Imperial College London

Department of Physics

Photonics Group

Vortex Laser Development Employing an Interferometric Output Coupler

---

Jan Willem Taubin Geberbauer

Thesis submitted in partial fulfilment of the requirements for the degree of
Doctor of Philosophy of Imperial College London

May 2022

Abstract

This thesis focuses on the design and implementation of new laser cavity designs for vortex mode generation. The vortex generation method is integrated into both solid-state laser cavities and systems using doped fibre gain mediums.

Optical vortex laser beams have attracted a lot of attention due to their proposed applications in a wide range of industries from communication to particle manipulation to microscopy to material processing. More recently, vortex generation directly from the laser has attracted research due to the potential for higher purity, higher power and a compact system. In this work a modified Sagnac interferometer, dubbed the vortex output coupler (VOC), is integrated as the output coupler of a laser cavity and used to convert the fundamental Gaussian intracavity mode into a first order Laguerre Gaussian output.

The VOC was first implemented into various solid-state cavities, with a Vanadate gain medium operating at $1064\,\text{nm}$, where vortex generation was successfully demonstrated. A record, from-the-source generated, vortex power of $31.3\,\text{W}$ was achieved, with a laser slope efficiency of 62.5%. The mode purity was 95.2% and the $\text{M}^2 = 2.25$. The handedness of the generated vortex was pure and switchable during operation. First order Hermite Gaussian modes with the same power were also demonstrated. The VOC was also shown to function in a pulsed cavity without any detrimental effects. It was found that the VOC has mode filtering properties, which helped maintain the a fundamental Gaussian in the cavity, despite mode mismatch between the pump beam and the fundamental Gaussian mode in the cavity.

Fibre laser systems have the advantage of being compact, alignment insensitive and maintaining a close resemblance to the fundamental Gaussian mode through the use of a single mode fibre. To demonstrate the implementation versatility of the VOC and capitalise on its power scaling potential, the VOC was integrated into a non-polarisation maintaining fibre laser system as a bulk output coupler. An Ytterbium-doped gain fibre was used, operating at $1064\,\text{nm}$, which allowed for the same optics as in previous work to be used for the VOC. $5.08\,\text{W}$ of vortex output power was achieved from the fibre laser system, with a mode purity and quality of 96.1% and $\text{M}^2_{X/Y} = 2.03/2.22$, respectively. This system was also used as a first order vortex source for higher order vortex generation, using a spiral phase plate. Vortices with orbital angular momentum values of $l = +2$ and $+3$ were generated from the first order vortex ($l = +1$) input using spiral phase plates, which imparted $+1$ and $+2$ orbital angular momentum (helical phase ramps of 2π and 4π respectively).

The VOC is made up of a beamsplitter and three turning mirrors, which are all high power damage threshold components. By choosing appropriate optical coatings for these components, considering wavelength and polarisation, the VOC can be implemented across the output spectrum making it incredibly versatile. The VOC is shown to function in a pulsed laser system, with a vortex pulse with duration 20 ns and energy 303 µJ shown in this work. The output mode can be switched between left and right vortex handedness and also between the first order Hermite Gaussian modes, all during operation. This pulsed operation and output mode versatility make it very interesting for material surface processing, particle levitation and manipulation, free-space communication and broadband, or ultrashort pulse, vortex generation. A VOC enhanced vortex laser can also be used as a high power and purity first order Hermite-Gaussian or Laguerre-Gaussain source for further conversion to higher order modes using other methods.

Acknowledgements

I seem to have somewhat stumbled into a Physics PhD, having started on the other end of the South Kensington campus in the Mechanical Engineering department. At the end of my undergraduate I received an email advertising the Quantum Systems Engineering programme, which wanted practically minded students to bring Quantum Mechanics into the real world.

I must first give thanks to my supervisor, Prof. Michael J. Damzen, for taking the leap of faith with a Mechanical Engineer, who decided that fiddling with mirrors made far more sense than Quantum Mechanics. His guiding hand and swift kicks up the backside have pushed me to achieve all that I have in this project.

I must also single out Dr. William R. Kerridge-Johns for special thanks, as he was the poor soul who dragged me kicking and screaming through the day-to-day. He was forever patient with all of my silly questions and was always on hand to talk through an issue with me.

I am very lucky to have worked with so many amazing colleagues in my research group. Those who came before me readily shared words of wisdom and encouragement: Dr Alex Coney, Dr Goronwy Tawy, Dr Ara Minassian, Dr Xin Sheng. Hopefully I was able to do the same for Meizhen Liang, Abdul-Haseeb Munj and Huaifeng Xiao, or at least demonstrate that they would have nothing to worry about.

I have to express my appreciation to Dr Anita "Megatron" Chandran for always being a shoulder to lean on and share in dark, sanity saving humour. She was also the first to start helping me figure out the feasibility of the fibre vortex laser and helped to show me the ways of fiddling with fibre systems. Dr Robbie Murray let himself be convinced of the merits of the fibre vortex collaboration and Dr Timothy Runcorn very kindly built the high power fibre gain system, which served as the basis for the fibre vortex laser. Thank you also to Paul Brown for the constant words of encouragement and positive vibes. Thank you to Martin Kehoe and Simon Johnson for their help with component manufacture and good energy.

Finally, I have to thank Immy for being a constant source of positivity. when I really didn't want to carry on or felt discouraged. Of course, thank you to my parents for supporting me through my academic journey and hiding their worries about my lack of future plans.

Statement of Originality

I confirm that all work in this thesis is my own. Any information used or derived from the work of others has been cited at each instance with references provided at the end of the thesis.

Copywrite declaration

Publications

Papers

J. W. T. Geberbauer, W. R. Kerridge-Johns, and M. J. Damzen, ">30 W vortex LG_{01} or HG_{10} laser using a mode transforming output coupler," *Opt. Express* 29, 29082-29094 (2021)

J. W. T. Geberbauer, W. R. Kerridge-Johns, and M. J. Damzen, "Q-switched laser with self-mode-filtering interferometric vortex output coupler," *OSA Continuum* 3, 204-213 (2020)

M. J. Damzen, W. R. Kerridge-Johns, **J. W. T. Geberbauer**, "Vortex mode transformation interferometry," *Journal of Optics*, vol. 22, pp. 1-9 (2019)

W. R. Kerridge-Johns, **J. W. T. Geberbauer**, and M. J. Damzen, "Vortex laser by transforming Gaussian mode with an interferometric output coupler," *Opt. Express* 27, 11642-11650 (2019)

Conference proceedings

J. W. T. Geberbauer, W. R. Kerridge-Johns and M. J. Damzen, ">30 W Vortex Laser Using Vortex Output Coupler," 2021 Conference on Lasers and Electro-Optics Europe & European Quantum Electronics Conference (CLEO/Europe-EQEC), 2021, pp. 1-1, doi: 10.1109/CLEO/Europe-EQEC52157.2021.9542383.

J. W. T. Geberbauer, William R. Kerridge-Johns, Michael J. Damzen, "Q-switched vortex laser using a Sagnac interferometer as an output coupler," Proc. SPIE 11259, Solid State Lasers XXIX: Technology and Devices, 112590E (21 February 2020);

W. R. Kerridge-Johns, **J. W. T. Geberbauer**, A. Volpini, and M. J. Damzen, "Vortex Laser Output with a Fundamental Gaussian Internal Mode using a Sagnac Interferometer," in Laser Congress 2018 (ASSL), OSA Technical Digest (Optica Publishing Group, 2018), paper AW2A.2.

Contents

x

List of Tables

List of Figures

Chapter 1

Introduction and thesis structure

Ever since Allen et al demonstrated that light modes could carry orbital angular momentum (OAM) in 1992, there has been a flurry of interest in how these light beams could be generated and harnessed [1]. With applications and proposed applications ranging from communication to material processing to particle trapping to imaging, generating and providing so called "vortex" beams on demand is the name of the game.

For three decades vortex work has almost exclusively been confined to research labs, with an input Hermite Gaussian beam being converted into the desired vortex beam. This required specialist optics, such as: cylindrical lenses, spiral phase plates and spatial light modulators. These optics can be expensive or require sensitive alignment. However, as the technologies move out of the labs a need for compact, robust, turn-key vortex sources arises. This need has prompted the research presented in this thesis.

Chapter 2 presents the optical vortex, how it can be diagnosed experimentally and a literature overview on generation techniques. Chapter 3 then introduces the Sagnac interferometer, which is the vortex generation technique that is the focus of this thesis. The Sagnac interferometer is tested experimentally and the conversion results are presented, as well as the required operating parameters.

Chapter 4 presents the results of introducing the Sagnac interferometer into a laser cavity as a vortex output coupler (VOC). An overview of vortex laser (vortex sources) literature and solid-state cavity design in given. Three vortex laser cavities are presented: the first success with continuous wave operation, slight power scaling with the introduction of pulsed operation

and a cavity lasing on an annular mode.

Chapter 5 presents a new vortex laser, designed to increase the achievable output power. The new cavity achieved a record 31.3 W vortex power directly from the laser, at the time of writing to the best of the authors knowledge. With a simple cavity adjustment, performed during lasing, first order Hermite Gaussian mode generation, with over 30 W, is also demonstrated.

Chapter 6 presents the results of integrating the VOC with a fibre based gain system, to create a fibre vortex laser. An overview of fibre vortex laser literature is presented, as well as the advantages gained by harnessing a fibre gain system. The systematic experimental approach of testing the VOC integration feasibility is then presented, culminating in a successfully lasing integrated fibre vortex system.

The aim of this work was to experimentally characterise the Sagnac interferometer, as a vortex conversion method, and demonstrate its ability to integrate into a cavity as a VOC. The project further aimed to highlight the versatility of the VOC in operation by presenting results from varying cavity configurations. The final aim of this project and thesis is to convince the reader of the further future potential the VOC holds for scientific interest and commercial use.

Chapter 2

Vortex mode generation

The aim of this chapter is to review what an optical vortex (OV) is and the literature on OV generation. First an OV is defined, with a focus on the Laguerre Gaussian modes. An overview of extracavity OV generation techniques is then presented, excluding fibre based techniques, which will be discussed in a later chapter. Finally, experimental modal analysis techniques are presented and discussed.

2.1   What is an optical vortex?

An optical vortex mode has an annular intensity profile, stemming from a helical phase structure, and have been shown to carry orbital angular momentum (OAM) [1]. The OAM stems from a helical phase in the electric field of the beam that can act either clockwise or anti-clockwise, defining the handedness of the vortex light. The annular intensity profile results from a zero-intensity phase singularity at the centre of the vortex mode. A rudimentary analogy to this may be to consider time zones around the North Pole, resulting in no official time or time-zone at the North Pole itself.

An example of stably propagating optical vortex modes are the Laguerre-Gaussian (LG_{pl}) modes when $l \neq 0$, these are shown in fig. 2.1. The Laguerre-Gaussian modes are solutions to the paraxial Helmholtz equation and form a complete basis set. They can be written in the

following form for a beam propagating along the z-axis:

$$E_{p,l}(r,\phi,z) = C_{pl}^{LG} \frac{w_0}{w(z)} \left(\frac{r\sqrt{2}}{w(z)} \right)^{|l|} L_p^{|l|} \left[\frac{2r^2}{w^2(z)} \right] exp\left(-\frac{r^2}{w^2(z)} \right) \times$$

$$exp\left(-ik\frac{r^2}{2R(z)} \right) exp(-il\phi) exp(i\psi(z)). \tag{2.1}$$

Where $C_{pl}^{LG} = \sqrt{(2p!)/(\pi(p+|l|)!)}$ is a mode dependent normalisation factor, $w(z) = w_0\sqrt{1+(z/z_R)^2}$ is the beam radius, $R(z) = z\left[1+(z_R/z)^2\right]$ is the radius of curvature of the beam, $\psi(z) = (N+1)arctan(z/z_R)$ is the Gouy phase, $r = \sqrt{x^2+y^2}$ is the radial distance from the centre axis of the beam, ϕ is the azimuthal angle around the central axis, $L_p^{|l|}$ is the Laguerre Gaussian polynomial of order p, which are the radial and azimuthal mode orders respectively. In the previous definitions w_0 is the minimum beam waist and $z_R = \pi w_0^2 n/\lambda$ is the Rayleigh length of the beam. In the definition of the Guoy phase $N = |l| + 2p$, due to the Guoy phase evolving differently for higher order modes. The term $exp(-il\phi)$ describes the helical phase profile, with an OAM value equal to l and the handedness represented by the sign.
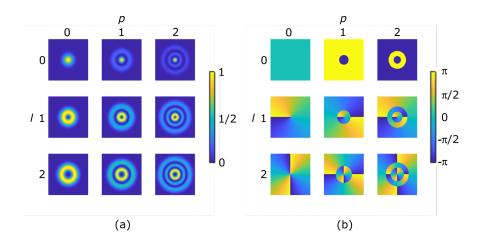
Figure 2.1: (a) Calculated spatial intensity profiles of the first nine Laguerre Gaussian modes. (b) Simulated phase profiles of the Laguerre Gaussian modes, corresponding to the modes shown in (a).

The Laguerre Gaussian modes represent a basis set in cylindrical coordinates. Solving the paraxial Helmholtz equation in Cartesian coordinates gives the complete basis set of Hermite-Gaussian (HG$_{nm}$) modes. These are also stably propagating modes and are shown in fig. 2.2.

They can be written in the following form:

$$E_{n,m}(x,y,z) = C_{nm}^{HG} \frac{w_0}{w(z)} H_n \left[\frac{\sqrt{2}x}{w(z)} \right] H_m \left[\frac{\sqrt{2}y}{w(z)} \right] exp \left(-\frac{x^2 + y^2}{w^2(z)} \right) \times$$

$$exp \left(-i\frac{k(x^2 + y^2)}{2R(z)} \right) exp(i\psi(z))exp(-ikz). \tag{2.2}$$

Where $k = 2\pi n/\lambda$ is the wavenumber, H_n and H_m are the Hermite polynomials of order n or m and $C_{nm}^{HG} = \sqrt{2/2^n 2^m n! m! \pi w_0^2}$. The definition of the Guoy phase remains the same, except for $N = n + m$. It is important to recognise that any mode of one set (LG or HG) can be created via the correct superposition of one or more modes of the other set.
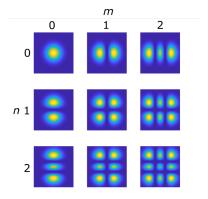
Figure 2.2: Calculated spatial intensity profiles of the first nine Hermite Gaussian modes.

2.2 Motivation

Vortex mode generation has become a rich vein of research due to the range of applications proposed. There are applications in material processing, where the complex light profile and OAM carried by the beam are used for surface texturing [2, 3, 4]. In particular, the creation of chiral nanoneedles has been much explored, whose chirality either depends on the OAM of the laser pulse or due to the spatial profile depending on the literature source.

The inherent, stable annular intensity profile of vortex beams lends itself to the trapping of micro and macroscopic particles. As opposed to particle trapping with a fundamental Gaussian beam, trapping with a vortex beam utilises photon pressure to trap the object, allowing the trapping of non-transmissive objects in the central intensity null. Further to simple trapping, the OAM of the vortex beam can spin the particle on its axis or make it orbit a central axis [5, 6, 7].

There is a plethora of research looking at using vortex, or LG, modes for high density information communication [8]. This is due to the orthogonality of all the higher order LG modes and importantly the ability to multiplex and demultiplex them. While, LG modes increase in transverse mode size with mode order, so called "perfect vortex" beams have been demonstrated, which have an unchanging spatial profile across different transverse modes [9, 10].

The stable annular intensity profile has also found a use in sub-diffraction limited imaging [11]. The vortex is used to deplete fluorescence, leaving the centre undepleted. A second beam can be used to analyse the undepleted centre spot. Crucially, this undepleted centre is smaller than the diffraction limited focused spot achievable.

2.3   Extracavity vortex mode generation

Spiral phase plates

A spiral phase plate (SPP) is perhaps the most intuitive method of generating a spiral phase front from a plane wave and was first demonstrated in 1994 [12]. It involves adding a transmissive optical element with a helical face (imagine a seashell) into the path of a plane beam. As a plane wave passes through the SPP the beam acquires a helical phase profile. This is well illustrated in fig. 2.3 [13], which shows the phase of a plane wave before and after passing through the SPP. The pitch of the SPP, h, is determined by the incident beam wavelength, λ,
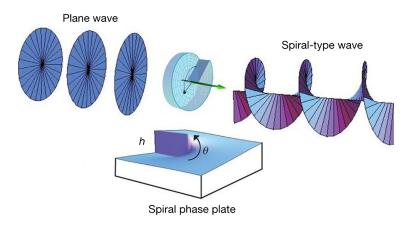
Figure 2.3:   Figure illustrating a plane phased wave passing through a spiral phase plate and becoming a helicaly phased wave [reproduced from Massari et al, 2015]. Inset bottom: side view of helical profile of spiral phase plate.

the refractive index of the SPP, n_{SPP} and the desired OAM, l, to be imprinted on the beam,

where

$$h = \frac{l\lambda}{n_{SPP} - 1}.$$

This condition ensures that the incident beam receives a $2\pi l$ phase change around its propagation axis, resulting in a true phase singularity.

SPPs are generally etched onto fused silica and therefore are capable of handling very high average and peak powers, making them ideal for material processing applications. However, the mode produced is impure due to the central power of the incident beam being diffracted out. The SPP is also wavelength dependent and has a fixed handedness.

Diffraction grating

An alternative to using a refractive element like the SPP, is to use a diffractive optical element. Using a photolithographic process to imprint an interference pattern on a substrate, an incident Gaussian beam can be converted into a structured beam with OAM [14, 15, 16]. The patterns used to create vortex beams can be spiral or forked interference patterns.

These patterns can also be generated using liquid crystal spatial light modulators (SLM). These can be readily designed to mimic any refractive index element, however only for a specific wavelength at a time. With the commercial availability of SLMs, which are essentially liquid crystal devices that can be programmed by a computer, this has become the most commonly used technique to generate vortex beams. These devices are often referred to as computer generated holograms, as they mimic an optical element. Some of these holograms are shown in fig. 2.4[17]. To convert a plane wave to a helical wave using an SLM either a forked diffraction grating [18, 19] is required or a spiral Fresnel lens [20]. Due to their ease of implementation and their flexibility in producing various or multiple modes, SLMs are the primary source of converted vortex beams. However, if a more complex beam is required then the implementation becomes more complicated. This is because it may be necessary to define the phase (l value) and also restrict the radial mode, p. SLMs are relatively expensive and do not have the power scaling capabilities of fused silica optics, but they are very flexible in their usage as they can be programmed.
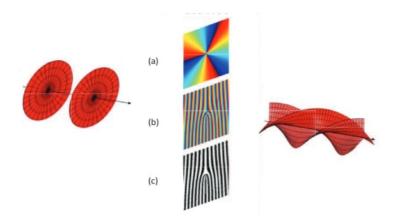
Figure 2.4:   a) Spiral phase hologram, b) forked phase hologram and c) binary forked phase hologram [reproduced from Rui et al, 2019].

Astigmatic mode converters

Both the Hermite-Gaussian (HG) and the Laguerre-Gaussian (LG) modes form complete basis sets. Therefore, given the correct combination of modes, one can use mode-superposition to generate any LG mode from HG modes and vice-versa. Mode conversion of a Hermite-Gaussian (HG) beam by passing it through a pair of cylindrical lenses was considered by Abramochkin and Volostnikov [21] and was employed by Tamm and Weiss [22], and was what Allen used [1, 23] for generating the LG modes. This conversion from HG to LG can also be achieved using astigmatic curved mirrors [24]. Fig. 2.5 shows an example of the mode superposition and phasing required for conversion into a 1st order LG mode. Practically, the example above may
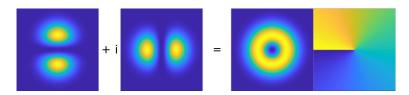
Figure 2.5:   Mode superposition of coherent HG_{01} and HG_{10} modes with a $\pi/2$ relative phase shift, resulting in an LG_{01} mode (intensity and phase shown).

be achieved by using a single HG_{01} beam at 45° and aligning the cylindrical lenses, or curved mirrors, such that a relative Gouy phase change occurs between the x-axis and y-axis. For the example shown above, a relative phase shift of $\pi/2$ needs to be introduced between the two orthogonal HG_{01} modes to generate an LG_{01}. Using this method can produce very high purity LG modes and have a high conversion efficiency, however it requires high precision construction

and subsequent alignment. This method is also wavelength sensitive.

Q-plate

The q-plate is a thin layer of liquid crystal sandwiched between two glass sheets. Changes in the local molecular alignment of the liquid crystal determine how it interacts with incident light of various polarisation states. The q-plate allows the user to transform circularly polarised light, with OAM = 0, into light carrying OAM by converting the spin angular momentum of the light into OAM [25, 26]. As it functions in transmission it is free of many alignments problems, as well as not introducing any astigmatism. The q-plate can also be used with a wide range of frequencies and ultra-short pulses. Q-plates can generate high purity vortex modes with a high conversion efficiency. However, they require the correct input mode and do not have the power scaling capabilities of fused silica optics.

Metasurfaces

Optical metasurfaces are able to manipulate the amplitude, phase, polarisation and frequency of light at a subwavelength scale, through intricate subwavelength surface patterning. These patterns can be manufactured to achieve a wide array of pure and superposition modes, as well as deconstructing these superpositions. Achievable mode purities can be in excess of 95% [27], however conversion efficiencies can struggle due to reflection/transmission losses, which reduces the achievable conversion efficiency [28]. Diffraction efficiency, and conservation of angular momentum, also plays a role in the conversion efficiency into the desired mode, however this can be largely overcome with the use of blazed diffraction gratings [29]. There is very little information available regarding the power handling or scaling capabilities of metasurfaces.

2.4 Vortex mode measurement

Verification of the vortex mode is important to distinguish between an annular beam, a vector-vortex (polarisation vortex) and our desired OAM vortex mode. The unique property of the OAM vortex is the helical phase profile, therefore interferometry is the most common method to identify the phase profile. By interfering a plane wave with the vortex the phase singularity in the vortex can highlighted. By interfering them both with the same wavefront curvature and a small tilt, a fork interference pattern is revealed, as shown in Fig. 2.6. At the phase

singularity the π phase jump interrupts the linear fringes you would expect between two plane waves, resulting in a fork. As the OAM content of the vortex increases, so does the number of forks in the interference pattern. When the vortex has wavefront curvature, the interference pattern becomes a spiral. As before, the number of spirals indicates the OAM content of the vortex beam.
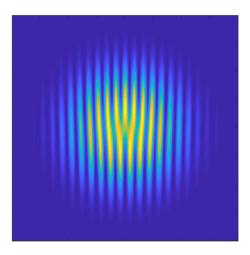
Figure 2.6:   Simulation of interference pattern achieved by interfering a vortex, with OAM content = 1, and a tilted Gaussian beam, with the same wavefront curvature. The fork in the centre represents the π phase jump at the centre of the beam.

2.4.1   Fork and spiral interference pattern

Experimentally, this can be implemented using a Mach-Zehnder interferometer (MZI). A MZI consists of two beamsplitters (BS) and two HR turning mirrors, where mirrors act to realign the two outputs of the first BS onto the second BS. The vortex mode to be measured is sampled by the first BS. One arm is allowed to diverge naturally, so that any small part of the larger beam can be assumed to be a quasi-plane wave. The other arm is re-imaged to a spatially smaller collimated beam, using two lenses in a telescope configuration. The interference of these two arms results in a fork interference pattern, when a small angular misalignment is introduced between them. By adding a third lens to the telescope arm the vortex can be made to be diverging at the camera, which introduces a wavefront curvature mismatch between the vortex and the quasi-plane wave and results in a spiral interference pattern. The MZIs used during this project were built from scratch on the lab bench for each project. During the construction, it was important to keep both arms of the MZI the same length to maintain the coherence of

both arms.

In later results, the MZI used for OAM verification is altered slightly. The beam is gently focused into the MZI, with the reimaging plane at the camera after the MZI. This foregoes the need to demagnify the beam using a telescope. To achieve a quasi-plane wave the reference arm is sampled using a pinhole, which is then followed by a lens for collimation [30]. This method introduces less optics into the beam path and therefore reducing the risk of distorting the beam.

The interferometric method can also be used to diagnose a super continuum vortex. While the pitch of the helical phase at each wavelength will be different, each wavelength will still have the phase singularity at the centre. Fig. 2.7 shows the fork pattern generated when interfering a super continuum vortex with an super continuum plane wave, with a range of 400-2000 nm and equal power in every wavelength. The result is one super fork in the middle, with washed out linear fringes, owing to the different wavelengths reducing the fringe contrast.
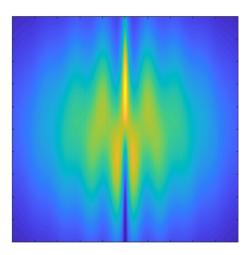
Figure 2.7: Simulation of interference pattern achieved by interfering a supercontinuum vortex (400-2000 nm) with a supercontinuum tilted Gaussian, both at their focus. This assumes that all wavelengths remain in phase to ensure all the forks overlap.

2.4.2 M^2 measurement

The fundamental mode of a Gaussian beam much sought after because it is diffraction-limited, which means when focusing the beam the achieved beam waist is the smallest possible for that specific wavelength. Therefore, the highest light intensity is achieved, for a given power, by a fundamental Gaussian mode. However, experimentally there are many factors which can

contribute to your laser mode being non-ideal, making it useful to understand how close your laser mode is to an ideal Gaussian. This is where the M^2 measurement becomes useful.

The M^2 measurement is a dimensionless value, which expresses how the measured beam propagates compared with a fundamental Gaussian as a ratio. A fundamental Gaussian therefore has a M$^2 = 1$. With the M^2 value of your laser mode, the minimum achievable waist size and its divergence when focused can be calculated. The M^2 of a laser beam is defined as

$$M^2 = \pi\theta_0 w_0/\lambda,$$

where w_0 is the beam width at focus and θ_0 is the half angle divergence of the beam. In practice, determining the exact position of the beam waist to measure the radius and knowing whether you have taken a read far enough away from the waist to get a precise measure of the divergence is difficult.

The ISO (International Organization for Standardization) set forward a method for measuring the M^2:

1. Collimate your laser beam.

2. Focus it with an aberration-free lens.

3. Measure the beam width at multiple points through the focus of the beam, also noting the position $(w(z))$.

4. Fit the measured points to

$$w^2(z) = w_0^2 + \left(M^2\right)^2 \left(\frac{\lambda}{\pi w_0}\right)^2 (z - z_R)^2.$$

The fit yields M^2, the beam waist position z_0 and the minimum beam width w_0. The beam width must be measured using the D4σ, or 2nd moments, definition of the beam width and at least 10 data points must be taken, approximately half within the one Rayleigh length from the focal point and the other half beyond two Rayleigh lengths from the focal point.

Experimentally, the M^2 was taken using a known lens, a camera on a translation stage and RayCi Pro software. The lens was chosen such that the beam was focused along the line of the translation stage, without resulting in a minimum beam width that was too small for the

camera to resolve. The wavelength was given to the RayCi software before a series of snapshots were taken on the camera, while translating it through the beam waist and inputting the camera position into the software each time. A minimum of 5 beam snapshots were taken on either side of the beam waist, two Rayleigh lengths away, and a further 5 snapshots were taken within one Rayleigh length of the beam waist. All of the M^2s presented in this thesis were taken in conform to the ISO standards and the error on the analysis was given as less than 1% (± 0.02).

2.4.3 Modal decomposition

The verification of the phase singularity is enough to demonstrate that the beam is carrying OAM. This interferometric analysis, coupled with the correct M^2, has been commonly used to confirm the generation of Laguerre Gaussian, or other, modes. However, as previously discussed, it is possible to achieve a helical phase, which does not have a uniform azimuthal profile. This beam would still produce a forked interference pattern and may propagate with close to the desired M^2, however it would not be a pure mode.

To provide more analysis of the vortex mode, various methods have been proposed and implemented. There have been attempts made to teach a neural network to analyse a spiral interference pattern and determine the purity of the incident vortex beam [31, 32]. Another method employed is to decompose the incident vortex beam using an SLM [33]. Later in this work, we use a phase retrieval algorithm developed by Dr William Kerridge-Johns based on that of Takeda et al. [34]. This algorithm performs a decomposition from the phase and intensity profiles of the vortex and plane wave used in the interference. The incident vortex beam is then reconstructed, from the calculated constituent modes' weights and phases, and compared with the incident mode for verification.

In this thesis, the M^2 value combined with a fork or spiral interference pattern is used consistently to diagnose the vortex result. In the earlier work, the intensity profile is also analysed for its uniformity and is matched to the ideal profile of an $LG_{0\pm 1}$ mode. However, in the later work modal decomposition is preferred because of its quantitative analysis on the purity of the mode. This decision was also made due to push back by reviewers in earlier papers, regarding our vortex analysis, and a general trend in the vortex community to present modal decompositions.

Chapter 3

Vortex generation using a Sagnac interferometer

This following chapter introduces interferometric vortex generation using a Sagnac interferometer, which is the technique used to achieve the results presented in the rest of the thesis, and experimental work conducted to investigate it. The theory and experimental set-up are presented, with reasoning for the pursuit of this method. Experimental results are presented of the extracavity conversion of a fundamental Gaussian input mode into a first order vortex, using the Sagnac interferometer. Different parameters affecting the quality of the conversion are investigated, such as the waist position and size. The use of the Sagnac interferometer for the conversion of vortex modes to higher order vortex modes is also briefly explored and preliminary results are presented. These results acted as precursors to results presented in a published work [35].

3.1   Motivation

Interferometry, as mentioned with the cylindrical lenses in the previous chapter, can theoretically be used to generate pure vortex modes with zero conversion loss. The optics employed can have very high damage thresholds, as no energy is deposited in them. However, they require higher order mode input and are alignment sensitive.

3.2 Interferometric vortex generation using fundamental Gaussian beams

As seen in the previous chapter, an HG_{01} and HG_{10} can be superimposed with a $\pi/2$ phase difference to create an $LG_{0\pm1}$. Two fundamental Gaussian beams can also be superimposed to create an $LG_{0\pm1}$[36]. This latter method can be advantageous as generating a high purity fundamental Gaussian with scalable power is easier than generating a similar higher order HG_{10} or HG_{10} mode.

Given the correct combination of angular misalignment in one axis and spatial misalignment in the orthogonal axis (see fig. 3.1) with a π phase shift between them, two otherwise co-propagating, coherent Gaussian beams will interfere to generate a first order Laguerre Gaussian mode carrying ±1 unit of orbital angular momentum (OAM). In this work the angular misalignment of each beam from the central propagating axis will be denoted by θ and the spatial misalignment from the central axis will be denoted with d. Further, the angular misalignment will always be applied in the x-axis, while the spatial displacement will be applied in the y-axis (where the z-axis denotes the propagation axis). This convention is applied for practical reasons demonstrated in the next section, however in theory this is arbitrary, so long as the two misalignments are orthogonal. Let us consider two fundamental Gaussian beams,
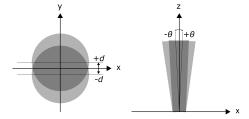
Figure 3.1: Figure showing spatial and angular misalignments, d and θ, where x and y are the horizontal and vertical planes, respectively, and z is the plane of propagation.

E_1 and E_2, and apply equal and opposite misalignments, at the minimum waist size of both beams:

$$E_1(x, y, z = 0) = C_{00} e^{-\frac{\left(x^2 + (y-d)^2\right)}{w_0^2}} e^{(-ik\theta x)} \tag{3.1a}$$

$$E_2(x, y, z = 0) = C_{00} e^{-\frac{\left(x^2 + (y+d)^2\right)}{w_0^2}} e^{(+ik\theta x)}, \tag{3.1b}$$

where w_0 is the beam waist at focus and $k = 2\pi/\lambda$ is the wavenumber (for wavelength λ) and $C_{00} = \sqrt{2/(\pi w_0^2)}$ is the normalisation constant at $z = 0$. The small angle approximation $Sin(\theta) \approx \theta$ has already been implemented for the transverse component of the wavevector. Coherently combining these two beams using a 50% beamsplitter with a common phase results in two output beams: one a destructive combination of the two beams and the other a constructive combination. This is due to the π phase shift at the glass to air interface for one of the beams into the two output ports of the beamsplitter, but not the other, resulting in:

$$E_t(x, y) = E_1(x, y) - E_2(x, y) \tag{3.2a}$$

$$E_r(x, y) = E_1(x, y) + E_2(x, y), \tag{3.2b}$$

where $E_t(x, y)$ and $E_r(x, y)$ are the beams resulting from the destructive and constructive interference respectively. These two solutions correspond to the transmitted and reflected beams of the Sagnac interferometer, which will be introduced in the next section. The analysis in [35] shows that the transmitted field $E_t(x, y)$ and the reflected field $E_r(x, y)$ can be rewritten as follows:

$$E_t(x, y) = 2 \left[\left(\frac{d}{w_0} \right) \frac{y}{w_0} + i \left(\frac{\theta}{\theta_0} \right) \frac{x}{w_0} \right] HG_{00} = \varepsilon_y HG_{01} + i\varepsilon_x HG_{10} \tag{3.3a}$$

$$E_r(x, y) = \left[1 - \frac{1}{2}(\varepsilon_x^2 + \varepsilon_y^2) \right] HG_{00} + \frac{1}{2} \left[\varepsilon_x^2 HG_{20} - \sqrt{2}i\varepsilon_x\varepsilon_y HG_{11} - \varepsilon_y^2 HG_{02} \right], \tag{3.3b}$$

where $\theta_0 = \lambda/\pi w_0$ is the far-field half-angle divergence of the Gaussian beam, $\varepsilon_y = d/w_0$ is the normalised spacial displacement, $\varepsilon_x = \theta/\theta_0$ is the normalised angular displacement, HG_{nm} are the normalised Hermite Gaussian modes and it is assumed $\varepsilon_x, \varepsilon_y \ll 1$.

Eq. 3.3a shows that the transmitted beam $E_t(x, y)$ can be rewritten as a superposition of HG_{01} and HG_{10}, with a $\pi/2$ phase difference, which interfere coherently to produce a LG_{01}. This is the case when the normalised misalignment parameters are equal, $\varepsilon = \varepsilon_x = \varepsilon_y$, which we call the canonical case. Here, we can also see that if only one misalignment is applied we end up with either a HG_{01} or HG_{10}. However, if the canonical condition is met, then eq. 3.3a can be written as

$$E_t(x, y) = i(\sqrt{2}\varepsilon)LG_{01}, \tag{3.4}$$

where the input fundamental Gaussian is transformed into a first order Laguerre-Gaussian

vortex. The scaling factor for the amplitude and intensity is dependent on the magnitude of the misalignments applied.

The reflected beam, $E_r(x, y)$, assuming the canonical condition, can be rewritten as

$$E_r(x, y) = \left[1 - \varepsilon^2\right] HG_{00} + \sqrt{2}\varepsilon^2 LG_{02}, \tag{3.5}$$

where $HG_{00} = LG_{00}$ is the fundamental Gaussian mode. The HG_{00} component in the reflected beam has an amplitude $(1 - \varepsilon^2)$ and intensity $(1 - 2\varepsilon^2)$ (to second order in parameter ε). There is an additional reflected weak LG_{02} signal with intensity reflectance $2\varepsilon^4$ (to fourth order in parameter ε). This term may be the from the small misalignment between the two constructively interfering beams, leading to a slightly elliptical mode. Experimentally, this may present itself as a slightly elliptical Gaussian mode when the misalignment's between two beams are increased.

The conversion efficiency, described as the desired LG_{01} or HG mode power relative to the input Gaussian power, which becomes the intensity transmission once the system is implemented into a laser cavity, can be calculated [37] as

$$T = \frac{1}{2} \left[1 - exp\left(-2(\varepsilon_x^2 + \varepsilon_y^2)\right)\right]. \tag{3.6}$$

The conversion efficiency relies on the magnitude of the misalignments. This becomes an important factor when implementing the system in a laser cavity and the output transmission can be used to optimise the laser output power.

Eq. 3.6 is general for all values of ε_x and ε_y, while the conversion theory presented assumes that the misalignments are small, $\varepsilon_x, \varepsilon_y \ll 1$. Fig. 3.2 shows the normalised spatial displacement against the theoretical transmission given by eq. 3.6, assuming that the canonical condition is met. Inset at the top are are the calculated transmitted intensity profiles at various transmission values. These show that the beam starts to "pull apart" as the transmission is increased, which makes sense intuitively as increasing the misalignments is physically separating the beams further. The helical phase profile is inherent to the conversion method, so the beam maintains its phase singularity, however, the azimuthal phase variation becomes less and less linear and tends towards that of a HG_{01} or HG_{10} mode.

The transmitted mode is exactly equal to the LG_{01} mode for $(d/w_0) \rightarrow 0$; however, the
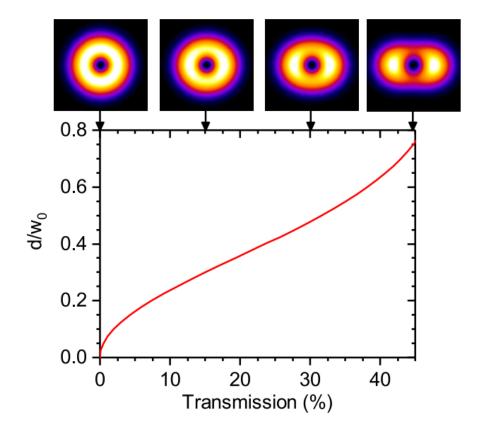
Figure 3.2: The VOC's theoretical transmission versus normalised displacement (d/w_0) assuming canonical condition operation, with calculated transmitted intensity profiles in the far field inset above.

vortex output maintains a close similarity to the ideal LG_{01} mode up to approximately T = 30%, as can be seen by the inset profiles in fig. 3.2, which is suitable as an output coupler for most solid-state laser systems.

3.3   Vortex generation using a Sagnac interferometer

There are a few options to achieve the theoretical Gaussian to vortex transformation, described in the section above, experimentally, such as: Sagnac interferometer [38], Mach-Zehnder interferometer (MZI) [36] and, with a slight twist, wedge plate [39]. In this work the former is used.

The Sagnac interferometer used in this work, as shown in fig. 3.3, consists of a 50:50 beamsplitter and three turning mirrors, forming a ring. An input beam enters the ring via one of the beamsplitter faces, gets split into two arms which counter propagate around the ring, before either constructively or destructively interfering at the beamsplitter, shown in fig. 3.3.

The destructive interference occurs on the transmission arm of the Sagnac interferometer due to one path being transmitted twice through the beamsplitter, while the other one takes two reflections, thus introducing a π phase shift between the two arms on transmission, achieving the first requirement necessitated by the theory.
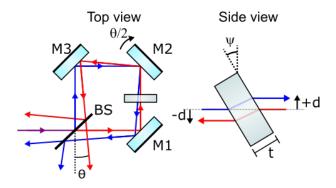
Figure 3.3: Top view: Input beam (purple) shown propagating around a Sagnac interferometer, before interfering at the beamsplitter. The two counter-propagating beams are shown in red and blue. The Sagnac interferometer consists of a beamsplitter (BS), an AR coated plane-plane plate (tilt-plate) and three turning mirrors (M1, M2, M3). Side view: Two arms of Sagnac interferometer passing through tilt-plate.

To achieve vortex generation the addition of angular misalignment and spatial displacement are required. The angular misalignment is imparted through a rotation of mirror M2. A $\theta/2$ rads rotation of M2 introduces the angular misalignment θ rads away from the propagating axis, in the x-plane. The spatial misalignment can be imparted in two ways: mirrors M1 and M3 can be tilted in an equal and opposite manner to walk the two counter propagating beams away from the propagating axis vertically or by using a tilted plate in the ring, as shown in fig. 3.3. When the plate is tilted by a small angle ψ, the spatial displacement is given by $d = t\psi(1 - 1/n)$, where t is the thickness of the plate and n is the refractive index of the material (N-BK7 glass, $n = 1.517$). The Sagnac interferometer set up shown has been dubbed the vortex output coupler (VOC) and will be referred to as such throughout the rest of this thesis.

Implementing the superposition of two Gaussian beams has many advantages. Firstly, a very high purity vortex mode can be achieved. Secondly, the necessary experimental equipment is standard, off-the-shelf equipment, found in laser labs and can be selected to have very high

damage thresholds. The coatings of the equipment can also be selected to be broadband for ultrashort pulses [38] or perhaps for tunable source vortex generation.

As mentioned, when the two counter-propagating arms of the Sagnac interferometer recombine at the beamsplitter there is both destructive and constructive interference, which are described by eq. 3.4 and eq. 3.5. Some of the input Gaussian is transformed into a LG_{01} when the canonical condition is met and the reflected beam is an almost unchanged Gaussian beam. Interestingly, when the misalignments are set to zero, there is no transmission and the reflected beam is the same as the input beam. When perfectly aligned for zero transmission, the Sagnac interferometer acts as a retro-reflector, and when it is aligned to transmit a vortex it acts as a quasi partially reflective mirror at 0°. This feature makes it suitable to be implemented as the output coupler of a laser, as a tunable part of the input power is reflected to maintain the intracavity mode of the laser.

3.4   Experimental implementation of the Sagnac interferometer

To explore the theory laid out in the previous section the Sagnac interferometer was mounted on a translation stage with an AR coated plane-plane window on a rotation mount and a piezo actuator controlling the x-tilt of M2, as shown in Fig. 3.4. A fundamental Gaussian beam was focused into the Sagnac interferometer and the translation stage was aligned such that mirror M2 of the Saganc interferometer could be translated through the focus of the incident beam. The transmitted vortex beam was focused (lens not shown) onto a camera on a translation stage, to allow an M^2 measurement to be taken. A portable power meter was also used to record the input and output powers. This allowed for the investigation of the Sagnac interferometer.

The input beam parameters are laid out in Table. 3.1. The 1064 nm HG_{00} input was focused to a minimum waist radial size $w_0 = 130\,\mu m$, which gave a Rayleigh range and half-angle divergence of 50 mm and 2.6 mrad, respectively. This was chosen to allow for multiple points to be investigated within the Rayleigh range.
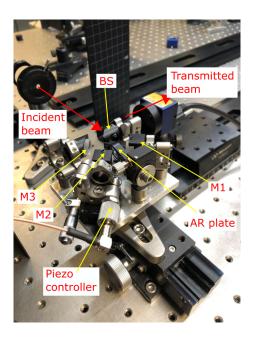
Figure 3.4: Image of optical bench showing experimental setup. Front centre: Sagnac interferometer mounted on an aluminium plate consisting of a beamsplitter (BS), three turning mirrors (M1, M2, M3) and an AR coated window held in a rotation mount. Bottom centre: The Sagnac interferometer and it's aluminium mounting plate were clamped onto a translation stage. Top left: Input focusing lens and aperture. Top right: Camera imaging the output of the VOC, mounted on a translation stage.

Input Beam		
Beam parameter	X	Y
M^2	1	1
w_0	$132\,\mu m$	$126\,\mu m$
z_R	$52\,mm$	$47\,mm$
θ_0	$2.55\,mrad$	$2.7\,mrad$

Table 3.1: This table shows the input mode parameters in the x- and y- axis for the $1064\,nm$ source used to test the Sagnac Interferometer.

3.4.1 At zero transmission

When initially building the Sagnac interferometer, the beamsplitter is first aligned to the incident beam for 50:50 power splitting. The three turning mirrors are then added, ensuring that the beam height is maintained. To check that the mirror angles are correct, and double check the vertical axis, the output of the Sagnac interferometer is monitored on a camera. When the two counterpropagting arms of the Sagnac interferometer are perfectly realigned at the beamsplitter, perfect destructive interference should occur at the output. An example of the output when the Sagnac interferometer is perfectly aligned for zero transmission is shown in

fig. 3.5. The central region of the intensity snapshot is very well zeroed, and only very faint interference fringes can be perceived. The two Gaussian intensity spots either side are the result of the two arms each taking a reflection off of the AR coated face of the beamsplitter. The relative intensity of the AR reflections to the transmitted mode in the centre shows the excellent zeroing that can be achieved. Once the Sagnac is zeroed, the reflected beam can be
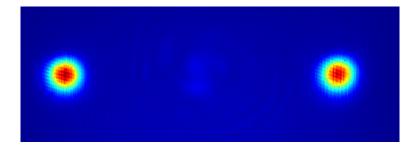
Figure 3.5: Snapshot showing the intensity profile of the output of the Sagnac interferometer when misalignments are zero ($d=\theta=0$) and the Sagnac interferometer is behaving like a retrore-flector. The two Gaussian intensity spots are due to the reflections off the AR coating of the beamsplitter.

steered to be completely aligned with the incident beam. The Sagnac interferometer functions like a retro-reflector, so the vertical angle and horizontal displacement of the reflected beam would need to be optimised to achieve alignment with the incident beam. This can be achieved by optimising the vertical angle of mirror M2 and the z-position of mirror M2, which can be done using a translation stage as can be seen in fig. 3.4.

After optimisations of the Sagnac ring have taken place, the AR coated plane-plane window can then be added and optimised to get back to the zero transmission again.

3.4.2   Effect of input beam waist position on the vortex generation

The theory requires that the angular misalignment between the two beams is applied at a common waist position. When the angle is applied away from the common waist then a spatial misalignment in the x-axis is simultaneously introduced. It is therefore required that the input beam waist is positioned on the mirror M2. To investigate the sensitivity to waist position the VOC was systematically translated through the input beam's focus. The misalignments in the VOC were applied to satisfy the canonical condition for the beam size at each point. A snapshot at each position was taken and is shown in Fig. 3.6. The distance measurements have

an arbitrary start on one side of the input beam focus and show the translation through the waist in 5 mm steps.
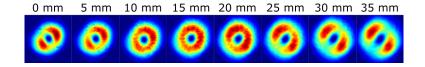
Figure 3.6: Snapshots of the vortex output as the VOC is moved along the axis of the input beam propagation. Distances (above) show progression of VOC, starting before the input beam comes to a focus and ending after the focus.

The snapshots show that the waist position of the input beam is around the translation point at 15 mm, as the most symmetric intensity profile was found at this point. At both points "10 mm" and "20 mm" the beam profiles are asymmetric, indicating that beam waist is not on the mirror M2 and the effect of the introduced translation in the x-axis between the two counter-propagating beams can be seen. No matter the combination of the misalignments, d and θ, the two lobes that are visible remain prominent. The spatial x misalignment, Δx, quickly increases with either waist distance from M2, δ, or angle θ as $\Delta x = \delta Tan(\theta)$. This is reflected in the increasing separation of the two lobes with distance from the optimal position. It is also interesting to note that the direction of separation changes as the Sagnac interferometer is moved through the focus due to the sign change in Δx, which is similar to inverting either d or θ to effect a sign change in the vortex output.

While for many applications the beam size can be assumed to be constant within the Rayleigh range, it is obvious that for vortex conversion using the Sagnac interferometer it can make a significant difference. Furthermore, a change of $\sqrt{2}$ in the beam size would change the canonical condition by 40%. The problem of position the waist correctly becomes arbitrary once the Sagnac interferometer is positioned within a cavity as M2 becomes en effective end-mirror and therefore a stable cavity configuration requires a waist to be positioned there.

3.4.3 Variable vortex transmission

For the Sagnac Interferometer to convert an incident Gaussian beam into a vortex, the misalignments applied must satisfy the canonical condition. However, the absolute value of the misalignments can be varied. By increasing the misalignments, while maintaining the canonical

condition, the amount of power transmitted in a vortex mode can be increased.

The displacement and the angular misalignment were quantifiable in this system. Therefore the theory of the Sagnac interferometer and the applicability of optimising the misalignments for a intensity output vortex verified. With this purpose the transmission of the Sagnac interferometer was systematically increased. At each point the M^2 was then taken, the misalignments were recorded and the power of the input beam and the transmitted beam was recorded. From this the parameters θ/θ_0, d/w_0 and the canonical ratio were calculated. The transmission of the Sagnac interferometer, T_{power}, was simply calculated by taking the ratio of the output power against the input power. Additionally, to test the theory laid out previously, the misalignments were substituted into eq. 3.6. Firstly, the vortex was assumed to be canonical and only the θ misalignment was used ($\varepsilon_x = \varepsilon_y = \varepsilon$) to predict the transmission, $T_{canonical}$. Secondly, both recorded misalignments were substituted into eq. 3.6 to give $T_{non-canonical}$. The data taken and calculated are summarised in table. 3.2. The snapshots shown in fig. 3.7 correspond to each point recorded.

M^2 (X/Y)	θ (μrad)	d (μm)	θ/θ_0	d/w_0	$\frac{(\theta/\theta_0)}{(d/w_0)}$	T power (%)	T canonical (%)	T non-canonical (%)
2.17/2.22	305.0	11.9	0.116	0.092	0.794	3.2	2.6	2.1
2.14/2.10	576.3	32.7	0.220	0.254	1.155	9.5	8.8	10.0
2.14/2.04	732.1	35.7	0.279	0.277	0.992	13.7	13.4	13.3
2.00/2.16	811.2	47.6	0.309	0.369	1.194	17.9	15.9	18.4
2.08/2.06	898.0	47.6	0.342	0.369	1.078	19.7	18.7	19.8

Table 3.2: This table shows the data recorded while incrementally increasing the absolute misalignments in the Sagnac interferometer. At each point the M^2 was recorded. Then the misalignments, d and θ, were recorded and used to calculate θ/θ_0, d/w_0 and the canonical ratio. Finally, the transmission was calculated in three ways: using the transmitted power divided by the incident power, calculating the transmission assuming the canonical condition and using the theoretical transmission formula, and finally using the theoretical transmission formula but not assuming the canonical condition.

While each point was only optimised to achieve the best aesthetic vortex (most uniform intensity pattern), the M^2 values suggest that this is a good approximation. It is important to remember that a 2π azimuthal phase variation is inherent in this conversion method, therefore optimising for a uniform intensity pattern offers a good approximation of whether the canonical condition is being satisfied.
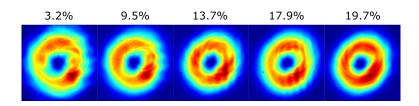
Figure 3.7: Snapshots of vortex at varying transmission.

By recording the applied misalignments, the practical implementation of the theory could be investigated. In an ideal experimental environment, the appropriate misalignments needed to satisfy the canonical condition for a given transmission could be calculated and applied precisely using appropriate rotation mounts. However, while translations on the scale of microns or micro-radian rotations are achievable, even by hand, precise and repeatable implementation using motion control is still difficult. Table. 3.2 shows the recorded M2 mirror tilt, θ, which is then used to calculate the canonical ratio. A canonical ratio equal to 1 tells us that the phase profile of the converted vortex should have a linear azimuthal phase ramp, akin to that of the LG_{01} mode. The calculated canonical ratios vary by $\pm 20\%$, even though the transmitted beams all have M^2s < 2.2. However, the beams with transmission values of 13.7% and 19.7%, which have the most uniform intensity profile also have a canonical ratio closest to 1.

3.4.4 Higher order mode generation

With a fundamental Gaussian input, and just d and θ misalignments, the output of the Sagnac interferometer is limited to a vortex (including the $LG_{0\pm1}$ modes) and the HG_{10}/HG_{01} modes. However, with an incident LG_{01} mode, higher order modes can be accessed. This is described in Damzen et al. [35] mathematically and can be simplified to say that the Sagnac interferometer can add or subtract one order of topological charge from the incident beam. If the Sagnac interferometer is misaligned in a complementary fashion to the incident LG_{01}, then the output will have a total of OAM of 2, and vice-versa.

In order to verify this theory, a second Sagnac interferometer was constructed and used the output of the first Sagnac interferometer as an LG_{01} input source. The incident mode was carefully focused onto the M2 mirror of the second Sagnac. The results of both the complementary and opposite misalignments are shown in Fig. 3.8. Fig. 3.8b shows the output

when the misalignments are opposite, it corresponds to the LG_{10} and has OAM $= 0$. Fig. 3.8a shows the output when the misalignments are complementary to the input OAM, the total OAM of the output is 2 however it is contained in two singularities with the same handedness. The two snapshots are taken at the beam focus, demonstrating stable propagation. The orientation of the vortex pair goes through a 90° rotation through the focus and is at $\pm 45°$ from the y axis in the farfield.

(a)   (b)
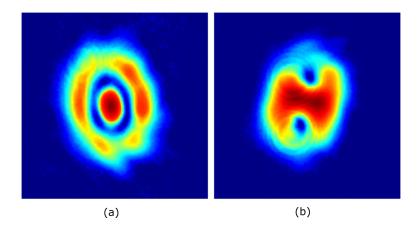
Figure 3.8:   Snapshots of the conversion an LG_{01}, using the VOC into (a) an LG_{10} and (b) a vortex pair formed by the superposition of an LG_{02} and a fundamental Gaussian. Both snapshots were taken at the respective beams' focus.

By varying the input mode, a range of different modes and superposition states can be accessed, which would otherwise require complex holographic phase maps or custom designed metasurfaces [35]. Accessing these higher order modes and superposition states has potential applications in high capacity data communication, matter manipulation and trapping, and material processing. Using the Sagnac to achieve these states significantly increases the limit on input power, imposed by a liquid crystal optic. By flipping or removing either of the misalignments, this technique allows rapid switching between different outputs. The conversion method is also polarisation independent, although higher losses may be incurred depending on the coating of the optics.

3.5   Chapter summary

In this chapter, the concept of an optical vortex was introduced along with an overview of the literature regarding vortex generation techniques. The Sagnac interferometer was presented as

a way to implement interferometric vortex generation, from the coherent superposition of two Gaussian beams. The theory of the interferometric vortex generation was also laid out.

The Sagnac interferometer was tested and successfully produced a vortex, from an input Gaussian beam. The effect of beam waist position within the Sagnac interferometer was investigated and it was found that the input beam waist had to sit on mirror M2, for ideal vortex conversion. The Sagnac interferometer allows for tunable transmission between 0-30% (how much of the input mode is converted into a vortex) and the experimental control over this was tested against theory. The predicted transmission, using the misalignments of the beam, matched the measured transmission with a correlation coefficient of >99.5%.

Finally, a LG_{01} vortex beam was used as the input for a second Sagnac ring. It was demonstrated that the ring could add or subtract a unit of OAM, generating different modal superpositions.

The major drawback of the vortex generation technique presented thus far is its relatively low conversion efficiency. Being effectively limited to small misalignments ($d/w_0 << 1$) to maintain high vortex mode purity, this limits the transmission of the VOC to $\approx$30% with the rest of the power reflected back. However, using off-the-shelf components, the Sagnac interferometer can operate up to the normal power limits of fused silica optics making it suitable for high power vortex generation. With standard fused silica broadband dieletric mirrors 100 W+ or milliJoule pulse energies could be supported using the Sagnac Interferometer. The specilist component coatings can also be selected to allow for even higher powers and pulse energies, broadband conversion or conversion of ultrashort pulses.

Chapter 4

Solid-state vortex laser development

This chapter builds on the previous chapter, by investigating the introduction of the Sagnac interferometer into a laser cavity as a vortex output coupler (VOC). An overview of the literature on integrated vortex lasers is presented, to provide context to the work. Solid-state cavity design is discussed, with particular interest on achieving and maintaining a fundamental Gaussian mode in the cavity. Three vortex laser cavities are presented with results and discussion on merits and limitations.

The experimental cavities investigated were end-pumped Neodymium doped Vanadate (Nd:YVO$_4$) cavities. The pumping came from a fibre delivered laser diode module with a nominal wavelength of 808 nm. The first cavity represents the first experimental integration of the VOC into a cavity and achieved a maximum vortex output power of 3.2 W. An efficiency comparison between a similar cavity with a fundamental Gaussian output and the vortex was made. The effect of VOC transmission on mode quality and power output was also investigated and the results are presented.

The second cavity provides some power improvement, with a maximum vortex output power of 5.1 W achieved. Additionally, an acoustooptic modulator was integrated into the cavity to achieve Q-switching and the successful pulsed vortex results are presented. The power scaling was limited by fractures in the crystal due to deposited pump power, which was verified with finite element analysis of the crystal. During operation, it was observed that the intracavity fundamental Gaussian mode maintained a better beam propagation factor in the vortex cavity than it did in a similar cavity without the VOC. This higher order mode suppression was

investigated, experimentally verifying that the VOC has a higher transmission (an effective loss term for the cavity) for higher order modes, thereby suppressing them in the cavity.

The third vortex cavity came about while building the second one. An output beam with a doughnut shaped profile was observed, from a plane-plane mirror cavity. The results taken from this cavity are presented and the disadvantages discussed.

Some of the results in this chapter have contributed to two published works [37, 40] and experimentally verified analysis in a third [35], demonstrating the potential of the VOC for high power vortex generation, both CW and pulsed, and its mode filtering properties.

4.1 Motivation

As mentioned in the previous chapter, the drawback of the vortex output coupler (VOC) for vortex generation is the poor conversion efficiency, being effectively limited to <30%. However, if the VOC were introduced as the output coupler of a laser cavity, with the reflected beam used to maintain the cavity mode, then the conversion efficiency would effectively increase to 100%.

Along with better efficiency, vortex lasers offer the possibility for turn-key vortex sources, which would provide the backbone for wider implementation in research and industry. This approach can also remove the need for precise alignment of conversion elements by exploiting the loss-avoiding nature of laser cavities and natural noise filtering [41]. Also, the ability to use the VOC as variable transmission output coupler is useful in cavity optimisation for power optimisation [42].

4.2 Vortex lasers

As with extra-cavity vortex conversion techniques discussed in the previous chapter, there have been a number of different techniques used to achieve a vortex laser source. A widely researched method is to force the preferred internal mode of the cavity away from the usually favoured fundamental Gaussian and onto the desired vortex mode. One of the most intuitive ways of achieving this is to create a spot defect on one of the end mirrors [43, 44, 45, 46, 47, 48]. A low reflectivity spot is created, either by hand or using laser ablation, and positioned in the centre of the beam path within the cavity making the fundamental Gaussian very lossy. The

spot defect has also been achieved using an SLM [49]. The aim is for the cavity to lase on an annular mode, which allows for an incoherent superposition of $LG_{0\pm1}$. A further optic is then usually required to increase losses for one handedness, so that the laser only lases on a single mode.

Similarly, instead of creating losses for the fundamental mode there has been work carried out into directly exciting the $LG_{0\pm1}$ through annular pumping [50, 51, 52, 53] and off-axis pumping [54, 55]. Here the pump spot is matched to the desired intracavity mode. As with the spot defect, a further intracavity optical element is usually required to isolate a pure handedness in the cavity. The off-axis pumping scheme has also been used for Hermite-Gaussian mode generation which was then converted into a Laguerre Gaussian mode extra-cavity using astigmatic mode converters [56, 57, 58, 59, 60].

Another gain shaping technique employed has been to implement a coupled cavity [61]. Here two cavities share a single gain medium; one lases on the fundamental Gaussian mode, depleting the central region of the gain medium and forcing the second cavity into a higher order Laguerre Gaussian. Pump induced spherical aberrations in the gain medium have also been shown to result in the cavity preferentially lasing on a Laguerre Gaussian mode [62, 63, 64]. However, like the other methods of gain shaping these usually require another optic to force the cavity into one handedness or the other.

Research has also been conducted into shaping the intracavity mode by inserting transforming elements into the cavity, which use polarisation and/or phase changes. Q-plates [65, 66], metasurfaces [67, 68] and SLMs [49, 69] have been implemented into cavities in efforts to create fully controllable structured light lasers.

Gain shaping techniques have been widely researched, probably due to the lack of specialist equipment required. However, they often struggle with efficiency issues, due to added losses in the cavity or poor matching between the desired mode and the pump mode. Using pump shaping can also lead to awkward thermal lensing effects, making power scaling difficult. Reliance on the thermal lens in the gain medium limits the exercisable control of the user and the power range over which successful vortex generation is achieved. All techniques without inherent handedness selection also require additional optics or misaligment to achieve this.

The introduction of phase or polarisation changing optics into the laser cavity has resulted in the direct generation of a wide array of modes and superpositions. However, the optics introduced tend to be very sensitive to power scaling.

4.3   Solid-state lasers

For the electric field of a laser beam to stably oscillate in a laser cavity, it must exactly reproduce itself every round trip. Both the transverse spatial intensity and phase profiles must be replicated, ensuring that the so-called laser mode is self-reproducing and sustainable.

Radiation emitted by most lasers contains several discrete optical frequencies, separated by a frequency difference dependent on the cavity optical path length. These various fields, operating at different optical frequencies, are referred to as longitudinal modes. Transverse modes refer to spatial modes that have a particular intensity distribution and a particular oscillation frequency.

It is useful to consider the transverse spatial intensity profile and the longitudinal phase reproduction separately as they are responsible for different aspects of the laser performance. The characteristic beam divergence, beam diameter and energy distribution are governed by the transverse mode. The characteristics line width and temporal coherence length are governed by the longitudinal modes.

Transverse Modes

The transverse modes of a resonator, introduced earlier, are propagation invariant, ensuring that they fulfil the self reproduction requirements. These transverse modes are solutions to the paraxial Helmholtz equation. Solutions in Cartesian coordinates give Hermite-Gaussian (HG) modes, whereas cylindrical coordinates gives Laguerre-Gaussian (LG) modes. Both form complete basis sets, from which all other modes (solutions) in other coordinate systems can be generated.

Longitudinal Modes

A longitudinal mode in the laser resonator is a standing wave, reinforced by constructive interference on every round-trip of the cavity. In essence this refers to an exact wavelength of light. Multiple longitudinal modes can form in a single cavity, with a frequency spacing determined

by the optical length of the cavity. If we examine the simplest resonator formed of two parallel plane mirrors, also referred to as a Fabry-Perot cavity, the permitted longitudinal modes satisfy the following condition:

$$L = b\frac{\lambda}{2} \tag{4.1}$$

where L is the mirror separation and b is an integer known as the mode order. These longitudinal modes, or acceptable resonator wavelengths, will have a frequency separation, $\Delta\nu$, of

$$\Delta\nu = \frac{c}{2nL} \tag{4.2}$$

where c is the speed of light and n is the refractive index of the cavity medium. In a laser resonator containing multiple optical elements, the frequency spacing of the longitudinal modes becomes:

$$\Delta\nu = \frac{c}{2\Sigma_i n_i L_i} \tag{4.3}$$

where n_i and L_i are the refractive index and length of the i-th element in the laser resonator.

In practice, the number of longitudinal modes able to oscillate in a laser resonator depends on more than just the resonator geometry. Importantly, each longitudinal mode must fall within the spectral width of the gain medium used. The number of longitudinal modes present in a cavity can be estimated using the spectral width of the gain and the frequency spacing of the modes. The number of longitudinal modes present in a laser resonator can be referred to as the spectral width or linewidth of the laser emission. This becomes a prominent feature of the laser design when either a very narrow laser linewidth (eg. for interferometry) or a broad linewidth (eg. for ultrashort pulses) is required.

4.3.1   Stability

As mentioned at the beginning of the chapter, when designing a cavity the electric field must be exactly reproduced after one round trip to ensure stable operation and lasing. This can be achieved by modelling the beam through one round trip of the cavity using ray propagation matrices. The effect of propagation through free space with length d, a lens with focal length

f and a curved mirror with curvature R can be expressed with the following three matrices:

$$\begin{pmatrix} 1 & d \\ 0 & 1 \end{pmatrix} \quad , \quad \begin{pmatrix} 1 & 0 \\ -1/f & 1 \end{pmatrix} \quad and \quad \begin{pmatrix} 1 & 0 \\ -2/R & 1 \end{pmatrix}.$$

These matrices can be used to calculate the effect optical elements, and therefore a laser cavity, on the parameters of a Gaussian beam. A convenient quantity for that purpose is the complex wave parameter q, defined as

$$\frac{1}{q} = -i\frac{\lambda}{\pi w^2} + \frac{1}{R}, \tag{4.4}$$

where w and R are the beam width and radius of curvature at a chosen point. The product of the ray propagation matrices is generally represented by $\begin{pmatrix} A & B \\ C & D \end{pmatrix}$ and modifies q in the following way:

$$q' = \frac{Aq + B}{Cq + D}, \tag{4.5}$$

where q' is the modified complex wave parameter.

In the case of a stable cavity, one round trip should result in $q = q'$. In the case of the simplest cavity configuration with cavity length L and two mirrors with radius of curvature R_1 and R_2 the stability criteria can be summarised by two parameters $g_1 = 1 - L/R_1$ and $g_2 = 1 - L/R_2$ in the following relationship:

$$0 < g_1 g_2 < 1. \tag{4.6}$$

4.3.2 Pump induced lensing effects

Optical pumping generates heat in the gain medium mainly due to the energy difference between the pump photon and the laser photon, dubbed the quantum defect. This heat deposition can lead to the gain medium developing a lens-like attribute, called thermal lensing, and can eventually lead to stress fracturing of the crystal. The thermal lens can change the stability criteria of the laser resonator, making stability of the cavity input power dependent. Stress fracturing of the crystal ultimately limits the average power obtainable from a particular laser material.

There are multiple ways in which heat deposition in the gain medium contributes to a

thermal lens. The heating leads to expansion in the gain material which can result in surface bulging, turning the pumped surface into a physical lens. These are the stresses that eventually result in stress fracturing. These stresses also change the local refractive index via the photo-elastic effect [70]. There is also a temperature dependent element to the local refractive index of the laser material. Both of these change the refractive index profile across the laser material, which has a further lens-like affect on the laser resonator mode. This combined lensing effect can change the cavity stability, as previously mentioned, but can also distort the beam if the thermal lens is not uniform.

The minimisation of heat generation in the laser material is therefore crucial in achieving high average output powers from the laser and limiting the pump dependent affect on the cavity stability and mode quality. This can be approached in a number of ways. The first is to match the pumping wavelength as closely as possible to the required emission wavelength to reduce the quantum defect, however this is limited by the absorption spectra of the laser material and available pump sources. The second, almost universally used, method is to apply a cooling jacket to the laser material, which helps remove heat from the sides. Another technique, to reduce surface bulging, is to have undoped endcaps on the laser material. This provides mechanical resistance to the stresses and also helps with heat dissipation.

4.3.3   Cavity specific stability

Most real cavities are more complicated than just two mirrors. Almost certainly the gain medium in the cavity will have a lens-like effect on the mode passing through it. This, however, is not accounted for is the basic stability equation. Magni et al. [71] expanded the basic equations for stability parameters g_1 and g_2 to include an intracavity lens.

Three new equations are presented for effective cavity length

$$L_e = L_1 + L_2 - \frac{L_1 L_2}{f},$$ (4.7)

and for the stability parameters,

$$g_1 = 1 - \frac{L_2}{f} - \frac{L_e}{R_1}$$ (4.8)

and

$$g_2 = 1 - \frac{L_1}{f} - \frac{L_e}{R_2}. \tag{4.9}$$

All the terms used in these equations, except L_e (L' in the Magni paper), refer to the labelled parameters in Fig 4.1.
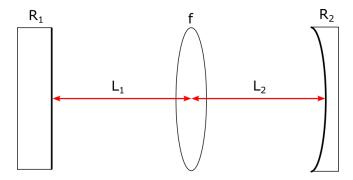
Figure 4.1: Cavity diagram with cavity parameters used in the Magni equations labelled. R_1 and R_2 are the radius of curvatures of the two end mirrors, L_1 and L_2 are the cavity length between the end mirrors and the lens, and f is the focal length of the central lens.

Fig 4.1 shows a typical cavity used during this PhD. The gain crystal was either placed in the centre of the cavity, and is represented by the lens, or it was placed next to one of the output couplers, which can be approximated by a curved mirror. A lens was always added either next to one of the output couplers or in the centre of the cavity, depending on where the crystal was, to provide further control over the cavity stability. This cavity can be approximated by the work in Magni et al. [71], therefore the equations are refined and analysed to give a better understanding of the cavity mode's responses to changes to cavity geometry. The output coupler is a plane mirror, therefore R_1 is infinite. Given this, we can simplify eq. 4.8 to

$$g_1 = 1 - \frac{L_2}{f}. \tag{4.10}$$

This leaves us with

$$L_e = L_1 + L_2 - \frac{L_1 L_2}{f}, \quad g_1 = 1 - \frac{L_2}{f} \quad and \quad g_2 = 1 - \frac{L_1}{f} - \frac{L_e}{R_2}.$$

The last useful term we need is the mode size at the crystal. In our Magni approximation this becomes the mode size at the back mirror. This is given by

$$w_2 = \left[\frac{\lambda |L_e|}{\pi} \left(\frac{g_1}{g_2(1 - g_1 g_2)} \right)^{0.5} \right]^{0.5}. \tag{4.11}$$

Changing the cavity and stability parameters

It is important to have a sense of how changing certain aspects of the cavity effect the stability
parameters. The following section will walk through different changes via the maths.

Changing L_1

Considering the impact of changing L_1, we see that g_1 stays unaffected. The change impacts
L_e as follows

$$L_e = (L_1 + \Delta L_1) + L_2 - \frac{(L_1 + \Delta L_1)L_2}{f}. \tag{4.12}$$

Therefore, if $\frac{L_2}{f} > 1$, then L_e will decrease with a positive ΔL_1. Looking at g_2 we see it depends
on L_1 and L_e. By substituting eq. 4.7 into eq. 4.9 we can arrive at the following expression for
g_2

$$g_2 = 1 - \frac{L_2}{R_2} + \frac{1}{fR_2}(L_2 - (R_2 + f))L_1. \tag{4.13}$$

We can see that the change in g_2 with L_1 depends on whether $L_2 > R_2 + f$ or not. If we assume
that $L_2 > R_2 + f$, then g_2 increases with L_1 and vice versa.

Changing Thermal lens (R_2)

Only g_2 depends on R_2, $g_2 = 1 - \frac{L_1}{f} - \frac{L_e}{R_2}$. Therefore, if $L_e > 0$, then decreasing R_2 (increasing
the thermal lens strength) will decrease g_2. In the cavity presented in this report, however, L_e
is negative, which means that decreasing R_2 will increase g_2.

Changing L_2

All three parameters depend on L_2. By similar analysis to the section above it can be found
that if $\frac{L_1}{f} > 1$, then L_e will decrease with a positive ΔL_2. If L_2 increases, g_1 decreases, using
eq. 4.10. Eq.4.9 can be rearranged to the following, after substituting in eq. 4.7 again,

$$g_2 = 1 - \frac{L_1}{f} - \frac{L_1}{R_2} + \frac{1}{R_2}(\frac{L_1}{f} - 1)L_2. \tag{4.14}$$

Therefore, if $L_1 > f$, as L_2 decreases g_2 decreases and vice versa.

Example Cavities

To further understand how the cavity behaves and especially how the mode size at the back
mirror changes, an example cavity is used. The test cavity will have the following parame-

ters: $L_1 = 140\,\text{mm}$, $f = 70\,\text{mm}$ and $L_2 = 210\,\text{mm}$. To calculate and visualise the changing parameters, and their effects of the mode size throughout the cavity, a software designed by Dr William Kerridge-Johns in MATLAB based on the equations presented in Magni et al. [71] was used. The graphs of changing mode size and the diagrams of cavity with the intracavity mode presented in this section were calculated and generated using this software. Firstly, the effect of varying L_1 and how that effects w_2 with a varying thermal lens is assessed. Fig 4.2 shows how the beam waist size in similar cavities vary with the thermal lens, when L_1 is increased. It also shows where these cavities become stable and unstable as the thermal lens is increased, as the waist size asymptotes.
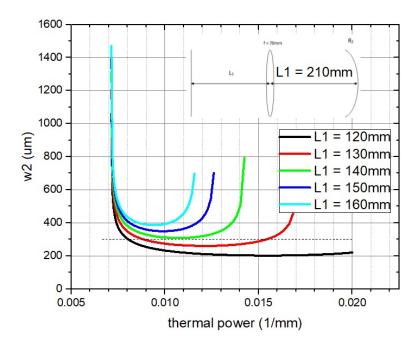
Figure 4.2: Graph of calculated w_2 (beam waist at the back mirror) against thermal power for several cavities. Each cavity differs only in the length of L_1. The dotted line shows the 300 μm mark, where the spot size of the intracavity mode would match the pump size.

Fig 4.2 shows that regardless of what L_1 is, each cavity becomes stable at the same thermal power. At this point $g_1 g_2 = 1$ for each cavity, and the intracavity mode will look like fig 4.3. From the figure we can see that the L_1 arm is collimated meaning that any change in the length of L_1 will not effect the L_2 arm. Furthermore, if the L_1 arm is collimated then the focus in the L_2 arm will happen at exactly 70 mm from the lens and the thermal lens has to have a value of L_2-f. If the thermal power gets any weaker the focus would be closer than 70mm to the lens and the beam in L_1 would be diverging towards R_1. In this scenario the cavity would be

unstable as R_1 is a plain mirror. From the previous section we know that g_2 is dependent on L_1 and if $g_1 g_2 = 1$ at the point the cavity becomes stable, we might expect this to change as L_1 changes. However, from eq. 4.13 we see that g_2's L_1 dependence is scaled by $(L_2 - (R_2+f))$. Therefore, if $L_2 = R_2+f$, then $g_2 = 1 - \frac{L_2}{R_2}$ and stays constant, which is why the cavity always becomes stable at the same thermal power, regardless of changes made to L_1.


```
Cavity Parameters
  R1 / mm          L1 / mm          f / mm          L2 / mm          R2 / mm
  1000000            140              70               210             140

  w1 = 1.42e+03 um           w3 = 1.42e+03 um          w2 = 2.83e+03
```
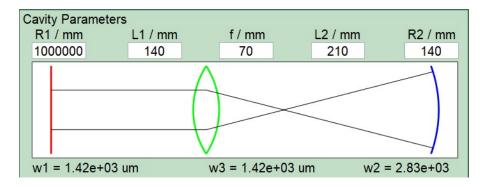
Figure 4.3:   Calculated fundamental mode size in example cavity showing intracavity mode just as the cavity becomes stable with decreasing radius of curvature of R_2 (increasing thermal lensing of a gain medium placed next to a mirror). Calculated and visualised using software developed by Dr William Kerridge-Johns.

Each cavity then goes unstable again at higher thermal powers, however, as L_1 increases the cavity goes unstable at a lower thermal power. At this point $g_1 g_2 = 0$ and a representative cavity mode is shown in fig 4.4. The beam in the L_1 arm is no longer collimated and comes to a point on R_1. The focus in the L_2 arm has moved towards R_2 and is now a distance of L_2-R_2 away from the lens. As the beam is essentially a point source from R_1 the lens formula can be used to describe the relationship as shown

$$\frac{1}{f} = \frac{1}{L_1} + \frac{1}{L_2 - R_2}. \tag{4.15}$$

As L_1 increases, the $1/L_1$ term decreases which means that the $1/(L_2$-$R_2)$ term has to increase to maintain the equality. The required value of R_2 therefore increases as L_1 increases, meaning the cavity goes unstable at lower thermal power as L_1 increases. From fig 4.2 we can also see that the minimum waist size (the lowest point on each curve) in the cavity increases as L_1 increases. This makes sense as $|L_e|$ increases with L_1 and remains constant with R_2, this is from eq. 4.11 that tells us that $w_2 \propto \sqrt{\frac{\lambda|L_e|}{\pi}}$.

The other component that we can vary in the cavity is the position of the intracavity lens, this changes the values of L_1 and L_2 but keeps the total cavity length the same. Fig 4.5 shows
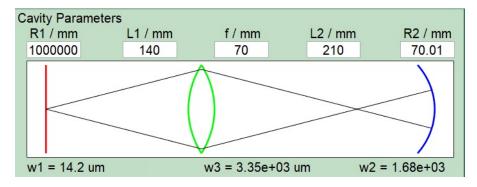
Figure 4.4: Calculated fundamental mode size in example cavity showing intracavity mode just before the cavity becomes unstable with decreasing radius of curvature of R_2 (increasing thermal lensing of a gain medium placed next to a mirror). Calculated and visualised using software developed by Dr William Kerridge-Johns.

how w_2 varies with the thermal power while changing the intracavity lens position.
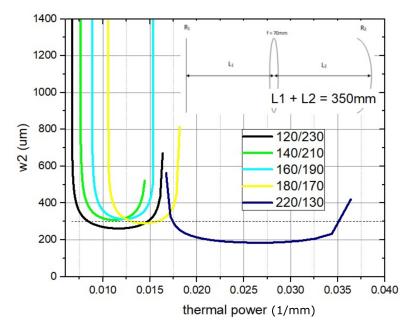
Figure 4.5: Graph of spot size w_2 against thermal power. Each cavity has the same total cavity length, however the intracavity lens is moving. The dotted line denotes the point at twhich the intracavity mode size at the crystal is equal to $300\,\mu m$.

The first thing to note is that the thermal power at which the cavity becomes stable at lower powers is shifting to the right. Very simply this is because L_2 is getting shorter, as L_1 gets longer, therefore $f + R_2 > L_2$ becomes true at shorter thermal lens values. The effective length depends on both L_1 and L_2, which explains why the minimum of each cavity's curve goes and the down with increasing thermal power. Fig 4.6 shows how the magnitude of the effective length of each cavity varies as L_1 increases (and L_2 decreases). Fig 4.6 shows that the magnitude of the effective cavity length peaks between $L_1 = 170\,mm$ and $180\,mm$. In fig
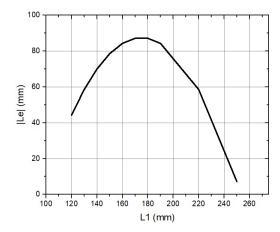
Figure 4.6: Magnitude of L_e changing with L_1, over the same range as L_1 changes in fig 4.5.

4.5, however, the highest sitting trough is roughly around $L_1 = 150/160 \, \text{mm}$, the change in the effective length is therefore not a perfect predictor of how the minimum waist size will change.

One thing that can be seen from both fig 4.2 and 4.5 is that the mode size at R_2 changes with thermal power. As the cavity becomes stable it starts at an infinite value, rapidly shrinks, come to a minimum and then increases again to infinity before becoming unstable. As R_2 changes only g_2 changes with it, while L_e and g_1 stay constant. So while the waist at R_2 is given by eq. 4.11, the shape of the curve is given by

$$\frac{g_1}{g_2(1 - g_1 g_2)}.$$

If we differentiate this with respect to g_2 and set it to zero, we get

$$-\frac{g_1(1 - 2g_1 g_2)}{(g_2 - g_1 g_2^2)^2} = 0.$$

From this we can see that the curve of w_2 is at a minimum when $g_1 g_2 = 0.5$. If $g_1 g_2 > 0.5$, w_2 decreases with thermal power and vice versa. Using $g_1 g_2 = 0.5$ at the minimum we can come up with an expression for the minimum w_2 of a cavity operating in this regime.

$$w_{2,0} = \sqrt{\frac{\lambda |L_e|}{\pi g_2}}, \tag{4.16}$$

where $w_{2,0}$ is the minimum w_2 for a given cavity.

4.4   Vortex laser using the VOC

The key feature of the imbalanced Sagnac interferometer VOC is that a controllable fraction of the incident Gaussian power is transmitted into the vortex output. The remaining power is

reflected in a beam that has approximately the same intensity and phase distribution as the incident Gaussian, and can be aligned to be collinear with the input beam. This allows it to function as an output coupler in a laser cavity, where the internal Gaussian mode is preserved as a stable cavity mode whilst extracting the vortex output. If the VOC was used externally to a laser the reflected Gaussian beam power would be wasted as loss and the conversion efficiency would be equal to the transmission; however, by returning this reflected power to the oscillator to be amplified as a part of the cavity the conversion efficiency is approximately 100%.

4.4.1 Experimental vortex generation from a laser

In this work we experimentally demonstrate the use of the VOC to output an LG_{01} type mode from a linear laser resonator using the cavity design shown in Fig. 4.7. The cavity was formed with a high reflectance flat back mirror (BM), Nd:YVO$_4$ crystal, dichroic turning mirror (TM1), intracavity lens of focal length f = 150 mm for mode size control, and the VOC completed the linear cavity by acting as the end reflector. The VOC had a perimeter of 200 mm and an internal parallel AR plate with a thickness of 3 mm. The gain medium was a 2 mm square by 4 mm long 0.5 at.% doped Nd:YVO$_4$ crystal operating on the c-axis at 1064 nm, with the internal laser mode and outputs being linearly polarised parallel to the c-axis throughout this work. It was end-pumped through the dichroic TM1 with a nominal 808 nm fibre delivered laser diode module with up to 13.6 W of optical power. The crystal absorbed 78% of the incident pump power due to an actual central pump wavelength of 806 nm that did not accurately match the 808 nm absorption line in Nd:YVO$_4$. The laser cavity could be redirected away from the VOC to use a standard plane output coupler (OC) by inserting a turning mirror (TM2), where the distance from TM2 to the OC was equal to the path length between the insertion point of TM2 to M2.

The transmission T of the VOC is defined as the fraction of incident power from the laser cavity that was converted into vortex output. The intra-cavity power was deduced from the known 0.7% transmission of the BM. The VOC was first operated with a transmission of T = 16% at 8.1 W of absorbed pump power, which gave a vortex output power of 2 W. The intra-cavity mode and vortex output intensity profiles are shown in Fig. 4.8. The vortex output coupler had negligible effect on the intra-cavity mode, which remained approximately TEM$_{00}$
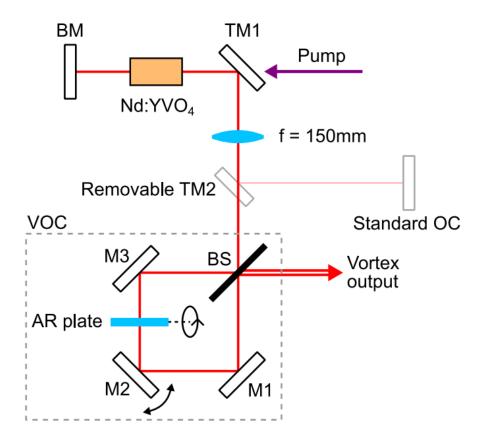
Figure 4.7:   Diagram of experimental setup of the first vortex laser, with the VOC (in the grey dashed square) as the output coupler. Also showing the redirection of the cavity for comparison with a standard output coupler. The arrows by the anti-reflection (AR) coated glass plate and by mirror M2 show how they were rotated to control the vortex output.

with an $M^2 < 1.3$.

The M^2 beam quality parameter can be used to determine the likely dominant transverse mode component in the vortex output, where a pure LG_{01} mode has $M^2 = 2$. The average beam qualities of both the left and right handed vortex outputs were $M^2 = 2.07$ in each axis, which indicates a close match to the intended LG_{01} mode. To further assess the quality of the vortex output the intensity profile was compared to that of the theoretical LG_{01} mode. Circular cross sections were taken to calculate the average and standard deviation of the beam intensities at different radial distances from the beam centre. The measured and fitted theoretical intensity profiles are shown in Fig. 4.9. The experimental vortex outputs were excellent matches to the LG_{01} mode for both left and right handed outputs, which verifies their high purity. The intensity minima were both below 2% of the peak intensities, limited by the accuracy of the CMOS camera measurement equipment. The beams had excellent symmetry, with both having a standard deviation of 6% in intensity at the peak. The central intensity minima is expected,
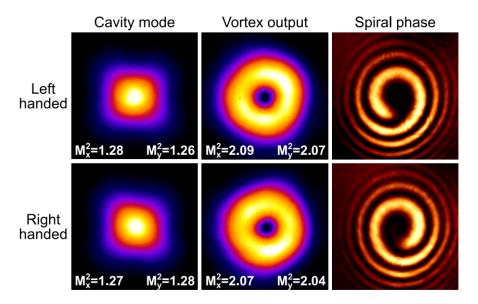
Figure 4.8: Snapshots of the spatial profiles of the intracavity mode and vortex output in both left and right handed operation, when operated with a transmission of 16%. The last column shows a spiral interference pattern of each handed vortex.

as complete destructive interference at the central point is inherent in the conversion process. A radially uniform intensity profile, like a uniform M^2, confirms that the canonical condition is being met and that the small angle approximation made in the conversion is still valid.
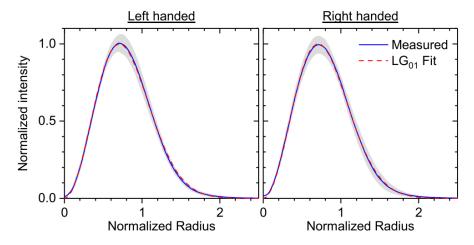
Figure 4.9: The measured average intensities (shown in blue and normalised to the peak) against the radial distance from the centre (normalised to the fundamental Gaussian beam radius) of the left and right handed vortex outputs shown in fig. 4.8, with one standard deviation either side (shaded grey). Fitted theoretical LG_{01} profile overlaid (dashed red).

To reveal the vortex phase structure of the output, a Mach-Zehnder interferometer was constructed to self-interfere the output with a curved wavefront reference beam. The single spiral interferograms in Fig. 4.8 reveal a first order vortex phase structure. The handedness of the vortex output produced by the VOC is determined by the relative signs of d and θ, which

makes the handedness controllable by reversing either the AR plate or M2 rotation direction. Reversing the vortex handedness did not affect the vortex output power or intensity profile, see Fig. 4.8, with the handedness reversal being confirmed with the opposing spiral directions in the interferogram. These results confirm that the vortex handedness control is fully independent from the internal Gaussian mode, it can be performed in place without replacing intra-cavity optics or requiring realignment of the laser cavity.

The beam propagated metres before reaching the Mach-Zehnder interferometer, over which period it passed through several lenses, leading to the conclusion that the generated vortex mode propagated stably. This is expected as Laguerre Gaussian modes propagate stably and the constituent Gaussian beams will never diverge away from each other (see 3.1).

To fully determine the mode components of the vortex outputs modal decomposition methods can be used [65]. However, our analysis shows that the measured vortex outputs had excellent intensity matching to the LG_{01} mode, well within one standard deviation, with the correct spiral phase. This is sufficient to confidently conclude that the outputs have a high LG_{01} mode component.

The performance of the VOC laser was compared to an equivalent laser with a standard partially reflecting mirror output coupler (OC) by inserting TM2 to redirect the cavity, see Fig. 4.7. The laser output power versus input pump power is shown in Fig. 4.10 for the VOC and standard OC lasers, where the VOC was matched to the standard OC transmission of 16 %. The VOC and standard OC lasers had almost identical laser thresholds at $1\,\mathrm{W}$ of pump power, which highlights the low insertion loss of the VOC. The slope efficiencies of the VOC and standard OC lasers were 34 % and 40%, respectively. This resulted in similar maximum output powers at $10.7\,\mathrm{W}$ pump power absorbed of $3.2\,\mathrm{W}$ and $3.7\,\mathrm{W}$, respectively. At the highest pump power the standard OC laser, designed to operate on the fundamental mode, had an M^2 = 1.5, and this increasing higher order mode content may have improved the mode matching efficiency to the pumped region giving it a higher efficiency than the VOC laser. It has been shown that a Sagnac ring with an imaging asymmetry creates a larger loss for higher order transverse modes [72], so it is likely that the VOC also suppresses higher order modes.

The efficiency of the VOC laser was limited to that of the standard OC cavity in this work.
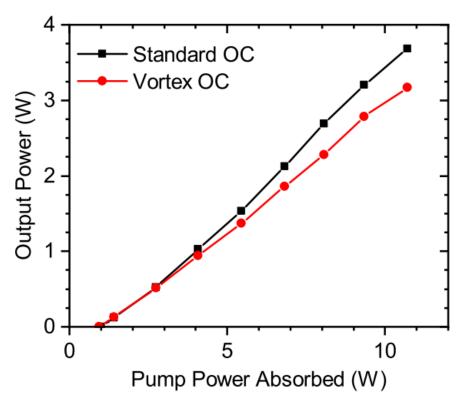
Figure 4.10: The output power of the laser, in the vortex configuration and with the flip-in standard output coupler, against absorbed pump power at 16% transmission.

These first results have demonstrated that, if implemented correctly, the VOC laser will operate at the same powers and efficiencies of standard linear cavities, therefore it will be capable of operating at the same elevated powers and efficiencies of more optimised cavity designs. These results highlight the suitability of the VOC as a simple replacement for a standard OC and its inherently low loss design from non-absorbing and non-diffracting components.

A key benefit of incorporating the VOC device inside the laser cavity is the increase in vortex generation efficiency when compared to external use. As a simple example, if the VOC was used externally on the output of the standard OC laser in Fig. 4.10 with T = 16%, a vortex beam of power 0.59 W would have been generated. This is over a factor of 5 times less than the power from the VOC laser of 3.2 W. However, incorporating the VOC into the cavity provides benefits beyond just efficiency increases. If used externally, the VOC requires precise alignment of the input beam to the device, in particular ensuring a beam waist is formed on M2. When used internally, these alignments are automatically satified as a result of the conditions for a stable cavity mode.

4.4.2   Transmission of the VOC

A key property of an output coupler is its transmission, which in this instance is the fraction of input Gaussian power that is converted into the vortex output. The continuously variable transmission is unusual in an output coupler design and is advantageous for optimising the output power from a laser [42]. To demonstrate this feature the output coupler transmission was varied from 3% to 41% at a fixed input pump power of 4.1 W, with the resulting vortex powers shown in Fig. 4.11. It should be noted that changing the transmission was a simple procedure using only two controls - the AR plate and mirror M2 rotation angles to control and maintain the $|d| = \pi w_0^2 |\theta| / \lambda$ condition. The transmission was continuously tunable, with an optimum power output found at T = 22%.
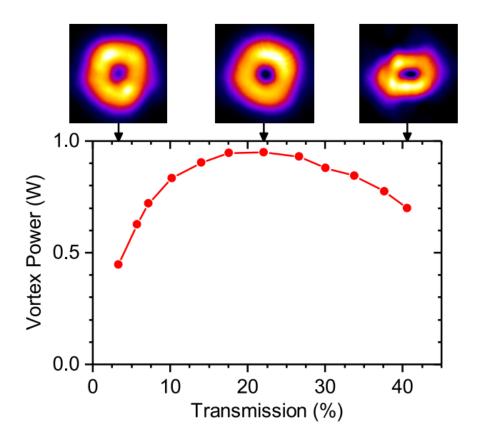
Figure 4.11:   The output vortex power against the VOC transmission for 6.4 W of absorbed input pump power. The far field vortex intensity profiles at various transmission values are inset above.

The vortex intensity profiles are shown at selected transmission values in Fig. 4.11. From T = 3% to 30% the output vortex maintained good symmetry as expected from the theory. Above T = 30% the vortex intensity profile became stretched in the horizontal plane as predicted by

the theoretical calculations in Fig. 3.2. The central intensity minimum of the vortex arises from the destructive interference condition of the Sagnac interferometer, so it maintained its high contrast to the peak intensity. For example, at the maximum transmission of T = 41% the central intensity minimum was below 2% of the peak. It was experimentally verified with spiral interferograms that the output maintained its vorticity for all transmission values, which is consistent with the theoretical beam profiles shown in Fig. 3.2 that have spiral phase profiles.

Both the rotation angles of M2 and the AR plate are functions of the beam waist size on M2 through the VOC transformation condition $|d| = \pi w_0^2 |\theta|/\lambda$. The Gaussian beam waist radius, on the mirror surface, was approximately $w_0 = 150\,\mu m$ throughout this work, which for a VOC transmission of T = 20% gives $\theta/2 = 0.4\,mrad$ for M2 and $\psi = 3°$ for the AR plate. These are both easily and accurately achievable with common optical mounts, in particular the M2 rotation is within typical alignment tolerances for a laser cavity mirror and did not need frequent realignment.

The concept of interferometric mode transformation presented in this work is not limited to the production of vortex modes as in the VOC. Simply by altering the input mode or the interference properties of the beams diverse and unique outputs can be generated directly from lasers. For example, the VOC in this work can be configured to output a HG_{10} or HG_{01} (Hermite-Gaussian) mode if either of d or θ are zero, respectively, see Fig. 4.12.
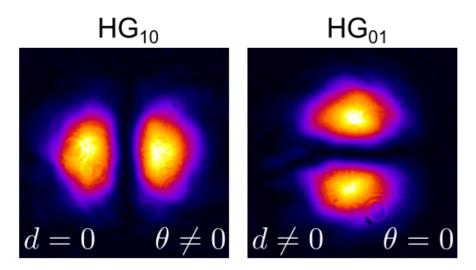
Figure 4.12: Measured intensity profiles of the output of the VOC while operating either d or θ misalignments in isolation. These outputs correspond to the first order Hermite-Gaussian modes, HG_{10} and HG_{01}.

4.5   Pulsed vortex laser

To have a better handle on the cavity geometry dynamics, the gain medium was moved next to the back mirror. This allowed the back mirror/gain medium combination to be approximated as a curved mirror, because of the thermal lensing in the gain medium, and the cavity to be approximated as in Magni et al. [71]. With a known pump spot size, the cavity geometry could be better designed to maintain overlap between the intracavity mode and the pump mode in the gain medium. A further optical element, an acousto-optic modulator (AOM), was also added to allow the cavity to be pulsed.

The AOM is a transparent element connected to an electrical signal generator which periodically creates an acoustic wave travelling through the AOM. This acoustic wave temporarily changes the refractive index of the AOM, causing any beam travelling through it to refract differently. When aligned correctly within a cavity, the AOM can be used to periodically divert the cavity beam enough to cause the cavity to stop lasing. The AOM allows for Q-switching by modulating the loss of the cavity and while the cavity is unable to lase, the pump continues to deposit energy into the gain medium. The lack of lasing causes energy to build up in the gain medium, which is then released in a pulse once the acoustic wave has propagated through the AOM and the intracavity mode is no longer diverted.

The two laser cavities that were operated in this study are shown in Fig. 4.13: a standard linear laser cavity with plane mirror output coupler (OC), Fig. 4.13(a), and a variant of this cavity with a vortex output coupler (VOC), Fig. 4.13(b).

In the linear cavity, used as a starting point for the vortex laser, the gain medium was a 3x3x5 mm 0.5 at.% doped Nd:YVO$_4$ crystal, operating on the c-axis at 1064 nm. The cavity was formed between the back mirror (BM) and a 20% transmission plane output coupler (OC). An intracavity lens (f = 70 mm) provided mode size and stability control. An acousto-optic modulator (AOM) was used to Q-switch the cavity for pulsed operation. The gain medium was placed 1 mm from BM, the BM to lens distance was 225 mm, and the lens to OC distance was 80 mm. The Nd:YVO$_4$ crystal was end-pumped by a fibre-delivered laser diode module, with a nominal wavelength of 808 nm, through BM, which transmitted 808 nm and reflected 1064 nm. The pump beam was focused into the crystal to a minimum waist radius $w_p = 300\,\mu\text{m}$ and

with a super-Gaussian intensity profile. The pump beam propagation parameter was $M^2 = 35$. A maximum pump power of $12.8\,W$ was used, or $12.2\,W$ absorbed power accounting for 95% absorption in the crystal. The maximum pump power was set as a safety limit as there was crystal fracture observed with our $Nd:YVO_4$ crystal in its crystal holder when operating at pump powers above this due to thermal stress in the gain medium but this is not expected to be a fundamental limit.
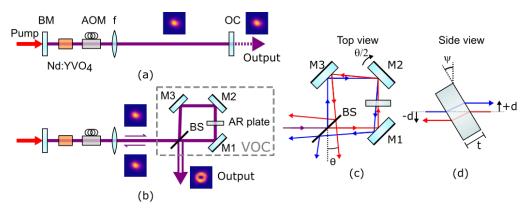
Figure 4.13: The laser cavity and VOC operation. (a) Standard linear cavity, composed of: high reflectance (HR) back mirror (BM), Nd:YVO4 crystal, acousto-optic modulator (AOM), intracavity lens and output coupler (OC). (b) Converted linear cavity with the VOC. The lens to OC and lens to M2 distances are matched in both cases. The inset intensity profiles show the beam at different points. (c) Schematic of a top view of the VOC showing how an angular misalignment is imparted between the two counter-propagating beams. (d) Side view of the AR plate, which can be tilted to introduce a spatial separation between the two counter-propagating beams.

The linear cavity was converted into a vortex source by removing the OC and replacing it with a VOC, as shown in Fig. 4.13(b). The VOC cavity was made geometrically identical by placing the mid-mirror M2 of the Sagnac interferometer at $80\,mm$ from the lens, identically matched to the lens to OC distance in the initial linear cavity. This meant that the mode size and cavity stability conditions were unchanged, so the linear cavity optimisations also applied to the VOC laser.

To operate the VOC as part of the laser cavity, so that it outputs a vortex, the canonical condition and ratio magnitudes must be maintained. In a laser, the varying thermal lens in the crystal can change the intracavity mode size at M2. Therefore, to maintain the canonical condition and transmission of the VOC output, small adjustments to θ and d were necessary when changing the pump power. In this investigation, the canonical condition was obtained

by monitoring the output mode symmetry, where maximum azimuthal symmetry occurred when the canonical condition was satisfied. The transmission of the VOC was determined experimentally by measuring the intracavity power from the small known transmission fraction of M3.

4.6   Q-Switched linear and vortex laser results

The standard linear cavity, see Fig. 4.13(a), was operated with a plane mirror output coupler with 20% transmission. At 150 kHz Q-switching rate, the average output power against absorbed pump power is shown in Fig. 4.14 (black circles). At 12.2 W of absorbed pump power the average output power was 5.4 W in a Gaussian mode, $M^2 = 1.20$, and it had a slope efficiency of 49%.

To directly compare the performance of the VOC laser, the VOC was also operated with 20% transmission. The vortex laser results for 150 kHz Q-switching rate are also shown in Fig. 4.14 (red squares). The average vortex output power at 12.2 W pumping was 5.1 W, and it had a slope efficiency of 46%.
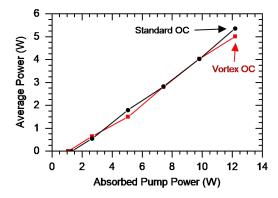
Figure 4.14:   Average output power at 150 kHz repetition rate and 20% output coupling against absorbed pump power. The VOC cavity results are in red and the linear cavity results are in black.

The VOC cavity and the linear cavities had similar lasing power, threshold and slope efficiency, showing that the implementation of the VOC negligibly impacted the cavity efficiency. This result shows the potential for the VOC as a general methodology for converting a standard TEM_{00} laser cavity into a vortex laser. The VOC cavity efficiency was limited to that of the linear cavity, which is expected as the VOC cavity geometry was equivalent to the linear cavity

and therefore had similar mode to pump size conditions. The equivalence of the plane output coupler and VOC, and the required fundamental intracavity mode, means that the VOC cavity can be designed and modelled using standard ABCD matrix analysis.

To operate the VOC the amount of shear and angular displacement introduced in the recombining beams must be matched to the beam waist size and the required transmission, as determined by eq. 3.6. When operating with a measured transmission of 20% at 12.2 W of absorbed pump power the beam waist radius at M2 was measured to be 100 μm, and the AR plate had been rotated by ψ=2.0° giving d=36.9 μm. The normalised displacement was therefore d/w_0=0.36. Using eq. 3.6 this gives a theoretical transmission of T=20%, assuming the canonical condition is exactly satisfied, which precisely matches the measured transmission. From the values of d and w_0, it can be inferred that the relative horizontal beam angle was θ = 1.2 μrad, although this was not measured directly.

To further investigate the pulsed vortex laser the Q-switching repetition rate was varied from 25 to 175 kHz. The average vortex power against Q-switching rate is shown in Fig. 4.15(a). The average power of the vortex asymptotically increased with increasing repetition rate, from 4.5 W at 25 kHz to 5.1 W at 175 kHz.
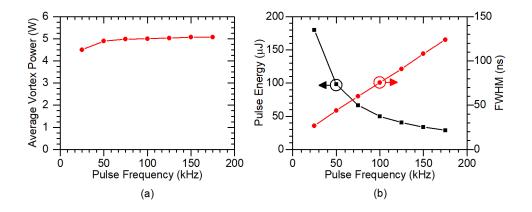
Figure 4.15: (a) Average vortex power of the VOC cavity against repetition rate of Q-switching at 12.2 W of absorbed pump power. (b) Pulse energy (black) and pulse full-width half-maximum (FWHM) duration (red) of the VOC cavity against pulse repetition rate at 12.2 W of absorbed pump power.

The pulse energy and pulse duration against Q-switching rate is shown in Fig. 4.15(b), in black and red respectively, at 12.2 W of absorbed pump power. At 25 kHz, the pulse energy

was $180\,\mu J$ with a pulse duration of $26.6\,ns$, and at $150\,kHz$ the vortex pulses had an energy of $34\,\mu J$ and a duration of $108\,ns$. The spatial profile of the vortex output at $12.2\,W$ of absorbed pump power and 150 kHz is shown in Fig. 4.16(a). The vortex had a beam propagation factor $M^2 = 2.26$. The intracavity mode was analysed by accessing the leakage from mirror M3 in the VOC, which revealed the intracavity mode had an $M^2 = 1.12$, Fig. 4.16(b). These values are close to the theoretical M2 for the LG_{01} mode ($M^2 = 2$) and a fundamental Gaussian ($M^2 = 1$). For comparison, with the same pumping and Q-switching conditions the standard linear cavity had an $M^2 = 1.20$.

To further verify the vortex mode quality and confirm the pure handedness the phase structure was measured using the method laid out by Takeda et al. [34]. This uses the interference of the vortex beam with a tilted planar reference beam to retrieve the field phase information, which was performed with a Mach-Zehnder interferometer. The retrieved phase images of the vortex outputs in the two handedness states is shown in the insets of Fig. 4.17, with (a) and (b) showing the two handedness results. The graphs show the corresponding circular cross section of the phase profile that was centred on the beam axis and at a fixed radius, matching the peak intensity of the annular ring. The retrieved phase images show the characteristic phase singularity in the centre, with an azimuthal phase variation totalling 2π around the beam centre. The circular cross sections verify that these match well to the theoretical linear phase change of the LG_{01} mode, overlaid in red. The combination of close intensity and phase characteristics with the LG_{01} mode verify the high purity of vortex mode generated.
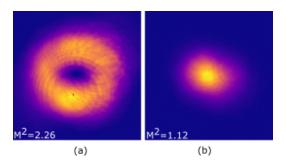
Figure 4.16: Spatial intensity profiles of the a) the vortex output and b) the intracavity mode of the VOC cavity. The M^2 of each beam is inset.

The handedness of the vortex output was switched during operation by inverting the spatial displacement d through reversing the tilted AR plate angle ψ. By comparison of Figs. 4.17(a)
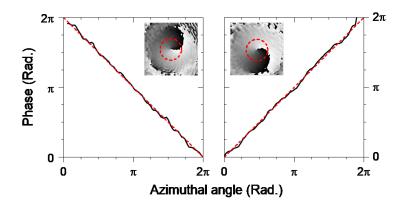
Figure 4.17: (left) Measured phase profile of a circular cross section around the phase singularity of the vortex with right handedness and (right) measured phase profile of the vortex with left handedness. The retrieved phase images for each handedness is inset. The measured phase data is shown in black, with the theoretical phase profile in red.

and 4.17(b), it is clear that this reverses the handedness of the vortex, without any loss in quality. Additionally, there was no observed power loss incurred by switching. The beam propagation factor of the vortex after the switch was maintained with $M^2 = 2.31$ (compared to $M^2 = 2.26$), and the intracavity mode had $M^2 = 1.11$ (compared to $M^2 = 1.12$), values within the measurement accuracy.

4.7 Higher order mode suppression by VOC

It was observed experimentally that the beam propagation factor of the intracavity beam of the VOC laser was lower than that of the linear cavity. The theory behind the VOC is based on a perfect fundamental Gaussian input, despite this the VOC still produced high quality vortices from cavity geometries not optimised for fundamental Gaussian oscillation. This suggested that the VOC improved the intracavity beam quality, allowing it to function as intended.

To better understand the intracavity mode conditions needed for the VOC laser, the fundamental mode size at the gain medium was systematically reduced to mismatch the mode and pump diameters. This was achieved experimentally by moving the intracavity lens towards the BM. The effect of the lens movement on the power and beam propagation factor of both the standard linear cavity and VOC laser cavity were investigated.

The power and beam propagation factor results for the standard linear laser are shown in Fig. 4.18(a), including inset beam profiles at certain lens positions. The beam propagation

factor increased with lens position from $M^2 = 1.38$ to $M^2 = 7.32$. This was expected because the fundamental mode size was becoming increasingly smaller than the pumped region allowing oscillation of higher-order modes, whilst the overall intracavity mode size at the pumped region was measured to remain constant. The transition from a Gaussian to an increasingly top-hat beam profile resulted in better matching to the top-hat pump profile, which is reflected in the output power increasing from 5 W to 5.4 W from 0 mm to 17 mm lens position. With further increasing lens position the output power decreased, which may have been the result of a higher proportion of the intracavity mode overlapping with the aberrated wings of the thermal lens.
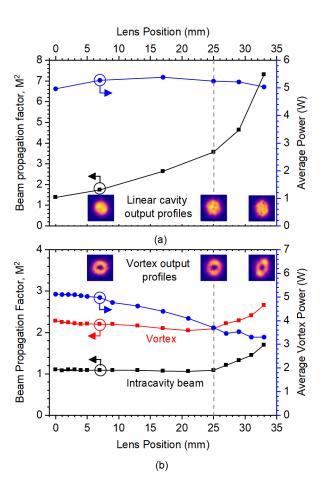
Figure 4.18: (a) The beam propagation factor (M^2) (black) and average power output (blue) of the linear cavity against detuning (lens position). (b) M^2 of the vortex (red) and intracavity beam (black) of the VOC and the average power of the vortex (blue) against detuning of the cavity. Dashed line highlights the point at which the VOC is no longer able to suppress the higher order modes in the cavity. Beam profiles for the VOC and linear cavities are inset, corresponding to the lens position at 7 mm, 25 mm and 33 mm.

The equivalent effects of intracavity lens movement in the VOC cavity are shown in fig.

4.18(b), including inset beam profiles at certain points. In this figure the beam propagation factor is shown for both the output vortex and the intracavity beam. The results show two clear regions of operation with a transition point at a lens position of 25 mm, highlighted by a vertical dashed line in Fig. 4.18. The initial trend, below a lens displacement of up to 25 mm, was that the intracavity beam stayed approximately fundamental mode HG_{00} and the vortex maintained its ideal value near $M^2 \approx 2$. This high spatial purity was at the expense of some output power that reduced from 5 W to 3.8 W over the range. The measured intracavity fundamental mode radius decreased from 270 µm to 155 µm in this range, resulting in poorer gain region extraction (pump mode size 300 µm) and so a lower efficiency.

After 25 mm lens displacement, the VOC cavity could no longer maintain the fundamental Gaussian mode seen by its increasing M^2. The intracavity beam became increasingly multimode to fill the gain region, which resulted in a reduced rate of power loss. However, this interfered with the VOC operation, and the output vortex was also no longer LG_{01} shaped and the output beam M^2 increased above 2.

The lens position at the transition point of 25 mm, with intracavity $M^2 = 1.1$, corresponded to the equivalent standard linear cavity having an $M^2 = 3.60$. This shows that the addition of the VOC to the cavity caused it to maintain a high-quality fundamental Gaussian mode despite poor pump to mode size matching. In fact, it has been previously predicted that an unbalanced Sagnac interferometer has a higher loss for higher order modes [35]. Our results show a similar behaviour, so we attribute our results to the VOC having a higher transmission for higher order modes. This means the VOC will supresses these modes in the cavity due to their higher round-trip higher loss. In this way, the VOC spatially optimises the cavity with a self-mode-filtering due to the interferometric behaviour of the VOC. This provide a benefit that it does not necessarily require a fully optimised starting cavity and, additionally, this means that it could also reduce minimise spatial degradation of the intra-cavity mode during power scaling efforts.

4.8 Vortex laser employing spherical aberrations in the laser crystal

The cavity used is shown in fig. 4.19. The cavity is plane-plane and end pumped, with an intracavity lens (f = 70 mm) and the gain medium (Nd:YVO$_4$, 3x3x5 mm) approximately 1 mm from the back mirror. The gain medium was pumped at 808 nm through a dichroic back mirror, which is HR at 1064 nm. The output coupler had a transmission of 15% and the Q-switching was achieved using an acousto-optical modulator, which was 30 mm long and was placed with its right face 73 mm from the back mirror. The distance from the output coupler to the intracavity lens, distance L_1, was 90 mm and the distance from the intracavity lens to the back mirror, L_2, was 230 mm. The cavity stability parameters, g_1 and g_2, are both negative in this set up. In the diagnostics set up a dichroic mirror is used to filter out any pump light which was not absorbed by the gain medium and a AR/AR wedge, which is used to pick off a small amount of the beam's power for the camera and MZI. These two elements account for a 7% loss in power at the power meter and has been accounted for in the presented results.
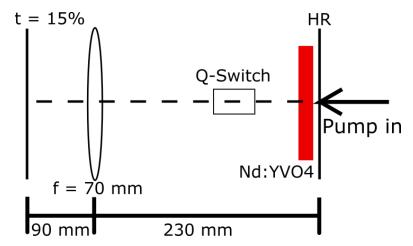
Figure 4.19: Cavity set up used. Gain medium pumped through a plane, dichroic back mirror, HR at 1064 nm. Plane output coupler, with a transmission of 15%. An intracavity lens, with focal length 70 mm, maintains cavity stability. An acousto-optic element is used for Q-switching.

4.8.1 Pump specifications

The pump module used was a 60 W unit, which lased at 808 nm. The collimated pump beam was focused onto the gain medium with a 200 mm lens, resulting in 300 µm beam radius at the focus with a Rayleigh length of 9.5 mm. The pump beam had an $M^2 = 35$. Fig. 4.20(a) shows

power in against power out for two plane-plane cavity, with lengths 100 mm and 200 mm. In both cavities the gain medium was position directly next to the back mirror, as in fig. 4.19. A snapshot of the pump beam at focus is shown in fig. 4.20(b). The beam appears to have a top hat profile.

(a)   (b)
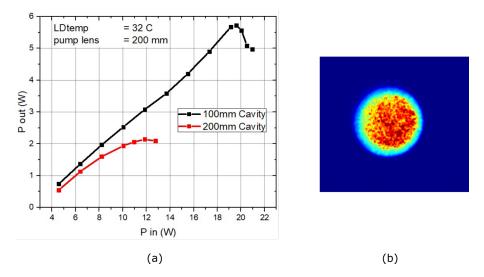
Figure 4.20: (a) Power out against pump power in for two plane-plane cavities, with lengths 100 mm and 200 mm. The pump diode was cooled to 32 °C and the pump beam focused into the gain medium with a 200 mm lens. (b) Snapshot of the pump beam at a focus.

The graph shows that the 200 mm cavity goes unstable at approximately 12 W of input power and the 100 mm cavity goes unstable at approximately 19 W. This allows us to estimate the strength of the thermal lens in the gain medium at various pumping powers. The results shown in fig. 4.20(a) were taken while the pump diode was being cooled to 32 °C. The subsequent results presented were obtained while the pump diode was being cooled to 38 °C. However, the observed thermal lens strength should still be valid to provide an approximate estimate. The pump beam was focused onto the gain medium with a 200 mm lens, as it was for results presented in the Results section.

4.8.2 Spherical aberration vortex results

A vortex was achieved with both continuous and pulsed operation. The results at 14.4 W of pumping are shown in fig. 4.21. The continuous beam had an output power of 6.04 W and an $M^2 = 2.22/2.18$, which is close to the canonical vortex beam quality of 2. The spiral interference pattern for the continuous operation shows that the vorticity is not pure, which is seen from the disjointed rings. The pulsed vortex had an average output power of 5.79 W at 100 kHz

repetition rate and an M^2 of 2.18/2.18. The handedness of the pulsed operation vortex is also more pure, with the disjointed rings almost completely re-joining. This suggests that the Q-switching, increases the mode purity and handedness at the loss of some power. In both pulsed and continuous operation, the mode stays stable through the focus.

The pulsed and continuous operation also have very similar efficiencies. Fig. 4.22 shows the absorbed pumped power against the continuous and average output power of the continuous and pulsed operation respectively. The Q-switching reduced the slope efficiency from 46% to 44.5%, and increased the lasing threshold from 1 W to 1.2 W of absorbed pump power.
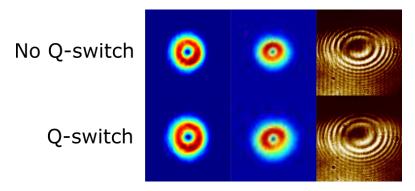
Figure 4.21: Snapshots of the vortex in the far-field, at its focus and its interference pattern with a spherical wave for both Q-switched and non-Q-switched operation.
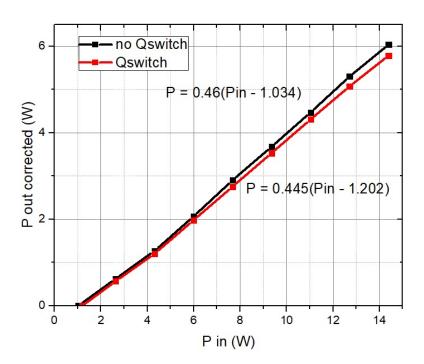
Figure 4.22: Vortex power out against pump power in for the cavity during non Q-switched operation (black) and Q-switched operation (red). The vortex power quoted for the Q-switched operation is the average power.

Fig. 4.23 shows the average power against absorbed pump power for the Q-switched operation at 100 kHz again, with snapshots of the mode at different pump powers inset. These show that the vortex persists from 14 W down to threshold. All optics were translated to ensure that there was no spot defect creating the singularity in the middle of the mode.
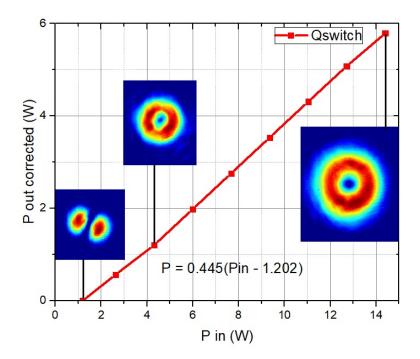
Figure 4.23:   Average vortex power out against absorbed pump power. Inset beam snapshots show the beam at threshold, at 4.3 W and at 14.4 W.

The repetition rate of the Q-switching was varied from 50 kHz to 200 kHz. The lower limit of 50 kHz was chosen to protect the optics and gain medium from damage and the upper limit of 200 kHz was chosen as the pulse stability started became too poor beyond it. Fig. 4.24 shows the pulse shapes. The trigger threshold had to be reduced at higher repetition rates, which is why the pulses are not all zeroed. The diagram does however show that the pulse duration and pulse energy change with the rep. rate. This is shown more clearly in fig. 4.25. The graph shows that the pulse duration, represented by its FWHM value, increases with repetition rate, from 37 nm at 50 kHz to 97 nm at 170 kHz. The outlier to this is at 200 kHz where the pulse duration decreases to 96 nm again, however the standard deviation at this point is 33%. The pulse energy decreases with repetition rate, as expected, from 110 µJ down to 30 µJ.

Finally, it was observed that the handedness of the vortex could be adjusted, and even switched, by adjusting the horizontal control of the output coupler. Fig. 4.26 shows the right and
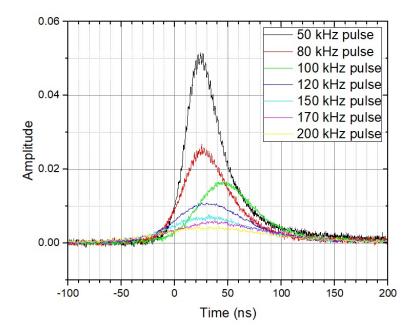
Figure 4.24:   Pulse shapes at 14.4 W of pumping at varying repetition rates. At higher rep. rates the trigger threshold had to be decreased, which is why the pulses are not all zeroed at the same place.

left handed vortexes, with their corresponding spiral interference patterns. Both interference patterns show a distinct spiral direction, indicating that most of the modal power was probably in a single handedness. However, the horizontal line across the centre of slightly misaligned fringes is the result of modal impurity, due to the presence of the opposit handedness. Using the mirror angle to change the handedness selection also resulted in a degradation of the spatial mode intensity pattern. This is reflected in the average power output, which dropped from 5.79 W in right handed operation to 4.72 W in left handed operation. The pulse width also increased to 69 ns.

4.9   Chapter summary

This chapter provides an overview of vortex laser literature, where many techniques suffer from poor efficiencies, poor power scaling or difficulties in handedness selection. A brief overview of solid-state laser design is also presented with some added analysis of cavity mode size it specific cavity configurations. Experimental results from three cavities were then presented.

In the first cavity presented, it was demonstrated that a Sagnac interferometer could be implemented as a VOC in a cavity to convert the typical HG_{00} internal mode of well optimised Gaussian laser cavities into an LG_{01} type vortex output. The vortex mode generated had an
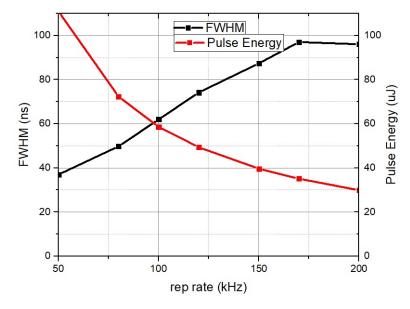
Figure 4.25: Pulse width expressed as full width at half maximum (black, left-axis) and pulse energy (red, right-axis) against pulse repetition rate.

excellent average beam quality of $M^2 = 2.07$, and the handedness was fully determined and controllable through a single control on the Sagnac interferometer. The intra-cavity mode remained approximately Gaussian. The transmission of the output coupler was continuously adjustable and was used to optimize the laser output power. The design utilised a Sagnac interferometer, making it robust against environmental perturbations and suitable for use with broad bandwidth or wavelength tunable lasers. This technique only requires a beamsplitter and mirrors so it can be used with any laser gain medium in wavelength ranges that may not be accessible with other methods, for example because the required optics or pump geometries are not available. It could replace the output coupler of any fundamental mode linear laser cavity to convert it into a vortex source.

In the second cavity presented, it was demonstrated that the VOC functioned without issues in a pulsed cavity. An average power of 5.1 W was achieved at 150 kHz pulse frequency, with a slope efficiency of 46%. The vortex also had an average beam quality close to the theoretical ideal of $M^2 = 2$ and phase retrieval revealed that the phase structure of the vortex closely matched the phase structure of an LG_{01}. The handedness was fully determined and configurable during operation with a single control (tilt-plate) in the VOC. It also offers variable output coupling for cavity optimisation. The VOC is shown to suppress higher order modes in the cavity with a self-mode-filtering action, which means it can operate as part of a non-ideal
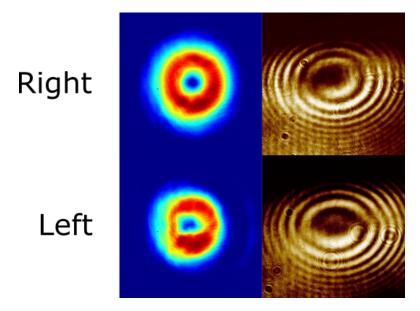
Figure 4.26: Snapshots of the beam profile in right and left handedness, accompanied by the corresponding observed spiral interference patterns, at 100 kHz repetiton rate.

cavity. The VOC can replace the output coupler of any fundamental Gaussian mode cavity, and we have also shown that it effectively operates in a high quality mode even in a sub-optimal cavity operating in multimode $M^2 = 3.6$. This makes it a highly effective solution for high power, wavelength tunable vortex lasers. Therefore, the VOC could be used to convert any high-power solid-state laser operating in fundamental mode or close to fundamental mode into a vortex laser, for example in systems based on thin-disk technologies [73, 74] . Furthermore, as an alternative use, the VOC could be implemented solely for its property of acting as a self-filtering-mode selector in a laser to improve the fundamental Gaussian output.

In the third cavity presented, it was demonstrated that under certain conditions the cavity mode could be forced to oscillate on a vortex mode. The vortex mode persisted when the cavity was pulsed and the handedness could be switched by tilted the back mirror of the cavity. However, from the interference patterns, it can be seen that the mode is impure and that both handedness's are present.

Chapter 5

Power scaling the vortex laser

Following the successful results of the last chapter, this chapter investigates power scaling the vortex laser using a Sagnac interferometer as an output coupler (dubbed vortex output coupler, VOC). The thought process in designing the new cavity is presented, as well as power scaled results.

The experimental cavity designed employed a new Nd:YVO$_4$ crystal design, which is discussed. With this cavity, over 30 W of CW and pulsed vortex output power were achieved, representing a record vortex laser output. The generation of first order Hermite Gaussian modes is investigated and the results reported. A purity analysis of the vortex output is performed and the experimental control of the VOC is compared to theory. These results contributed to a published work [75].

5.1 Motivation

"Increasing the power" feels like it would be the natural next step in a lot of laser development, even if just to test the limits of what is possible. However, thinking beyond the childish glee of bigger numbers, more power brings potential commercial benefits. For material processing, where pulse energy is the a factor, a higher average power allows for a higher repetition rate and therefore higher processing speeds. For trapping and levitation, larger objects can potentially be trapped or a single source can be split and used to power an array of traps. For free-space communication or metrology over longer distances, through potentially turbulent or scattering media, more power can be useful.

5.2 Endcapped crystal for power scaling

To reduce the thermal stress in the gain medium a new Nd:YVO$_4$ crystal was tested. The new gain medium was 3x3x20 mm 0.3 at. % doping with fused 3x3x2.5 mm undoped YVO$_4$ end-caps. This gain medium was implemented in the L-shaped cavity shown in fig. 5.1a. It was end-pumped through a dichroic turning mirror by the same 808 nm diode laser used previously and was focused onto the near, doped face of the crystal. The pump focusing lens was also changed and replaced with a longer focal length, f = 250 mm, lens. This corresponded to an increased pump spot size of w_p=375 µm. A 1% at 1064 nm OC was employed as a BM. The cavity was initially built using two flat end mirrors, with the cavity arm containing the VOC made shorter than intended. The VOC was then aligned to the leakage out of this end mirror, before this flat mirror was removed. The OC was positioned 105 mm from the focus of the pump, while M2 in the VOC was position 110 mm from the pump focus on the other side. The VOC was again operated at 20% transmission, which was determined experimentally by measuring the intracavity power from the known transmission of the BM.

With 29.6 W of absorbed pump power the VOC had a CW output of 14.3 W, shown in fig. 5.1b. The same cavity had a threshold of 4.0 W, and a slope efficiency of approximately 55%. The vortex output at maximum pumping, shown in fig. 5.1c, had an excellent beam quality with an M^2 = 2.04. This is a step in demonstrating the power handling capabilities of the VOC and shows that the VOC is only limited by the underlying cavity. The results are limited to 29.6 W of pumping due to reduced mode quality at higher power, believed to be caused by aberrations in the thermal lens. This is a normal problem faced by solid state laser cavities when power scaling, and is tackled by taking measures to reduce the induced thermal lens in the crystal and redesigning the cavity to optimise the overlap between the intracavity and pump modes.
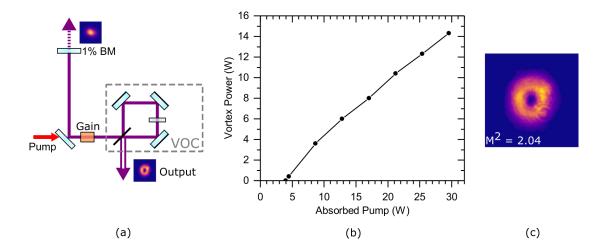
Figure 5.1: (a) L-shaped cavity composed of 1% OC as BM, dichroic turning mirror through which the Nd:YVO$_4$ crystal (Gain) is pumped and the VOC. The VOC is composed of three turning mirrors, a beamsplitter and an AR plate, highlighted by the grey-dashed box. (b) Plot showing output power scaling of the vortex laser output against absorbed pump power. (c) Spatial intensity distribution of 14.3 W vortex.

5.3   880 nm laser diode pumping for further power scaling

The vortex laser cavity schematic employed for this work is shown in fig. 5.2. It was based on a diode-end-pumped Nd:YVO$_4$ laser operating with linear polarisation on the crystal c-axis at 1064 nm. The Nd:YVO$_4$ crystal used was the same undoped endcapped crystal used in the previous section. The crystal was housed in a water-cooled copper mount and diode-end-pumped through a dichroic turning mirror (TM). The diode pump was a 65 W fibre-delivered module operating at 878.6 nm. By pumping at the 880 nm transition, rather than at 808 nm as in previous work [41, 43], the quantum defect heating is reduced, which when coupled with lower crystal doping and the use of endcaps reduces heat loading energy density and end bulging effects. This pump-crystal combination significantly lowers the thermally induced lensing to maintain high spatial quality and reduced crystal stress [76, 77, 78] that can lead to crystal fracture. As a result, the crystal was able to withstand the full power of the high-power diode pump module without damage and was ideally suited to investigate power-scaling of the vortex laser.

The laser cavity was formed between a plane back mirror (BM) and the modified Sagnac

interferometer acting as a vortex output coupler (VOC), highlighted by dashed grey box in Fig. 5.2. An intermediate 45° dichroic plane turning mirror (TM) was used with high reflectivity at the laser wavelength (1064 nm) and high transmission at the pump wavelength (878.6 nm) to allow ease of access for pumping the crystal and resulted in an L-shaped cavity with a total cavity length of 260 mm. The fibre-delivered pump beam was imaged to a near top-hat distribution in the crystal with a radius of 420 µm. A plano-concave lens (L) with focal length f=−500 mm in front of the back mirror was used for cavity mode size control. An acousto-optic modulator (AOM) placed between gain medium and back mirror provided Q-switching. The VOC was composed of a 50% beamsplitter (BS), 3 high reflectivity mirrors (M1-M3) and an AR-coated plane parallel fused silica plate for vertical beam displacement inside the Sagnac ring.
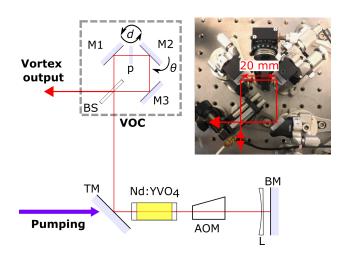
Figure 5.2: Vortex laser cavity composed of: Nd:YVO$_4$ crystal with undoped end-caps; high-reflectance back mirror (BM); intracavity lens (L) with f=−500 mm (l), 45° dichroic turning mirror (TM); VOC (highlighted in the grey-dashed box); and acousto-optic modulator (AOM) for Q-switching. The VOC is comprised of a 50% beamsplitter (BS), three HR mirrors (M1-M3) and a plane-parallel AR coated fused silica plate (P). Photograph of VOC system shown as inset.

The internal components of the VOC had their alignments adjusted to transform the fundamental Gaussian intracavity mode to produce a vortex LG$_{01}$ output mode and later re-adjusted to produce a HG$_{10}$ laser output mode. The transmission of the VOC was determined experimentally by comparing the power outputs from the VOC and the back mirror, which had a known transmission of 0.73% for cavity monitoring purposes.

5.4 30 W vortex laser using the VOC

The laser cavity in fig. 5.2 was first operated to output a LG_{01} mode from the VOC. The laser was operated in both CW and pulsed modes. In this section we show the power and pulse characteristics, along with analysis of the vortex mode purity and the ability to tune the VOC transmittance.

5.4.1 CW and pulsed results

The average output power of the vortex laser versus absorbed pump power is shown in fig. 5.3 for both Q-switched (pulsed) vortex operation at 150 kHz pulse rate (black data) and under continuous-wave (CW) operation with AOM not operated (red data). In pulsed operation, at the maximum available 62.5 W absorbed pump power 31.3 W of average vortex output power was achieved. To the best of our knowledge, this is the highest vortex power produced directly from a laser in a scalar OAM mode. The vortex laser had an impressively high slope efficiency of 62.5% and a threshold power of 13 W with the VOC at 28% transmittance. The output power under CW operation had a similar behaviour to the pulsed case. The spatial intensity profile of the vortex output is inset in fig. 5.3 for Q-switched operation at 150 kHzz.
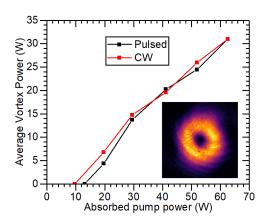
Figure 5.3: Average output vortex laser power versus absorbed pump power in pulsed operation at 150 kHzz Q-switching rate (black) and in continuous wave (CW) operation (red). The intensity profile of the vortex mode of the laser is shown in the inset.

The variation of vortex output power with Q-switching pulse rate is shown in fig. 5.4 at the maximum absorbed pump power of 62.5 W. Stable pulsing was achieved up to 600 kHz. At

100 kHz the pulse energy was 303 µJ and the pulse duration was 20 ns, corresponding to a peak power of 15.0 kW. Over the range of pulse rates presented the average output power stayed relatively constant and over 30 W.
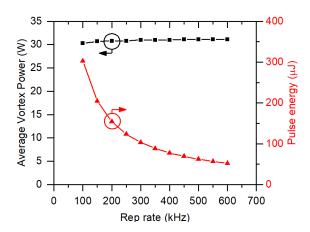
Figure 5.4:   Average output vortex laser power versus the Q-switching repetition rate, shown in black on the left hand axis. Pulse energy versus the Q-switching repetition rate, shown in red on the right hand axis.

5.4.2   Mode purity analysis

The M^2 beam propagation parameter can give a good indication of the modal content of a laser. The output vortex mode of the laser had the appearance of a high quality axially uniform annular LG_{01} mode, see inset Fig. 5.3, and it had a propagation beam parameter M^2 = 2.25, which is close to the theoretical LG_{01} value of $M^2 = 2.0$. This suggests that the VOC is working as intended at high power and is further supported as the intracavity mode had M^2 = 1.20, close to the diffraction limit of $M^2 = 1$ for a Gaussian beam as required in the VOC theory.

The M^2 parameter together with the high-quality annular appearance of the beam is a good but not conclusive proof of a vortex mode; however, importantly, it does not quantify the spiral phase required for a pure LG_{01} mode. To do so the phase must be measured, which when coupled with the intensity profile allows the mode content of the beam to be determined. This analysis was performed by interfering the vortex mode with a plane wave reference in a Mach-Zehnder interferometer. The resulting interferogram was then analysed with a phase retrieval algorithm based on that of Takeda et. al. [34] to recover both the phase and intensity profile

of the beam and perform the mode decomposition.

The phase retrieval process is shown in the fig. 5.5 insets. The first image shows the starting interferogram, which reveals the phase singularity from the central forked fringe. This interferogram is processed to retrieve the intensity and phase profiles of the laser output, see second and third insets. In the phase profile we see the helical structure with a phase singularity at the centre. From the phase and intensity profiles the mode decomposition is performed. To verify the accuracy of the mode decomposition, the input beam is reconstructed using the calculated mode weights and phases. The reconstructed intensity is an excellent match to the recovered intensity, concluding that the decomposition is accurate.

The mode decomposition results are shown in fig. 5.5, which shows the mode power content for LG_{pl} modes up to a total mode order of $2p + |l| = 7$. The beam demonstrates an excellent mode purity with 95.2% of the power in the $LG_{0,-1}$ mode. The next most significant mode was the small 0.8% contribution from the $LG_{1,1}$ mode. This could indicate a minor $LG_{0,2}$ impurity in the intracavity beam created by the VOC to the reflected beam, see eq. 3.5, which when returned to the VOC is converted to $LG_{1,1}$ from higher order conversion processes [35]. On repeated measurement the $LG_{0,-1}$ and $LG_{1,1}$ (labelled on figure) components remained at their relative strengths, with the contributions of the other higher order modes randomly varying due to noise in the interferogram diagnostic signal.

5.4.3 VOC transmission control

A useful feature of the VOC is the ability to adjust the output coupling transmission simply by changing the amount of vertical shear d_y and angular misalignment θ_x in the Sagnac ring. In this section we explore this behaviour and test the experimental performance compared to the theoretical transmission predicted by eq. 3.4.

The displacement and angular misalignment parameters (d_y, θ_x) were quantifiable in our laser system with the rotation of plate (P) and electronically piezo-controlled rotation of mirror M2. A 4-f image relay of the intracavity laser mode on mirror M2 allowed measurement of mode waist radius w so the divergence θ_0 of the intracavity beam could be calculated and therefore $\epsilon_y = d_y/w$ and $\epsilon_x = \theta_x/\theta_0$. The VOC theoretical transmission is then given by eq. 3.6. For LG01 output the canonical condition $\epsilon_x = \epsilon_y$ is expected to be satisfied.
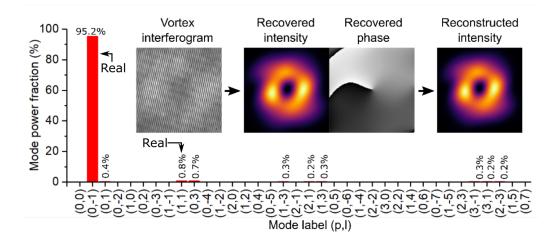
Figure 5.5:   Modal decomposition of the Q-switched vortex mode using a phase retrieval algorithm on a fork interference pattern, where modal power values greater than 0.1%, have been noted.   Inset: The fork interferogram, the recovered intensity and phase structure of the vortex from the interferogram, and the signal beam reconstructed from the decomposition algorithm.

The angle θ_x was adjusted with the piezo-controlled mirror M2, which rotates the mirror by $\theta_x/2$, whilst maintaining the canonical condition by adjusting d_y with the AR plate (P). The VOC transmission was measured by comparing the vortex output power to the leakage power from the back mirror (BM) that had a known transmission of 0.73%. The resulting transmissions of the VOC are shown in fig. 5.6(a) with red squares. The solid black line is a fit of the theoretical transmission function, eq. 3.6, to this dataset with w (beam radius) as a free parameter. While the fit showed excellent correlation with the data, the fitting parameter w_0 was larger than the actual w_0. This discrepancy is likely due to imperfect intracavity beam quality $M^2 = 1.2$ compared to the perfect fundamental mode used in the theory. As a further check, the observed versus predicted transmission based on the measured waist radius at each point is shown in fig. 5.6(b). A linear fit shows that the predicted and observed transmissions are linearly correlated. The linear fit has a slope of 1.2, which further suggests that the imperfect intracavity mode quality is causing an underestimation of the transmission predicted by theory.

5.4.4   Discussion

These results show the VOC's potential for high power, high repetition rate vortex pulses for industrial-scale applications such as material processing. The laser performance is only limited by the underlying cavity, the VOC could be used to adapt existing high energy, high repetition
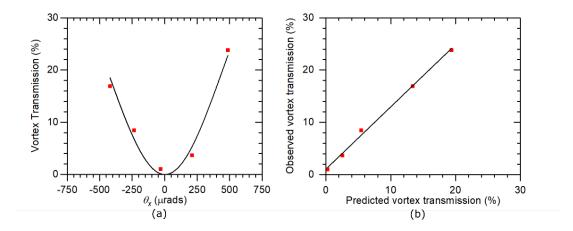
Figure 5.6:   (a) Experimentally observed transmission of the VOC in a vortex configuration (red squares), with eq. 3.4 fitted to the data (solid black line) with waist radius as a free parameter. (b) The observed transmission against predicted transmission using the measured waist radius (red squares), a linear fit is also shown (solid black line).

rate material processing lasers. We believe this provides a quick route to commercial material processing vortex applications, by circumventing further research into complex, novel cavity designs built around lossy or low power handling components.

When conducting any power scaling, consideration needs to be made regarding the laser induced damage thresholds of the optical components in the cavity and the energy fluence that they will be subjected to. In the VOC, the cavity mode will come to a focus on mirror M2, which means that this mirror will see the highest fluence of all the optics in the VOC. To reduce this fluence, the cavity could be designed to favour a larger spot size on mirror M2. A larger spot size, however, would reduce the divergence of the beam away from the beam waist, meaning the required angular misalignment θ would also be less. Greater experimental precision in the angular control of mirror M2 would then be needed to meet the canonical condition $\theta/\theta_0 = d/w_0$.

The high mode quality demonstrated separates the VOC method from other high-power capable vortex generation techniques. This makes the VOC a unique option in the structured light toolkit. Even greater mode quality is expected with a more ideal fundamental Gaussian intracavity mode.

The variable transmission of the VOC also offers another degree of freedom with which to optimise the underlying cavity power performance. The controllable misalignment that allows

variable transmission also enables the VOC to adapt to any mode size within the cavity. This means that the VOC can be added to any cavity that currently operates with a plane output coupler without requiring any cavity redesign. The small footprint of our implementation also demonstrates this potential.

The combination of high power and high mode purity makes the VOC a unique tool for vortex generation. With the extra features of handedness control, variable transmission and the possibility of being built with wavelength independent optics, we believe the VOC will help drive the structured light research and industrial implementation.

5.5   Hermite-Gaussian mode laser

The VOC laser in 5.2 is also capable of transmitting an HG type mode, as shown Chapter 3. To generate an HG10 or HG01 mode either the angle or displacement adjustments are implemented, ϵ_x or ϵ_y, instead of simultaneously for LG_{01} generation, see eq. 3.3a. This is an interesting use of the Sagnac VOC design to generate high power HG modes. One can convert HG modes into LG modes using astigmatic mode conversion; however, prior work generating HG modes with this approach have been limited to 100s mW [23, 24].

The VOC was operated in the laser system outlined in fig. 5.2 with only angular misalignment θ_x applied ($d_y = 0$). The laser output power is plotted against absorbed pump power in fig. 5.7(a), which shows over $30\,\mathrm{W}$ power in the HG_{10} mode. The laser slope efficiency was 60% and the mode intensity profile is inset. These results are almost identical to the vortex output configuration (see fig. 5.3) and demonstrate that the VOC can be switched between a vortex or HG_{10} output mode without loss in power or laser efficiency.

Fig. 5.7(b) shows the cross section of the experimental output mode overlaid with a theoretical plot of a HG10 mode. The HG_{10} mode had beam propagation parameters of $M_{x,y}^2 = 3.24/1.27$, which closely match the theoretical values of $M_{x,y}^2 = 3.0/1.0$ expected of the HG_{10} mode. This measurement along with the close fit to theory demonstrates the excellent mode quality produced by the mode transforming laser cavity.

To further characterise the HG_{10} laser output modal decomposition was also performed, similarly to the vortex case with an interference pattern and phase retrieval algorithm. This

showed that 91.4% of the power was in the desired HG10 mode. Some of the imperfection in this output mode was due to imperfect diagnostic optics and an imperfect intracavity fundamental mode quality.
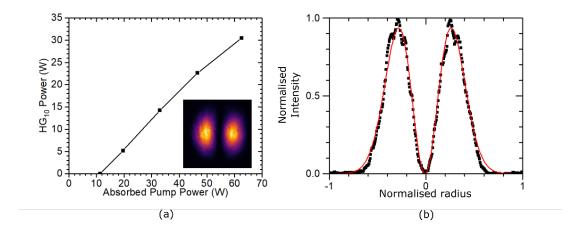
Figure 5.7: (a) Graph showing output power against the absorbed output power (intensity profile inset). (b) Intensity cross-section of laser output mode at maximum power (black) overlaid with the theoretical plot of HG_{10} mode (red).

5.5.1 HG mode transmission control

The transmission of the VOC in the HG mode configuration was also investigated. This was conducted in the same manner as previously with the vortex; however, the vertical shear was kept at zero ($d_y = 0$). The piezo control of VOC mirror M2 was used to systematically vary θ_x. The output powers from both the VOC and the BM were used to determine the transmission at each setting and the spatial profile of the beam at M2 was recorded.

The observed transmission values versus θ_x, the relative angle imparted on beam by M2, are shown in fig. 5.8(a) (red squares). The solid black line shows the fit of eq. 3.6 to these points with $\epsilon_y = 0$ and w_0 as a free parameter. This fit matches the observed values very well and the fitting parameter w_0 was close to the observed values of the beam waist. fig. 5.8(b) shows the observed transmission to the predicted value based on measured misalignment and the actual measured beam waist radius w_0 at M2 via eq. 3.6. A linear fit with slope of 1.0, shows an excellent correlation between predicted and observed transmission values.

With such excellent first-order HG mode quality and the potential to power scale far beyond the 30 W output power demonstrated here, we believe that this is a powerful use case for the
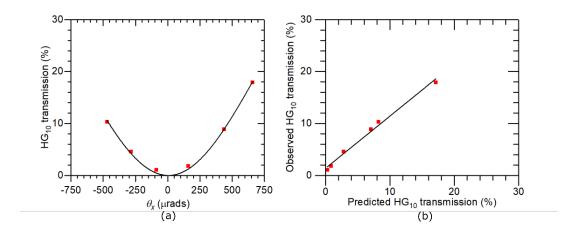
Figure 5.8:   (a) The experimentally observed transmission of the VOC in an HG_{10} configuration (red squares), with eq. 3.4 fitted to the data (solid black line). (b) The observed HG_{10} transmission against the predicted transmission (red squares) using the measured waist radius, a linear fit is also shown (solid black line).

VOC. The high-power, and high quality, HG mode demonstrated here could be used in vortex generation using astigmatic mode conversion [23, 24].

5.6   Chapter summary

This chapter presented a new crystal design and pump scheme as methods for power scaling the underlying cavity, with the aim of achieving increased vortex output power.

The results in this chapter demonstrate a Q-switched vortex laser with, to the best of our knowledge at the time of writing, a record vortex power of 31.3 W produced directly from a laser. The LG_{01} vortex mode was measured to have a high modal purity of 95.2% using a phase retrieval algorithm. The laser operated with an exceptionally high slope efficiency of 62.5% and had Q-switched operation up to a high pulse rate of 600 kHz. Using a simple adaptation of the output coupler configuration, we have also demonstrated the transformation of the internal cavity mode to a HG_{10} mode with >30 W power, which matched well to a theoretical HG10 mode profile and had a 91.4% modal purity. We performed an investigation of systematically varying the VOC transmission in both vortex LG_{01} and HG_{10} mode laser configurations and compared the results to the theoretical VOC model.

Chapter 6

Fibre vortex laser

In this chapter the vortex output coupler (VOC) is integrated with fibre systems to create fibre vortex lasers. This work aims to prove the versatility of the VOC as well as harness the advantages of fibre systems. An overview of fibre vortex lasers in literature is presented, with an introduction to fibre laser systems. A progressive set of experiments, integrating the VOC with fibre systems and increasing the power levels, are presented.

The first experimental integration of the VOC with a fibre system consisted of a length of passive, single-mode fibre, a fundamental Gaussian source and the VOC. The ability of the VOC to convert light coupled out of a fibre was investigated, as well as its ability to recouple light back into the fibre.

The next step was to implement the VOC as the primary output coupler of a Ytterbium-doped fibre laser oscillator. A method to align the VOC to a fibre laser oscillator is presented and stable lasing is demonstrated. Importantly, the polarisation independence of vortex generation using the VOC is investigated, showing that the VOC can operate with a non-polarisation maintaining fibre.

The final cavity presented uses an Ytterbium-doped active fibre, pumped with a fibre coupled laser diode. Over 5 W of vortex output power is achieved using the VOC as an output coupler. The mode purity across the entire power range is analysed and showed to be in excess of >95%. The results in this chapter are currently being written up for publication.

6.1   Motivation

While the basic principal of total internal reflection was known in the 19th century, the first fibre laser wasn't demonstrated until 1960 [79, 80], about a year after the first demonstration of the laser [81]. Since these seminal works immense strides have been made in fibre production methods, accessible wavelengths and achievable powers.

Fibre systems provide some advantages over free-space systems. Many free space laser optics have analogous fibre components, which can be spliced together to create an alignment free system. This can also make them very robust to the environment, as the fibre can be moved and coiled while still maintaining its wave-guiding properties. Because it can be coiled, fibre systems can be made very compact. Furthermore, due to generally low doping levels and long fibres, there is less risk of thermally induced lensing changing the stability of the cavity. Lastly, and importantly for the work with the VOC, single mode fibre can be implemented to ensure a fundamental Gaussian mode. This makes a fibre based gain system a promising route to a power scaled vortex laser using the VOC.

6.2   Vortex generation using fibre systems

The main fibre vortex generation method is mode superposition. There are two steps to this method: generating higher order LP modes (Fig. 6.1) and introducing a $\pi/2$ phase shift between its constituent vector modes to generate a vortex. This is analogous to free space methods using cylindrical lenses or curved mirrors to adjust the phasing between HG modes. The phase control is achieved by applying stress to the fibre carrying the higher order mode (HOM), however there have been different approaches to generating the HOM. One approach is off-axis coupling of the fundamental mode into a few mode fibre (FMF) or two mode fibre (TMF) as shown in Fig. 6.2a [82]. Using the experimental set-up shown in fig. 6.2b an 8.5 W picosecond output was achieved with 12.5 kW of peak power. The achieved mode was diagnosed to have a helical phase, however visual inspection of the presented mode suggests that the phase singularity does not go to zero and the intensity profile is not uniform. Off-axis coupling to generate the HOM has also been achieved by core-shifting the the splice of a single mode fibre (SMF) to a FMF [83]. Another method for generating the HOMs needed for the vortex generation is using an
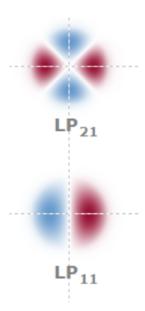
Figure 6.1: First and second order LP modes used for first and second order vortex generation in fibres. [Image taken from RP Photonics web page]

SMF-FMF coupler. With the correct phase matching criteria met between the LP_{01} mode in the SMF and the desired mode in the FMF, light can be coupled between the fibre to achieve the desired mode as shown in fig. 6.3 [84].

6.3 Coupling the VOC with a passive fibre

The first consideration when integrating free-space optics with a fibre system is whether coupling in and out of the fibre is viable. The light coming out of the fibre must be exactly reimaged to achieve the recoupling necessary for lasing. The experimental set-up, shown in fig. 6.4, was therefore built to test the VOCs ability to use light coupled out of a fibre and then recouple light back into the fibre. A single mode source, at 1064 nm, was used and passed through an optical isolator to protect it from any reflections. Two HR mirrors were employed to help align the beam to couple into the fibre. The beam was coupled into a length of undoped, single-mode fibre using a 4.5 mm aspheric lens. A 50% output coupler, at 0°, was added at a small angle to pick off any power coming back out of this fibre end. The light was then coupled out of the fibre at the other end using an 8 mm aspheric lens, which was positioned to reimage the fibre tip 285 mm away from the lens. This was chosen to allow enough space to implement the VOC and any polarisation altering elements that may be required. The VOC, consisting of an unpolarised beamsplitter (50:50 at 45°) and three HR turning mirrors, was added into

(a)　　　　　　　　　　　　　　　　　　　　(b)
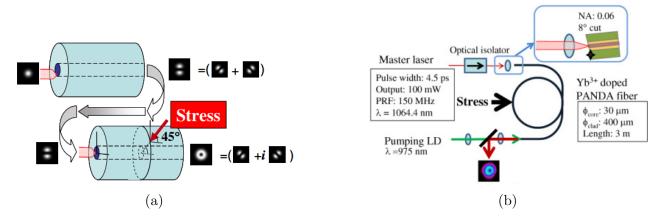
Figure 6.2: (a) Figure showing off-axis coupling of the fundamental mode into the fibre to excite the LP11 mode and then stress is applied to create the vortex. Inset intensity profiles show: (top) the decomposition of the LP_{11} mode into two TEM_{01} modes at 45°, (bottom) generation of the vortex via the superposition of the two TEM_{01} modes with the correct phase shift. (b) Figure showing experimental set-up used in Tanaka et al.[82]
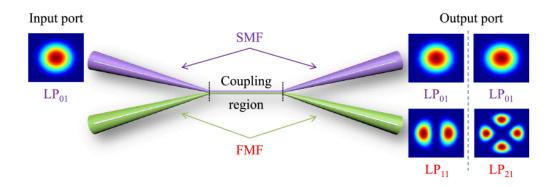
Figure 6.3: Figure from Zhang et al. demonstrating input mode on the left being coupled from a single mode fibre (SMF) into a few mode fibre (FMF) to generate higher order modes.[84]

the beam path such that the reimaged plane of the fibre tip was situated on the mirror M2, as shown in fig. 6.4. Both ends of the fibre were angle cleaved (8°) to avoid Fresnel reflections being guided by the fibre and creating a standing wave in the fibre.

To provide a baseline, a HR mirror at normal incidence was positioned at the reimaged plane of the fibre tip, before the VOC was built. The HR was aligned to optimise the recoupling back through the fibre, and a 98% recoupling efficiency was measured. The HR mirror was then replaced with the VOC, which was aligned for zero transmission, essentially acting as a retro-reflector. In this configuration 95% power recoupling was achieved, which was satisfactory as small losses from the AR face of the beamsplitter and non-ideal reflection of the turning mirrors for randomly polarised light could account for the small drop in recoupling.

The VOC was then aligned for vortex transmission, shown in fig. 6.5. An excellent beam
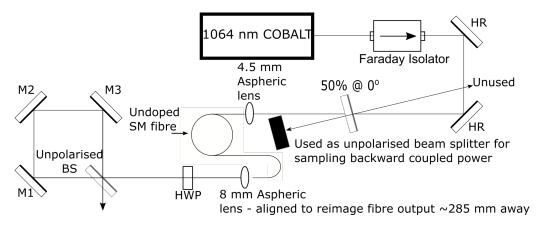
Figure 6.4: Diagram of experimental set up used to verify VOCs ability to use light coupled out of a fibre and recouple light back into the fibre. A 1064 nm single mode CW source was used and was coupled through an isolator to protect it from any reflected beams. Two HR mirrors and a 4.5 mm aspheric lens were used to couple the light into a single mode fibre. A 50% output coupler (at 0°) at a small angle was added to the beam path to measure any light leaving the fibre. The light was then coupled out of the fibre using an 8 mm aspheric len, which was positioned to reimage the fibre tip 285 mm further on. The VOC was arranged so that the reimaged plane was on mirror M2. A half-wave plate (HWP) was added to the beam path also.

propagation factor, $M^2_{X/Y} = 2.16/2.26$, was measured, which is very close to the theoretical value of 2. For this result the VOC was configured for 12% transmission and a recoupling of 84% was achieved, while maintaining the vortex transmission. These results showed promise that the VOC could be integrated with a fibre gain system to create a fibre vortex laser.
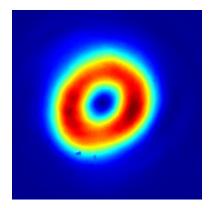
Figure 6.5: Snapshot of the spatial intensity profile of the vortex generated by the VOC while recoupling the reflected light back into the fibre.

6.4 Low power vortex fibre laser using the VOC

To determine the practical feasibility of integrating the VOC with a fibre gain medium, to create a stable laser, a low power fibre system was set up. The experimental set up used is shown in fig. 6.6. A non-polarisation maintaining (PM) ytterbium (Yb) doped gain block,

from IPG Laser GmbH, was used as a gain medium. The block had an input port, two output ports and a monitoring port. An IPG pump diode, with a central wavelength of 965 nm, was spliced onto the input port of the gain block. The monitor port picks off 1% of the intracavity flux and was angle cleaved, to reduce any feedback. One output port has a fibre bragg grating (FBG) spliced onto it. The FBG acts as a back mirror to the cavity with reflection of 87% at 1063.91 nm and a bandwidth of 0.15 nm. The fibre after the FBG has also been angle cleaved to reduce feedback into the cavity. The final output port has been flat cleaved, which provides 4% reflection due to Fresnel reflections. The pump diode and gain block were already spliced together from a previous project and, unfortunately, there was no data on the pump power against driving current. However, for the purposes of validating the VOCs functionality in a fibre laser system, it was enough to compare the relative performance of the VOC against a plane output coupler.
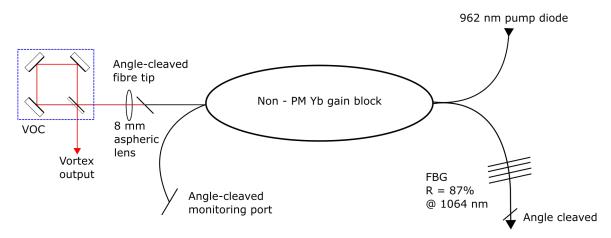
Figure 6.6:   Diagram of experimental set-up for low power fibre vortex laser. An Ytterbium doped, non-polarisation maintaining gain fibre was pumped using a fibre delivered laser diode, lasing at 965 nm. One end of the gain fibre was spliced onto a fibre Bragg grating (FBG), which had a reflectivity of 87% at 1064 nm. The fibre after the FBG was angle cleaved. The output of the fibre was angle cleaved (8°) and reimaged, using an 8 mm aspheric lens, to a point 235 mm from the lens. The VOC was aligned so that the reimaging plane was on mirror M2. There was also a monitoring port, which remained unused and was angle cleaved and taped to the lab bench surface.

The output power of just the fibre system, with the flat cleave acting as the output coupler, was then plotted against input current. A maximum output power of 48 mW was achieved with 2.2 A of pump current, with a threshold of 1.7 A, corresponding to a slope efficiency of 96 mW A^{-1}. This was carried out to set a benchmark output power value with low feedback

output coupling, typical of most fibre cavities.

The next step was to test how the cavity would respond to increased feedback and coupling out and back into the fibre itself. To achieve this the flat cleaved fibre end was angle cleaved and an 8 mm aspheric lens was used to re-image the end of the fibre to a point 235 mm from the lens. An HR mirror and a 30% transmission mirror (for 1064 nm @ 0°) were tested as output couplers, which were placed at this focal plane to exactly re-image the fibre mode back into the fibre. These two mirrors were chosen to represent the VOC at minimum and maximum transmission values, to test the damage potential if the VOC were aligned for reflection and to provide a reference to judge the performance of the VOC during operation. Each mirror was aligned using the amplified stimulated emission (ASE), while the pumping was below the laser threshold. This was to protect the fibre from sudden spikes in intracavity flux when the alignment was found, or from burning the fibre cladding when recoupling. Alignment of the mirrors was determined by monitoring the ASE power from the FBG, which increased by 50% at optimal alignment. The pump current was then slowly turned up until lasing was achieved, before further turning up the pump diode power, monitoring for any signs of failure along the way.

No failure was observed in this maximum feedback set up, however the pump current was only increased up to 1.9 A as a precaution. The threshold was significantly decreased to 0.74 A and 0.82 A with a maximum power of 33.1 mW (out of the FBG port) and 39.1 mW (out of the , using the HR and 30% transmissive mirrors respectively. The slope efficiencies were 28.8 mW A^{-1} and 37.0 mW A^{-1}. This shows that the laser efficiencies are greatly reduced when employing reduced output coupling. However, these results also showed that the system would not fail due to excess feedback in the system, when the VOC was implemented.

6.4.1 Low power VOC implementation

Much like when aligning the HR mirror to create the high feedback cavity, the ASE from the fibre was used to align the VOC on the end of the fibre cavity. The beamsplitter was polarisation independent. This allowed the use of a non-polarisation maintaining fibre and avoided, potentially lossy, polarisation components intracavity. The BS was angled for 50:50 power splitting, which was verified to be polarisation independent by inserting a cube polariser

on a rotation mount between the fibre end and the BS. The cube polariser was then removed
and the three turning mirrors (M1, M2 and M3) were inserted to complete the VOC. These
mirrors were aligned for zero transmission through the VOC. The reflection was then aligned
to co-propagate with the cavity beam and recouple into the fibre. This was achieved using the
help of an aperture, which helped with alignment and provided some protection against fibre
damage due to misalignment.

6.4.2   Low power vortex cavity results

The cavity was successfully operated and the results shown in fig. 6.7, when operating the
VOC with 36% output coupling. The output power of the VOC in the vortex mode, with 36%
output coupling, against the driving current of the pump module is shown with black squares.
The total output power of the cavity, from the VOC and the FBG, against the same driving
current is shown with red squares. The maximum power at 1.9 A of driving pump current
was 33.6 mW and the system had a slope efficiency of 28.8 mW. This was less power and less
efficient than whats was achieved with the 30% plane mirror output coupler.

The intensity profiles of the vortex mode are shown in Fig. 6.8. Left and right handedness
(Fig. 6.8) vortex generation was demonstrated and switching was achieved during lasing oper-
ation. They had beam propagation parameters of $M^2 = 2.11/2.24$ and $2.12/2.25$ respectively,
which is close to the theoretical value for an LG_{01} of 2.

While the beam propagation parameter is excellent, the intensity profiles of the modes are
not completely uniform. It was found that in this cavity set-up a stray reflection was interfering
with the generated vortex, which may have contributed to this. The source of the reflection
was found to be the front face of the angle-cleaved fibre output. This Fresnel reflection is
divergent from the cavity mode, due to the 8° angle-cleave, however the collimating lens was
acting to re-image it close enough to the main beam that it was interfering. The source of the
reflection was confirmed by the ability to mostly remove it by introducing a beam block between
the collimating lens and the fibre tip, which was carefully positioned to not interfere with the
main beam. While the stray beam was able to be mostly removed, there may still have been
enough, too close to the main beam to block out effectively, that distorted the output mode.
Interestingly, given that the fibre output has a bandwidth $\Delta\lambda = 0.125$ nm, a rough calculation
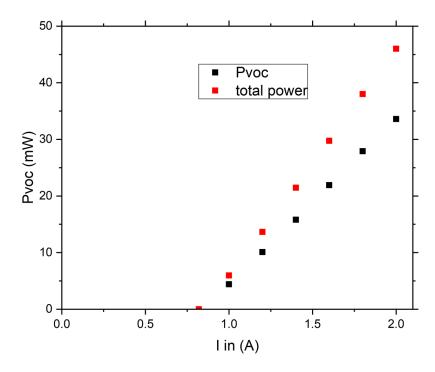
Figure 6.7: Graph of vortex output power (black squares) and total cavity output power(red squares), consisting of the vortex and fibre Bragg grating output power, against the pump input driving current.

of the beam coherence length suggests it should be on the order of 3 mm. This is many orders of magnitude less than the round trip length from the VOC to the fibre tip and back to the VOC, which implies that the reflected stray beam should be completely incoherent with the cavity beam.

To verify the polarisation independence of the experimental setup a quarter waveplate and a cube polariser were introduced. The quarter waveplate was introduced into the cavity, between the collimating lens and the VOC. The cube polariser, mounted on a rotation mount, was introduced at the output of the VOC to analyse the linear polarisation makeup of the output beam. The quarter waveplate was systematically rotated by 30°, from 0-90°, and the cube polariser was rotated though 360° for each quarter waveplate orientation. The power of the output beam was recorded, as well as the transmitted power through the cube polariser. The results are shown in fig. 6.9. The different quarter waveplate orientations are shown by different colours, indicated in the inset legend. In the top right of the figure the intensity profiles and powers of the vortex output are shown in order of quarter waveplate orientation. Overlaid on
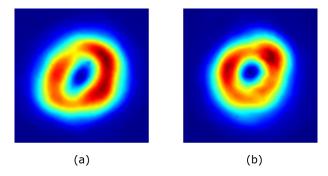
Figure 6.8: Snapshots of the vortex mode intensity profile with (a) right handedness and (b) left handedness.

the graph are snapshots of the mode intensity after the cube polariser at the minimum and maximum powers.

The introduction of the quarter waveplate does not seem to affect the intensity profile of the mode, which indicates that the beamsplitter in the VOC is truly polarisation independent. There is a very small power fluctuation (18.0 - 18.5 mW), however this may be explained by increased losses from the three turning mirrors, which are coated for HR for vertical polarisation only. When the quarter waveplate was aligned for 30° and 60° the output mode was overwhelmingly vertically polarised. Oriented at 0° the beam was the least vertically polarised and had the lowest output power, which corresponds to the increased leakage from the turning mirrors in the VOC that would be experienced. The smaller inset snapshots show that regardless of polarisation, the output mode stayed unchanged.

There is no inherent polarisation altering involved the vortex conversion process and the polarisation state of the vortex will be the same as that of the input beam. Experimentally, optical coatings may be optimised for a particular polarisation state (ie. vertically polarised light), which may have a filtering effect when used with a different polarisation state. Importantly, the beamsplitter needs to be coated for 50:50 splitting for the polarisation of the incident light. This is to ensure that the two counter-propagating beams are power balanced and the constructive/destructive interference occurs as intended.

6.5   Power scaled vortex fibre laser using the VOC

Following on from the successful integration of the VOC with an otherwise entirely fibre based laser, a system with higher output power capabilities was proposed. This would leverage the
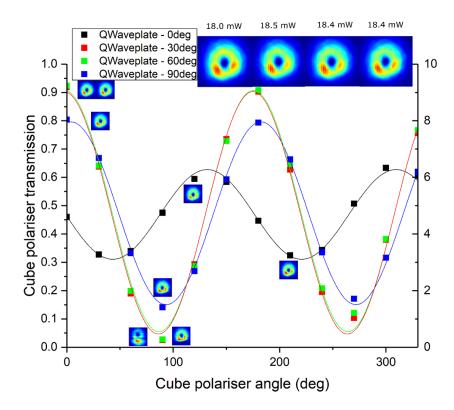
Figure 6.9: Graph showing the result of testing the polarisation sensitivity of the VOC set up. A quarter waveplate was inserted into the cavity, between the fibre tip and the VOC, and the output then passed through a cube polariser. The quarter waveplate was then systematically rotated by 30°, from 0-90°, and then cube polariser was rotated though 360° for each quarter waveplate orientation. The different quarter waveplate orientations are shown by different colours. Inset are snapshots of the intensity profiles of each beam before the cube polariser, with accompanying power, and snapshots after the cube polariser at the maximum and minimum transmission points.

unchanging mode quality and size across Watts, even 10s of Watts, of output power from the fibre. This unchanging mode size and quality should allow the VOC configuration to only need to be optimised once for the desired transmission and mode output, across the entire output power range.

6.5.1 Experimental set-up

The experimental system used is shown in fig. 6.10. A 60 W laser diode, locked at 976 nm, with fibre delivered multimode output was spliced onto a multimode pump combiner (MMPC). The MMPC had two input ports, allowing two pump diodes to be combined, and was capable of handling 100 W of combined pump power. However, only one pump diode was used in this experiment, the other port of the MMPC was angle cleaved and taped to the work bench. The
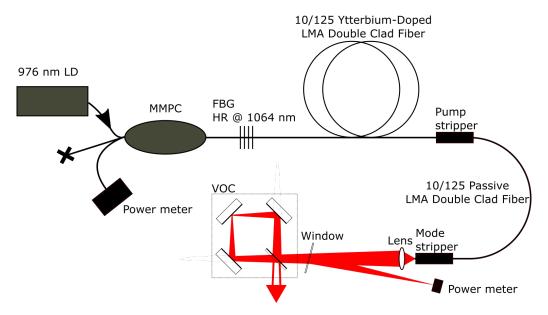
Figure 6.10: System diagram showing fibre vortex laser set-up and pumping. Multi-mode pump diode output fibre delivered to a multi-mode pump combiner (MMPC). The second input port to the MMPC was unused and taped to the work surface. The MMPC was spliced onto a single mode fibre with an FBG etched into it, which was designed to be highly reflective at 1064 nm. The single mode firbe containing the FBG was spliced onto a large mode area (LMA) double-clad, Ytterbium-doped fibre. The doped fibre was spliced to a length of passive LMA fibre, with a pump light stripper separating the two. A second mode stripper was added to the end of the passive LMA fibre, which was mounted on a collimation stage. The fibre tip was angle cleaved (8°). A 8 mm spherical lens was used to focus the output of the fibre onto mirror M2 of the VOC. A plane-plane, AR coated window was used to monitor the power entering the VOC. A power meter was also placed at the fibre output of the FBG.

MMPC was spliced onto a fibre Bragg grating (FBG), which was etched onto a single mode fibre and was designed to be highly reflective at 1064 nm. The FBG was spliced onto a large mode area (LMA) double-clad, Ytterbium-doped fibre. A cladding light stripper, comprised of a section of fibre with the cladding removed and taped to an aluminium strip with graphite tape, was added at the end of the active fibre to remove unabsorbed pump light. A length of precision matched passive LMA fibre was spliced onto the end of the active fibre and another cladding light stripper was added to the other end, which was mounted on a translation stage. The fibre tip was angle cleaved (8°) to suppress unwanted lasing with this face. The output was re-imaged 260 mm away using a 8 mm spherical lens. The VOC (comprising of a beamsplitter and three turning mirrors) was set-up around this output beam, ensuring that the focal plane of the beam was on M2. The VOC was mounted on a translation stage, which moved parallel to the beams path of propagaton, and was carefully aligned to ensure maximum recoupling of

the reflected light back into the fibre. An aperture was placed just after the collimation lens, which helped to align the return beam while protecting the fibre tip from severe misalignment. A thin, AR coated, plane-plane window was added to measure the intracavity power going into the VOC. The mode stripper at the output of the fibre ensured only core coupled light was able to propagate back into the fibre.

After receiving the fibre system from the Imperial Femtosecond Optics Group, the fibre end was angle cleaved and the collimation lens introduced. The collimation lens was adjusted to reimage the fibre tip 260 mm away from the lens. This resulted in a spot with 190 µm diameter and a Rayleigh range $z_R = 26.5$ mm. After this was established, the VOC was added. An AR (at 0°) coated wedge plate was introduced at a slight angle in front of the power meter monitoring the vortex power. The small amount of picked off power was used to run diagnostics on the vortex output: determination of the beam's M^2 and the modal purity of the beam using an MZI.

A thermal camera was also set up to monitor the temperature of the mode stripper at the output face of the fibre. This was implemented as a precaution to alert to excessive heat deposition due to recoupling losses. Some recoupling losses were expected due experimental error causing the fibre output to not be perfectly reimaged onto the fibre tip and the small fraction of higher order modes in the return beam, due to the vortex transformation. Furthermore, fibre laser systems tend to be operated with very high output coupling ($\approx96\%$), making use of the inherent Fresnel reflections off the inside of a flat cleaved fibre to provide feedback, whereas the VOC is limited to $\approx30\%$ output coupling so as not to degrade the vortex quality too much. The experimental work was therefore approached cautiously and the system constantly monitored for signs of failure.

Double-clad fibre

Double-clad fibres consist of the following optical layers: core inner cladding, outer cladding (see fig. 6.11). In modern double-clad fibres for high power applications, the inner cladding has a higher refractive index than the outer cladding and the core has a higher refractive index than the inner cladding. This allows the inner cladding to guide light by total internal reflection in the same way the core does, but for a different range of wavelengths. This means that high

power, multi-mode diode lasers can be used as pump sources. The pump light propagates along the inner cladding, frequently interacting with the core. The doped core gradually absorbs the pump light, driving the amplification process, and the generated signal then propagates in the core.
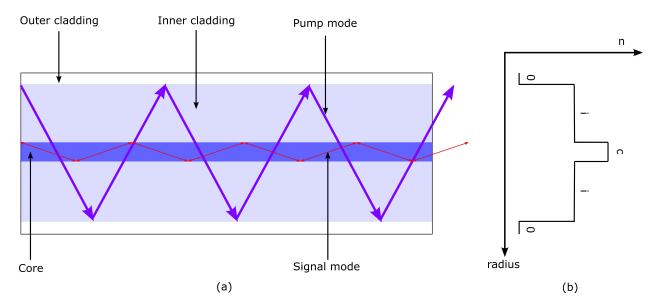
Figure 6.11:   (a) a schematic of a double-clad fibre, including: the core, the inner cladding, the outer cladding, the total internal reflection of the pump light and the total internal reflection of the core light. (b) Axis of refractive index (n) against fibre radius, with the relative refractive indices of the core (c), inner cladding (i) and outer cladding (o) across the radius shown.

This pumping scheme is commonly referred to as cladding pumping and was first introduced in 1989 [85]. Double-clad fibres have been used to produce continuous wave power into the kilowatts, while maintaining a near diffraction-limited beam quality [86].

6.5.2   Testing the system with an external output coupler

Before adding the VOC, plane output couplers with differing, quantified, transmission values were used to reimage the fibre output and complete the cavity. Output couplers with transmission values of 96%, 70% and 30% were tested. These were all carried out successively, at low power, from highest transmission to lowest transmission, in order to test the system's response to increased feedback. In each case the input power from the pump diode was only increased to 6.80 W, to not over stress the system in these preliminary experiments.

At 6.80 W of pumping the original system, with the flat cleaved fibre tip, produced 4.66 W of 1064 nm, CW, near diffraction limited light. The power out of the end of the FBG was also

monitored and found to be 30.9 mW. Once the fibre tip was angle cleaved and the output collimated, the first output coupler used was an uncoated wedge plate. This was chosen as it would have the same Fresnel reflection as the flat cleaved fibre tip. At 6.80 W of input power this new system produced 4.05 W of output power and the power recorded at the FBG was 26 mW. The discrepancy in the two results may be explained by slightly different transmission values, however the lower power from the FBG may indicate a lower feedback which could also point towards small recoupling losses. This is also corroborated by looking at the thermal reading of the graphite tape of the mode stripper at the fibre output, which read 25.5 °C. This is above the maintained lab temperature of 21 °C, suggesting heat deposition into the mode stripper due to non-ideal recoupling into the fibre core.

The uncoated wedge plate was then swapped out for the output coupler with 70% transmission and the pump power again taken up to 6.80 W. With this output coupler the output power dropped to 3.87 W, the power from the FBG read 122 mW and the temperature of the mode stripper was 26 °C. Finally, the 30% transmission output coupler was introduced. The power out was 2.72 W, the FBG power loss was 395 mW and the temperature of the mode stripper was 31.8 °C. As expected the laser functioned less efficiently with increased feedback, and increased heating of the mode stripper was observed, which limits the power scaling capabilities of the current system. However, these preliminary tests showed that the system would function with the required high feedback and, importantly, the laser performed better (40% optical-to-optical efficiency) than just placing the 30% output coupler into the output beam. This demonstrates the validity of incorporating the VOC into a fibre system.

6.5.3 Fibre vortex laser results

The VOC was then incorporated, as previously shown in fig. 6.10. The alignment procedure was much the same as in the previous fibre systems. The pump power was started below the threshold power for the laser and the aperture was centred and closed around the ASE from the fibre, so that only a fraction of the power passed through. The VOC was then aligned for vortex transmission using the ASE leakage and the return beam was aligned to pass back through the centre of the aperture. The pump power was then systematically increased, scanning the return beam across the centre of the aperture at each step, until lasing was achieved. The aperture

was then fully opened and the VOC alignment optimised for output power and modal quality.

The VOC was operated at 30% and 25% output coupling, to provide some comparison between laser performance at varying transmissions and to compare the effect on vortex quality. A maximum pump power of 15.8 W was used to keep heating of the graphite taped mode stripper below 60 °C.
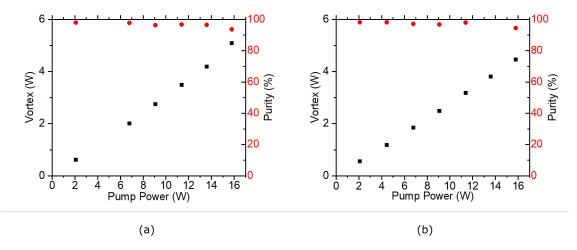
Figure 6.12: Graphs showing vortex power output (left y-axis, black squares) and vortex mode purity (right y-axis, red circles) against input pump power. (a) shows operation with 30% output coupling, while (b) shows operation with 25% output coupling. The red line shows the linear fit.

Fig. 6.12 shows the vortex output power of the VOC against pump power and the modal purity at each point, while operating at 30% and 25% output coupling respectively. At 30% output coupling a maximum power of 5.08 W was achieved, with a slope efficiency of 32.2%. At this point the mode had a beam propagation factor $M^2_{X/Y} = 2.03/2.22$, which matches the theoretical value of 2 well. The mode purity, determined using the same modal decomposition technique used in previous sections, started very high at 97.8% but reduced slightly to 93.6% as the power increased. This was unexpected as the internal mode should remain unchanged in a fibre system.

Looking at the mode profiles at the focal plane of the beam, shown in fig. 6.13, they seem to be stretching diagonally as the power is increased. This was again unexpected as the internal mode should remain unchanged and, therefore, so should the vortex output. This can be explained if we assume a thermal lens is formed in the collimating lens as the power is increased. A shortening of the effective focal length of the collimating lens would move the

focus off mirror M2 in the VOC. As seen in previous chapters, when angular misalignment is introduced away for the focus plane some spatial misalignment is also introduced, which results in the stretched mode profile and reduced mode purity. The mode purity of 97.8% may therefore be maintained despite power scaling, if the distance between the fibre tip and the collimating lens were adjusted slightly to keep the focal plane on mirror M2. When the transmission

| 0.61 W | 2.01 W | 3.48 W | 5.08 W |
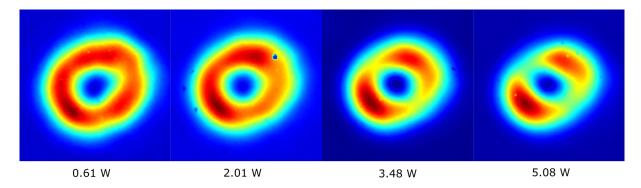
Figure 6.13: Snapshots of the intensity cross-sections of the vortex mode with increasing power at 30% output coupling.

of the VOC is reduced to 25% there is a drop in the peak power achieved, to 4.46 W, and slope efficiency, to 28.6%. This is expected as the previous results showed decreased power with increased feedback, indicating a decrease in the system efficiency. The modal purity was slightly higher (98.2%), than at 30% transmission, but also dropped with increasing power (94.4%). The spatial profiles of the vortex mode mirror the results at 30%, indicating that thermal lensing in the collimating lens may have caused issues here too.

6.5.4 Thermal lens correction

To verify the theory that a thermal lens, due to the intracavity flux, resulted in the vortex output becoming elliptical, the distance between the fibre tip and the collimating lens was optimised. Fig. 6.14 shows the corrected output at maximum power, with its fork interference pattern. The snapshot shows that the intensity profile is much more circular. A modal decomposition revealed that the mode purity was 96.1%, which is much closer to the mode purity at low power, indicating that the re-imaging of the fibre tip onto mirror M2 in the Sagnac does change with increasing power and can be compensated for.

The mirrors used in the VOC were the same used in the previous chapters in the vanadate cavities. They are HR coated for 45° and vertically polarised light. So operating in the fibre

(a)   (b)
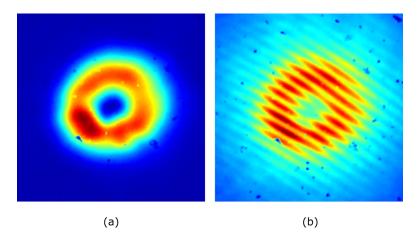
Figure 6.14: (a) Snapshot of the intensity cross-section of the vortex mode output at maximum power, after optimising the re-imaging of the fibre tip onto mirror M2. (b) Snapshot of the fork interference pattern resulting from the interference of the vortex mode with a quasi plane wave.

cavity, with light of a random polarisation, they were more lossy than one might expect of HR mirrors. While this may have reduced the output power of the VOC slightly, the losses may have actually improved cavity efficiency due to higher losses being preferential in the fibre cavity.

6.5.5   Fibre vortex system performance

While achieving the results laid out in the previous section, the rest of the experimental system was monitored. This was to better understand the system, but also to hopefully preempt any component failures. The parameters monitored were: power leakage from the FBG, power leakage through mirror M3 in the VOC and the temperature of the graphite tape of the mode stripper at the output of the fibre.

The power leakage from the FBG was monitored initially to confirm whether it acted similarly to the back mirror in a bulk cavity. This would allow the power leaking from the FBG, along with the known value for the FBG transmittance and the output power of the VOC, to calculate the transmission of the VOC. However, looking at the data taken, shown in fig. 6.15, the response to input pump power is non-linear. The leaked power from the FBG increases exponentially with increasing pump power. There are a few parameters that may influence this: the intracavity flux is increasing exponentially with pump power or the wavelength of the signal light is shifting away from the HR band of the FBG. Considering the intracavity flux
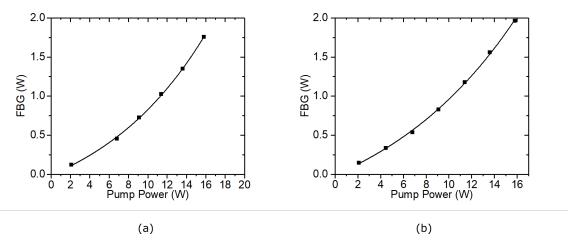
Figure 6.15: Graphs showing power output of the fibre Bragg grating (FBG) against input pump power. (a) and (b) show operation at 30% and 25% output coupling respectively. The red line shows an exponential fit to the data.

increasing exponentially, this could happen if the pumping wavelength shifted with power and there was increased absorption in the doped fibre. However, this would have presented itself in the data taken by the FOG group, before they handed over the system, as they also monitored the power coming out of the FBG and it remained linear with power. An exponential power increase in the output power would also be expected in this case. It therefore seems more likely that the wavelength is shifting away from the HR band of the FBG as the pump power increases, leading to increased losses from the FBG.

The power leakage from mirror M3 was also monitored. This was undertaken to understand how it changed with power scaling and evaluate its potential use in calibrating the transmission of the VOC. The results are shown in fig. 6.16. Both graphs show a linear response of the power leaking from mirror M3 against input power. This suggests that during laser operation the polarisation of the intracavity mode remains unchanged and that the intracavity flux scales linearly with input power. This suggests that in future builds, the power leakage from M3 could be used to verify to transmission of the VOC and that the currently implemented window could be removed. This would reduce the number of optics and losses in the system.

The final system check made was to monitor the temperature of the graphite tape on the mode stripper at the recoupling into the fibre, which is shown plotted against pump power in fig. 6.17. This was important as excessive heating could lead to the fibre jacket melting and destroying the fibre. The graphs show that the temperature of the graphite exponentially

(a)   (b)
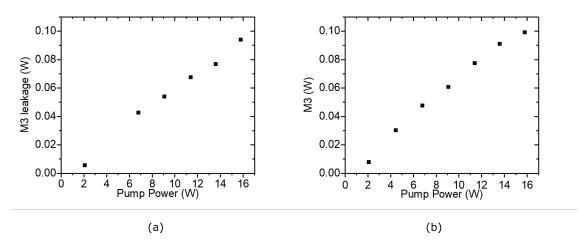
Figure 6.16: Graphs showing power leakage from mirror M3 in the VOC ring against pump input power. (a) and (b) show operation at 30% and 25% output coupling respectively. The red line shows a linear fit to the data.

increases with pump power, reaching 55.3 °C and 55.3 °C at 30% and 25% transmission respectively. The temperature of the graphite of the mode stripper became the limiting factor for the

(a)   (b)
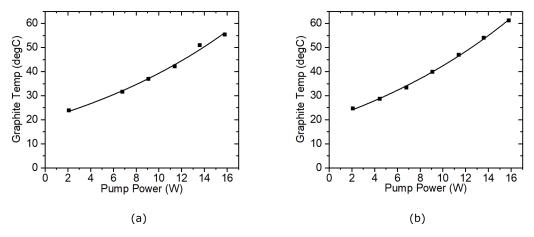
Figure 6.17: Graphs showing the temperature of the graphite coated mode stripper, at the fibre tip, against input pump power. (a) and (b) show operation at 30% and 25% output coupling respectively. The red line shows an exponential fit to the data.

pumping, due to concerns over melting of the fibre jacket, which we believed may happen at approximately 90-100 °C.

6.5.6   HG mode results

The VOC was also operated with only angular misalignment, θ, to generate a HG_{10} mode output. The VOC was operated with a transmission of 31% and at 15.8 W of pump power the cavity had an output power of 5.28 W. The output power against pump power is shown

in fig. 6.18. The transverse spatial intensity profile of the HG_{10} output mode is shown in fig.
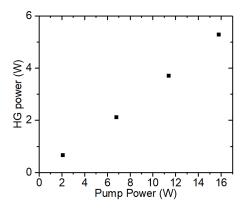
Figure 6.18: Graph showing output power in the HG_{10} mode against pump power.

6.19(a). The mode had an excellent $M^2_{X/Y} = 3.07/1.09$, which is very close to the theoretical value of $M^2_{X/Y} = 3.0/1.0$. The π phase jump from one half to the other half of the beam is demonstrated by the interference pattern shown in fig. 6.19(b).

(a)   (b)
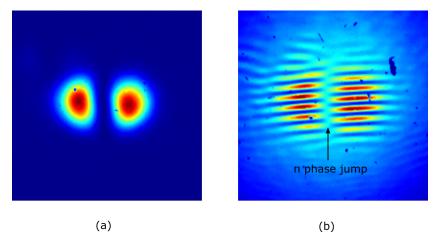
Figure 6.19: (a) Snapshot of the spatial intensity profile of the HG_{10} output mode. (b) Snapshot of the interference pattern between the HG_{10} and a plane wave.

6.5.7   Higher order vortex results

For some vortex applications, such as communication, higher order vortex modes are desired. However, in the configuration demonstrated in this chapter the VOC is only able to generate first order LG and HG modes. Subsequent VOCs could be cascaded to access higher order modes and superpositions thereof, but the limited conversion efficiency of the VOC outside of the laser cavity would come to bear. The high purity first order vortex could however be used in conjunction with a spiral phase plate (SPP), to access higher order LG modes.

As seen in chapter 2, the SPP is a essentially a $exp(i\phi)$ phase mask etched into fused silica. One of the issues going from a fundamental Gaussian to the $LG_{0\pm1}$ modes, using this method, is the spatial profile mismatch between the two modes. However, going from an LG_{01} to LG_{02+}, the spatial profiles are a better match. By using the SPP to convert the output of the vortex laser, with the VOC, high efficiency, high quality and high power higher order LG modes could be accessed.

For these results, two SPPs were used: one with OAM = 1 and the other with OAM = 2. When the SPPs are oriented so that the phase ramp circles in the same direction as the helical phase of the incident beam, there is an addition of OAM, whereas if the SPP is oriented such that the phase ramp spirals in the opposite there is a subtraction of OAM.

A vortex generated by the fibre system in the previous section was used as the incident beam for these results. Fig. 6.20 shows the results of adding the two SPPs into the path of the beam. Fig. 6.20(a) shows the OAM = 1 SPP aligned in a complimentary fashion, resulting in a LG_{02} mode. The central null is slightly larger than with the LG_{01} and two forks can be seen in the interference pattern. Fig. 6.20(b) shows the OAM = 2 SPP aligned in a complimentary fashion, resulting in a LG_{03} mode. The central null is even larger still and this time three forks can be seen in the interference patterns. The final result, from aligning the OAM = 1 SPP opposite to the incident beam, is shown fig. 6.20(c). The transverse spatial intensity profile is not quite Gaussian and seems to have a pedestal, however the interference pattern shows that the OAM has been completely removed from the beam.

6.6   Chapter summary

In this chapter an overview of vortex conversion techniques in fibre systems was given and it was demonstrated that the VOC could successfully be integrated with a fibre laser cavity. This was approached systematically, to ensure the the viability of the integration.

In the first system, light was coupled out of a passive single-mode fibre and successfully converted into a vortex using the Sagnac interferometer. Importantly, the reflected light was also successfully coupled back into the single-mode fibre, which is a key step to demonstrating its viability as a VOC in a fibre cavity.

OAM +1   OAM +2   OAM -1

(a)   (b)   (c)
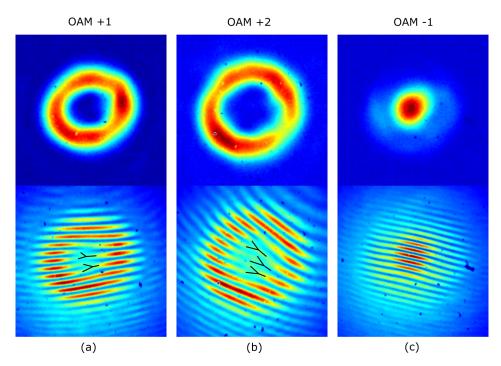
Figure 6.20: Tranverse spatial intensity profiles and interference patterns of the incident LG$_{01}$ after passing through the two SPPs in various configurations. (a) and (b) show the mode after passing through the OAM = 1 and OAM = 2 SPPs, respectively, when aligned so that the phase ramp has the same handed as the incident beams helical phase. (c) shows the beam after passing through the OAM = 1 SPP when aligned with opposite handedness. Black lines drawn on to help reader identify the forks in the interference patterns.

In the next system, a low power fibre gain cavity was set up. The VOC was successfully integrating and lasing was observed. A vortex output was achieved with M$^2_{X/Y}$ = 2.11/2.24. The beamsplitter in the VOC was chosen to be polarisation independent, which was successfully experimentally verified.

In the final system, the VOC was successfully output over 5 W of power in a vortex mode, with a mode purity starting at 97.8%. It was observed that the mode purity reduced as the power was increased and the spatial intensity profile became assymetric, however, it was concluded that this was due he presence of a thermal lens in the collimating lens, which moved the beam waist away from mirror M2 in the VOC. It was shown that this could be compensated for by adjusted the distance between the fibre tip and the collimating lens, thereby correcting the required re-imaging criteria. The system was also investigated and it was found that there was a lot of heating around the fibre tip where the light was being recoupled, which became the limiting factor on the power scaling in this work. Over 5 W of output power was also achieved in the HG$_{01}$ mode. Using a vortex output from the system, a series of spiral phase plates were

successfully used to convert the vortex output of the laser into higher and lower order modes.

Chapter 7

Thesis summary and discussion

This thesis presented work on using a Sagnac interferometer as a vortex generating output coupler. The Sagnac interferometer was presented and the use of this device for vortex generation experimentally tested. The experimental conditions for correct Sagnac interferometer alignment were presented and verified, and the conversion of a fundamental Gaussian mode into an $LG_{0\pm1}$ was successfully demonstrated. These results can be used to diagnose causes of imperfect conversion using the Sagnac interferometer. The Sagnac interferometer was also shown to transform an LG_{01} mode into either a vortex pair superposition or into an LG_{10} mode, depending on the handedness of the misalignements, which contributed to a published work [35].

The Sagnac interferometer was then successfully integrated into a laser cavity, as a vortex output coupler (VOC), achieving over $3\,W$ of vortex output power. This represented the first time ever, to the best of our knowledge, that a Sagnac interferometer had been used as the output coupler of a laser cavity to convert the internal cavity mode into a vortex output. These results were published in a peer reviewed journal [37].

The performance of the VOC in a laser cavity was compared with a plane mirror output coupler in a similar cavity, and was shown to only have a few percent impact on laser performance, which may be due to the extra optics and the AR face of the beamsplitter, in the VOC. The VOC was also shown to work in a q-switched cavity, creating a pulsed vortex source, with no detrimental effects to laser efficiency or vortex quality. When comparing the intracavity modes of the laser cavities with and without the VOC, it was noticed that the VOC cavity

maintained a near diffraction limited mode even when the cavity geometry was purposefully altered to encourage higher order modes to propagate. This was investigated and VOC was experimentally shown to create greater losses for higher order modes in the cavity, effectively suppressing them. These results were published in a peer reviewed journal [40].

To better power scale the cavity, a new crystal was used, which helped to negate some of the thermal lensing in the gain medium. Using this crystal, over 30 W of vortex output power was achieved, a record from-the-source generated vortex power at the time of publishing to the best of our knowledge. Stable q-switched vortex pulses, with repetition rates from 100-600 kHz was demonstrated, with a maximum pulse energy of 303 µJ and a peak power of 15 kW. The generation of high power HG_{10} and HG_{01}, using the same cavity with simple changes to the misalignments in the VOC, was also demonstrated. These results were published in a peer reviewed journal [75].

The VOC can replace the output coupler of any fundamental Gaussian mode cavity, and we have also shown that it effectively operates in high quality mode even in a standard cavity operating in multimode $M^2 = 3.6$. This makes it a highly effective solution for high power, wavelength tunable vortex lasers. Therefore, the VOC could be used to convert any high-power solid-state laser operating in fundamental mode or close to fundamental mode into a vortex laser, for example in thin-disk technologies [73, 74] . Furthermore, as an alternative use, the VOC could be implemented solely for its property of acting as a self-filtering-mode selector in a laser to improve the fundamental Gaussian output.

The high-power Q-switched vortex laser system with high pulse rate offers a promising candidate for high scan speed material processing applications [2]. The output power of the 30 W vortex laser system was only limited by available pump power showing the power scaling potential of the interferometric transformation technique. The technique could be automated for fast, accurate switching between modes, vortex handedness and output coupling transmission. This provides a route to industrial class speeds, for example in material processing, with control of output coupling transmission and spatial mode tunability. This may also open a new avenue into optical trapping and levitation, for example in particle physics applications, where macroscopic targets require a high-power trapping beam [6, 7]. Since the vortex method

uses low-cost, high-power handling components capable of operation across a wide wavelength range its implementation can be envisaged in a wide class of lasers without need for custom-manufactured wavelength specific components. This offers the attractive prospect of robust, turn-key laser solutions for future vortex light applications. Further promise for route to higher order structured light is potentially by using cascaded VOCs [35]. The VOC methodology offers a versatile platform for the generation of structured light and is a unique addition to the structured light toolkit.

The fibre vortex systems shown demonstrated the implementation versatility of the VOC. Over 5 W of vortex power was achieved with excellent mode quality. Importantly, the laser efficiency exceeded the extra-cavity conversion efficiency. This efficiency could be further improved by implementing polarisation independent HR turning mirrors in the VOC. The heating of the mode stripper at the tip of the fibre ended up being the limiting factor on the power scaling of the system. In a future iteration of the system, a cooling system could be employed to better remove the heat, or an aperture could be used to remove any of the reflected power that does not overlap with the incident beam.

7.1 Applications

Due to the unique properties of the Sagnac interferometer, as a vortex output coupler and as a general vortex conversion method, a range of interesting potential applications are available.

Material surface processing

Material surface texturing, using structured light sources, is blossoming as a research field because of the available control on the micro- and nano- scales. The literature shows two main avenues of research in this area: (chiral) nanoneedle formation and surface texturing.

Twisted structures on the nanoscale are of interest for a plethora of reasons and optical vortex modes are at the heart of the research, however there is still some dispute over their exact formation process. Some groups claim that the orbital angular momentum is the active component in shaping the chirality of the nanoneedle [3, 87, 88, 89]. A different group states that the chirality of the nanoneedle is driven by the temperature profile imparted by the pulsed beam [4, 90, 91]. The vortex interferes with its own reflection to impart a spiral heat profile on

the material, which drvies the chiral nanoneedle formation. Whether the OAM of the beam or the intensity profile at the surface is the driving factor, high quality vortex beams are required.

The second avenue of current research is surface texturing, which is interested in regulating the surface properties of materials (eg. optical, mechanical, chemical, biological and wetting). Grooved patterns on the nanoscale, with various structures and orientations, have been experimentally imprinted on material surfaces [92, 93, 94, 95]. The high power potential of the vortex generation method presented in this thesis would allow for increased pulse repetition rates and therefore higher scanning speeds, which would be required to produce textured surfaces on an industrial scale.

Optical trapping, levitation and manipulation

Given the annular intensity profile, the optical vortex has also been researched with regard to the trapping and levitating of particles, as there is less light interaction than with gradient force trapping making it more suitable for sensitive materials [96, 97, 98]. When levitating a particle using a vortex beam, with the beam aligned to propagate in the opposing direction to gravity, optically opaque particles can be trapped with a single beam relying on the balance of radiation pressure and gravity. Using a vortex beam, rather than any other annular beam, also presents the possibility of the transfer of OAM to the trapped particle [99, 100, 101, 102]. Most of the research done is conducted with mW power levels, therefore with the results presented in this thesis potentially far larger particle could be levitated or a single source could be split and used to trap multiple objects.

Ultrashort vortex pulses

Ultrashort vortex pulses for material processing, or other applications, require conversion methods which are independent of wavelength and use optics with high damage thresholds. It has already been demonstrated that the Sagnac interferometer can be used to convert fundamental Gaussian femtosecond pulses into vortex pulses [38], however this was performed external to the cavity. By integrating the Sagnac into the cavity, as demonstrated in this thesis, the conversion effectively becomes lossless and the system becomes more compact and stable.

Soft aperture for fundamental Gaussian generation

A continuous field of interest is pushing the maximum power output of lasers, while maintaining a fundamental Gaussian output mode. The use of hard apertures to increase losses of higher order modes in the cavity can be effective at low powers, however as the system power is scaled apertures would quickly over heat and potentially melt. As demonstrated experimentally in this thesis, the VOC creates higher losses for higher order modes when operated in transmission, effectively filtering them out of the cavity. It could therefore be introduced into the cavity, with low transmission, to act as a soft aperture for the cavity mode. This may be useful in kilo-Watt class lasers, where complex cavity designs are created to keep the cavity mode as close to the diffraction limit as possible [103].

White light/broadband light metrology with helically phased light

In metrology, white light interferometry is used for material surface metrology [104, 105]. By utilising a white light vortex, additional information may be extracted due to the additional helical phase profile. In astronomy, coronagraphs are used to view relatively dim objects next to distant stars. One technique to achieve this is to convert the incoming light into a vortex, where the star is the centre of the light source [106]. The Sagnac interferometer could be used for either application, due to its wavelength independence.

7.2 Potential future project direction

Given the many advantages of the Sagnac interferometer and the VOC for vortex generation, this project has the potential to go in a number of directions.

Tunable vortex laser

The photonics group at Imperial College London has demonstrated multi-Watt, wavelength-tunable fundamental Gaussian operation in an alexandrite laser [107]. By implementing the VOC as an output coupler, this may present a route to a compact, mulit-Watt, wavelength-tunable vortex source in the near infrared spectrum. Apart from sourcing an appropriate beamsplitter and turning mirrors for the tuning range, the challenge would be in the increased cavity losses introduced by the VOC. With the lower gain of Alexandrite, compared with

Neodynium doped Vanadate, the small losses incurred by extra optics and reflections from AR faces may prove significant.

Broadband/super-continuum vortex conversion

To further demonstrate the virtues of the Sagnac interferometer as a vortex conversion method it would be interesting to use it to convert a broadband source. This could then provide a source for white light topology or the basis for a wavelength multiplexing system for communication. Depending on how broadband the source is, the challenge would be to find a suitable beamsplitter to cover the spectrum. The turning mirrors would also need to be HR for the desired spectrum, however some extra losses would not be as detrimental as in the Alexandrite cavity.

"Macro"-particle levitation

Particles on the order of 10s of microns are already being levitated and manipulated optically. However, with the power provided by the system presented in this thesis larger particles (100s of microns) could be levitated. While this is interesting from a Physics point of view, this may also be useful for high energy Physics where they often need to isolate a particle before destroying it to study the effects.

Vortex source

A vortex in a Michelson interferometer can be used to detect changes in the refractive index of transmissive objects [108]. The sample is placed in one arm of the interferometer, changing the optical path length of that arm. When the two arms meet at the beamsplitter again they interfere to produce a petal pattern. The rotation of the petal pattern can be correlated to changes of refractive index in the sample. The extra power provided by the system in this thesis could be used for thicker samples or for detecting changes through a highly scattering medium.

Using the same Michelson interferometer set up the sample could be replaced with a helically wedged pinwheel, which could be rotated to produce a constantly rotating petal pattern. If the pinwheel were manufactured from fused silica, with AR coatings, the set up could be used to produce high power rotating petal beams. While this would be interesting from a Physics

perspective, I can only speculate as to how this may be used practically: Rotating gradient traps, drilling/material surface processing and/or communication.

Finally, the VOC integrated cavity could be further power scaled to create a new, more powerful vortex source. This could be used as it is, or used an a seed to further higher order structured light generation, as briefly demonstrated in this thesis.

Bibliography

[1] L. Allen, M. W. Beijersbergen, R. Spreeuw, and J. Woerdman, "Orbital angular momentum of light and the transformation of laguerre-gaussian laser modes," *Physical Review A*, vol. 45, no. 11, p. 8185, 1992.

[2] T. Omatsu, K. Miyamoto, K. Toyoda, R. Morita, Y. Arita, and K. Dholakia, "A new twist for materials science: the formation of chiral structures using the angular momentum of light," *Advanced Optical Materials*, vol. 7, no. 14, p. 1801672, 2019.

[3] K. Toyoda, K. Miyamoto, N. Aoki, R. Morita, and T. Omatsu, "Using optical vortex to control the chirality of twisted metal nanostructures," *Nano letters*, vol. 12, no. 7, pp. 3645–3649, 2012.

[4] S. Syubaev, A. Zhizhchenko, A. Kuchmizhak, A. Porfirev, E. Pustovalov, O. Vitrik, Y. Kulchin, S. Khonina, and S. Kudryashov, "Direct laser printing of chiral plasmonic nanojets by vortex beams," *Optics express*, vol. 25, no. 9, pp. 10214–10223, 2017.

[5] H. He, M. Friese, N. Heckenberg, and H. Rubinsztein-Dunlop, "Direct observation of transfer of angular momentum to absorptive particles from a laser beam with a phase singularity," *Physical review letters*, vol. 75, no. 5, p. 826, 1995.

[6] C. Price, T. Donnelly, S. Giltrap, N. Stuart, S. Parker, S. Patankar, H. Lowe, D. Drew, E. Gumbrell, and R. Smith, "An in-vacuo optical levitation trap for high-intensity laser interaction experiments with isolated microtargets," *Review of Scientific Instruments*, vol. 86, no. 3, p. 033502, 2015.

[7] W. Zhu, N. Eckerskorn, A. Upadhya, L. Li, A. V. Rode, and W. M. Lee, "Dynamic axial control over optically levitating particles in air with an electrically-tunable variable-focus lens," *Biomedical optics express*, vol. 7, no. 7, pp. 2902–2911, 2016.

[8] J. Wang, J.-Y. Yang, I. M. Fazal, N. Ahmed, Y. Yan, H. Huang, Y. Ren, Y. Yue, S. Dolinar, M. Tur, *et al.*, "Terabit free-space data transmission employing orbital angular momentum multiplexing," *Nature photonics*, vol. 6, no. 7, p. 488, 2012.

[9] A. S. Ostrovsky, C. Rickenstorff-Parrao, and V. Arrizón, "Generation of the "perfect" optical vortex using a liquid-crystal spatial light modulator," *Optics letters*, vol. 38, no. 4, pp. 534–536, 2013.

[10] J. García-García, C. Rickenstorff-Parrao, R. Ramos-García, V. Arrizón, and A. S. Ostrovsky, "Simple technique for generating the perfect optical vortex," *Optics letters*, vol. 39, no. 18, pp. 5305–5308, 2014.

[11] K. Otomo, T. Hibi, Y. Kozawa, and T. Nemoto, "Sted microscopy—super-resolution bio-imaging utilizing a stimulated emission depletion," *Microscopy*, vol. 64, no. 4, pp. 227–236, 2015.

[12] M. Beijersbergen, R. Coerwinkel, M. Kristensen, and J. Woerdman, "Helical-wavefront laser beams produced with a spiral phaseplate," *Optics communications*, vol. 112, no. 5-6, pp. 321–327, 1994.

[13] M. Massari, G. Ruffato, M. Gintoli, F. Ricci, and F. Romanato, "Fabrication and characterization of high-quality spiral phase plates for optical applications," *Applied Optics*, vol. 54, no. 13, pp. 4077–4083, 2015.

[14] V. Y. Bazhenov, M. Vasnetsov, and M. Soskin, "Laser beams with screw dislocations in their wavefronts," *Jetp Lett*, vol. 52, no. 8, pp. 429–431, 1990.

[15] V. Y. Bazhenov, M. Soskin, and M. Vasnetsov, "Screw dislocations in light wavefronts," *Journal of Modern Optics*, vol. 39, no. 5, pp. 985–990, 1992.

[16] N. Heckenberg, R. McDuff, C. Smith, and A. White, "Generation of optical phase singularities by computer-generated holograms," *Optics letters*, vol. 17, no. 3, pp. 221–223, 1992.

[17] C. Rui, Z. Hong, M. Marco, W. Xiaodong, and L. Jiandong, "Orbital angular momentum waves: Generation, detection and emerging applications," *arXiv preprint arXiv:1903.07818*, 2019.

[18] J. Arlt, K. Dholakia, L. Allen, and M. Padgett, "The production of multiringed laguerre–gaussian modes by computer-generated holograms," *Journal of modern optics*, vol. 45, no. 6, pp. 1231–1237, 1998.

[19] Y. Li, J. Kim, and M. J. Escuti, "Orbital angular momentum generation and mode transformation with high efficiency using forked polarization gratings," *Applied optics*, vol. 51, no. 34, pp. 8236–8245, 2012.

[20] N. Radwell, R. Hawley, J. Götte, and S. Franke-Arnold, "Achromatic vector vortex beams from a glass cone," *Nature communications*, vol. 7, no. 1, pp. 1–6, 2016.

[21] E. Abramochkin and V. Volostnikov, "Beam transformations and nontransformed beams," *Optics Communications*, vol. 83, no. 1-2, pp. 123–135, 1991.

[22] C. Tamm and C. Weiss, "Bistability and optical switching of spatial patterns in a laser," *JOSA B*, vol. 7, no. 6, pp. 1034–1038, 1990.

[23] M. W. Beijersbergen, L. Allen, H. Van der Veen, and J. Woerdman, "Astigmatic laser mode converters and transfer of orbital angular momentum," *Optics Communications*, vol. 96, no. 1-3, pp. 123–132, 1993.

[24] R. Uren, S. Beecher, C. R. Smith, and W. A. Clarkson, "Method for generating high purity laguerre–gaussian vortex modes," *IEEE Journal of quantum electronics*, vol. 55, no. 5, pp. 1–9, 2019.

[25] L. Marrucci, C. Manzo, and D. Paparo, "Optical spin-to-orbital angular momentum conversion in inhomogeneous anisotropic media," *Physical review letters*, vol. 96, no. 16, p. 163905, 2006.

[26] Y.-W. Huang, N. A. Rubin, A. Ambrosio, Z. Shi, R. C. Devlin, C.-W. Qiu, and F. Capasso, "Versatile total angular momentum generation using cascaded j-plates," *Optics express*, vol. 27, no. 5, pp. 7469–7484, 2019.

[27] R. Chriki, E. Maguid, C. Tradonsky, V. Kleiner, A. A. Friesem, N. Davidson, and E. Hasman, "Spin-controlled twisted laser beams: intra-cavity multi-tasking geometric phase metasurfaces," *Optics Express*, vol. 26, no. 2, pp. 905–916, 2018.

[28] E. Maguid, I. Yulevich, D. Veksler, V. Kleiner, M. L. Brongersma, and E. Hasman, "Photonic spin-controlled multifunctional shared-aperture antenna array," *Science*, vol. 352, no. 6290, pp. 1202–1206, 2016.

[29] W. Shao, S. Huang, M. Chen, X. Liu, and W. Xie, "Research of optical vortex's energy efficiency and diffraction angle based on spatial light modulator," *Optical Engineering*, vol. 56, no. 8, p. 086113, 2017.

[30] D. Lin, J. Daniel, and W. Clarkson, "Controlling the handedness of directly excited laguerre–gaussian modes in a solid-state laser," *Optics letters*, vol. 39, no. 13, pp. 3903–3906, 2014.

[31] S. Lohani, E. M. Knutson, M. O'Donnell, S. D. Huver, and R. T. Glasser, "On the use of deep neural networks in optical communications," *Applied optics*, vol. 57, no. 15, pp. 4180–4190, 2018.

[32] Y. He, J. Liu, P. Wang, W. Xiong, Y. Wu, X. Zhou, Y. Cheng, Y. Gao, Y. Li, S. Chen, *et al.*, "Detecting orbital angular momentum modes of vortex beams using feed-forward neural network," *Journal of Lightwave Technology*, vol. 37, no. 23, pp. 5848–5855, 2019.

[33] J. Pinnell, V. Rodríguez-Fajardo, and A. Forbes, "Probing the limits of orbital angular momentum generation and detection with spatial light modulators," *Journal of Optics*, vol. 23, no. 1, p. 015602, 2020.

[34] M. Takeda, H. Ina, and S. Kobayashi, "Fourier-transform method of fringe-pattern analysis for computer-based topography and interferometry," *JosA*, vol. 72, no. 1, pp. 156–160, 1982.

[35] M. J. Damzen, W. R. Kerridge-Johns, and J. Geberbauer, "Vortex mode transformation interferometry," *Journal of Optics*, vol. 22, no. 1, p. 015604, 2019.

[36] P. Vaity, A. Aadhi, and R. Singh, "Formation of optical vortices through superposition of two gaussian beams," *Applied optics*, vol. 52, no. 27, pp. 6652–6656, 2013.

[37] W. Kerridge-Johns, J. Geberbauer, and M. Damzen, "Vortex laser by transforming gaussian mode with an interferometric output coupler," *Optics express*, vol. 27, no. 8, pp. 11642–11650, 2019.

[38] D. N. Naik, N. A. Saad, D. N. Rao, and N. K. Viswanathan, "Ultrashort vortex from a gaussian pulse–an achromatic-interferometric approach," *Scientific reports*, vol. 7, no. 1, p. 2395, 2017.

[39] W. R. Kerridge-Johns, J.-B. Jaillot, and M. J. Damzen, "Sampling a vortex from a gaussian beam using a wedge-plate shearing interferometer," *Applied Optics*, vol. 60, no. 12, pp. 3510–3516, 2021.

[40] J. Geberbauer, W. Kerridge-Johns, and M. Damzen, "Q-switched laser with self-mode-filtering interferometric vortex output coupler," *OSA Continuum*, vol. 3, no. 2, pp. 204–213, 2020.

[41] H. Rubinsztein-Dunlop, A. Forbes, M. V. Berry, M. R. Dennis, D. L. Andrews, M. Mansuripur, C. Denz, C. Alpmann, P. Banzer, T. Bauer, *et al.*, "Roadmap on structured light," *Journal of Optics*, vol. 19, no. 1, p. 013001, 2016.

[42] S. C. Kumar, A. Esteban-Martin, and M. Ebrahim-Zadeh, "Interferometric output coupling of ring optical oscillators," *Optics letters*, vol. 36, no. 7, pp. 1068–1070, 2011.

[43] K. Kano, Y. Kozawa, and S. Sato, "Generation of a purely single transverse mode vortex beam from a he-ne laser cavity with a spot-defect mirror," *International Journal of Optics*, vol. 2012, 2012.

[44] S. Wang, Z. Zhao, I. Ito, and Y. Kobayashi, "Direct generation of femtosecond vortex beam from a yb: Kyw oscillator featuring a defect-spot mirror," *OSA Continuum*, vol. 2, no. 3, pp. 523–530, 2019.

[45] F. Tang, B. Shi, Q. Zhang, C. Zhou, Y. Bu, and J. Li, "Sesam-based mode-locked vortex ti: sapphire laser using spot-defect spatial filter for intra-cavity mode selection," *Laser Physics*, vol. 30, no. 12, p. 125802, 2020.

[46] S. Tan, C. Zhou, A. Shirakakwa, K.-i. Ueda, and J. Li, "Vortex ti: Sapphire laser by using an intracavity spot-defect spatial filter," *Optics & Laser Technology*, vol. 96, pp. 76–80, 2017.

[47] A. J. Lee, T. Omatsu, and H. M. Pask, "Direct generation of a first-stokes vortex laser beam from a self-raman laser," *Optics Express*, vol. 21, no. 10, pp. 12401–12409, 2013.

[48] Y. Uesugi, Y. Kozawa, and S. Sato, "Direct generation of the lowest-order vortex beam using a spot defect mirror in the ultraviolet region," *Optics Letters*, vol. 45, no. 7, pp. 2115–2118, 2020.

[49] S. Ngcobo, I. Litvin, L. Burger, and A. Forbes, "A digital laser for on-demand laser modes," *Nature communications*, vol. 4, no. 1, pp. 1–6, 2013.

[50] D. Kim, J. Kim, and W. Clarkson, "Q-switched nd: Yag optical vortex lasers," *Optics Express*, vol. 21, no. 24, pp. 29449–29454, 2013.

[51] J. Li, Y. Yao, J. Yu, K. Xia, and C. Zhou, "Efficient vortex laser with annular pumping formed by circle dammann grating," *Ieee Photonics Technology Letters*, vol. 28, no. 4, pp. 473–476, 2015.

[52] Q. Zhang, J. Yu, B. Shi, F. Tang, and J. Li, "Lg 11-mode vortex nd: Yag laser by applying second-order circular dammann grating for annular pumping," *Chinese Optics Letters*, vol. 17, no. 5, p. 051402, 2019.

[53] Z. Fang, Y. Yao, K. Xia, and J. Li, "Actively q-switched and vortex nd: Yag laser," *Optics Communications*, vol. 347, pp. 59–63, 2015.

[54] X. Huang, B. Xu, S. Cui, H. Xu, Z. Cai, and L. Chen, "Direct generation of vortex laser by rotating induced off-axis pumping," *IEEE Journal of Selected Topics in Quantum Electronics*, vol. 24, no. 5, pp. 1–6, 2018.

[55] Y. Ma, A. Vallés, J.-C. Tung, Y.-F. Chen, K. Miyamoto, and T. Omatsu, "Direct generation of red and orange optical vortex beams from an off-axis diode-pumped pr 3+: Ylf laser," *Optics Express*, vol. 27, no. 13, pp. 18190–18200, 2019.

[56] Y. Shen, Y. Meng, X. Fu, and M. Gong, "Wavelength-tunable hermite–gaussian modes and an orbital-angular-momentum-tunable vortex beam in a dual-off-axis pumped yb: Calgo laser," *Optics Letters*, vol. 43, no. 2, pp. 291–294, 2018.

[57] P. Tuan, Y. Hsieh, Y. Lai, K.-F. Huang, and Y.-F. Chen, "Characterization and generation of high-power multi-axis vortex beams by using off-axis pumped degenerate cavities with external astigmatic mode converter," *Optics Express*, vol. 26, no. 16, pp. 20481–20491, 2018.

[58] C.-Y. Lee, C.-C. Chang, C.-Y. Cho, P.-H. Tuan, and Y.-F. Chen, "Generation of higher order vortex beams from a yvo 4/nd: Yvo 4 self-raman laser via off-axis pumping with mode converter," *IEEE Journal of Selected Topics in Quantum Electronics*, vol. 21, no. 1, pp. 318–322, 2014.

[59] P. Tuan, K. Cheng, and Y. Cheng, "Generating high-power lissajous structured modes and trochoidal vortex beams by an off-axis end-pumped nd: Yvo 4 laser with astigmatic transformation," *Optics Express*, vol. 29, no. 15, pp. 22957–22965, 2021.

[60] Z. Xinmiao, L. Jingliang, L. Mingming, L. Ruobing, Z. Luan, J. Guangyong, and C. Xinyu, "Off-axis pumped tm: Ylf vortex laser with continuously tunable wavelength," *Infrared Physics & Technology*, p. 104064, 2022.

[61] W. R. Kerridge-Johns and M. J. Damzen, "Vortex laser from anti-resonant ring coupled cavities," *Optics express*, vol. 26, no. 25, pp. 32839–32846, 2018.

[62] S. Chard, P. Shardlow, and M. Damzen, "High-power non-astigmatic tem 00 and vortex mode generation in a compact bounce laser design," *Applied Physics B*, vol. 97, no. 2, p. 275, 2009.

[63] M. Okida, Y. Hayashi, T. Omatsu, J. Hamazaki, and R. Morita, "Characterization of 1.06 μm optical vortex laser based on a side-pumped nd: Gdvo 4 bounce oscillator," *Applied Physics B*, vol. 95, no. 1, pp. 69–73, 2009.

[64] G. Thomas, A. Minassian, and M. Damzen, "Optical vortex generation from a diode-pumped alexandrite laser," *Laser Physics Letters*, vol. 15, no. 4, p. 045804, 2018.

[65] D. Naidoo, F. S. Roux, A. Dudley, I. Litvin, B. Piccirillo, L. Marrucci, and A. Forbes, "Controlled generation of higher-order poincaré sphere beams from a laser," *Nature Photonics*, vol. 10, no. 5, p. 327, 2016.

[66] D. Wei, Y. Cheng, R. Ni, Y. Zhang, X. Hu, S. Zhu, and M. Xiao, "Generating controllable laguerre-gaussian laser modes through intracavity spin-orbital angular momentum conversion of light," *Physical Review Applied*, vol. 11, no. 1, p. 014038, 2019.

[67] E. Maguid, R. Chriki, M. Yannai, V. Kleiner, E. Hasman, A. A. Friesem, and N. Davidson, "Topologically controlled intracavity laser modes based on pancharatnam-berry phase," *ACS Photonics*, vol. 5, no. 5, pp. 1817–1821, 2018.

[68] H. Sroor, Y.-W. Huang, B. Sephton, D. Naidoo, A. Valles, V. Ginis, C.-W. Qiu, A. Ambrosio, F. Capasso, and A. Forbes, "High-purity orbital angular momentum states from a visible metasurface laser," *Nature Photonics*, vol. 14, no. 8, pp. 498–503, 2020.

[69] L. Burger, I. Litvin, S. Ngcobo, and A. Forbes, "Implementation of a spatial light modulator for intracavity beam shaping," *Journal of Optics*, vol. 17, no. 1, p. 015604, 2014.

[70] M. Born and E. Wolf, *Principles of optics: electromagnetic theory of propagation, interference and diffraction of light.* Elsevier, 2013.

[71] V. Magni, "Resonators for solid-state lasers with large-volume fundamental mode and high alignment stability," *Applied optics*, vol. 25, no. 1, pp. 107–117, 1986.

[72] S.-C. Sheng and A. Siegman, "Perturbed gaussian modes of an unbalanced antiresonant-ring laser cavity," *JOSA*, vol. 66, no. 10, pp. 1032–1036, 1976.

[73] F. Saltarelli, I. J. Graumann, L. Lang, D. Bauer, C. R. Phillips, and U. Keller, "350-w average-power sesam-modelocked ultrafast thin-disk laser," in *The European Conference on Lasers and Electro-Optics*, p. cf_1_1, Optical Society of America, 2019.

[74] S.-S. Schad, C. Stolzenburg, K. Michel, and D. Sutter, "Latest advances in high brightness disk lasers: high power performance from cw to short and ultra short pulses," *Laser Technik Journal*, vol. 11, no. 2, pp. 49–53, 2014.

[75] J. Geberbauer, W. Kerridge-Johns, and M. Damzen, "¿ 30 w vortex lg 01 or hg 10 laser using a mode transforming output coupler," *Optics Express*, vol. 29, no. 18, pp. 29082–29094, 2021.

[76] A. Sugiyama and Y. Nara, "Improved direct bonding method of nd: Yvo4 and yvo4 laser crystals," *Ceramics international*, vol. 31, no. 8, pp. 1085–1090, 2005.

[77] Z. Zhuo, T. Li, X. Li, and H. Yang, "Investigation of nd: Yvo4/yvo4 composite crystal and its laser performance pumped by a fiber coupled diode laser," *Optics communications*, vol. 274, no. 1, pp. 176–181, 2007.

[78] Y. Sato, T. Taira, N. Pavel, and V. Lupei, "Laser operation with near quantum-defect slope efficiency in nd: Yvo 4 under direct pumping into the emitting level," *Applied physics letters*, vol. 82, no. 6, pp. 844–846, 2003.

[79] E. Snitzer, "Optical maser action of nd+ 3 in a barium crown glass," *Physical Review Letters*, vol. 7, no. 12, p. 444, 1961.

[80] E. Snitzer, "Proposed fiber cavities for optical masers," *Journal of Applied Physics*, vol. 32, no. 1, pp. 36–39, 1961.

[81] T. Maiman, "Stimulated optical radiation in ruby," *Nature*, vol. 187, no. 4736, pp. 493–494, 1960.

[82] Y. Tanaka, M. Okida, K. Miyamoto, and T. Omatsu, "High power picosecond vortex laser based on a large-mode-area fiber amplifier," *Optics express*, vol. 17, no. 16, pp. 14362–14366, 2009.

[83] J. Zou, H. Wang, W. Li, T. Du, B. Xu, N. Chen, Z. Cai, and Z. Luo, "Visible-wavelength all-fiber vortex laser," *IEEE Photonics Technology Letters*, vol. 31, no. 18, pp. 1487–1490, 2019.

[84] Z. Zhang, Y. Cai, J. Wang, H. Wan, and L. Zhang, "Switchable dual-wavelength cylindrical vector beam generation from a passively mode-locked fiber laser based on carbon nanotubes," *IEEE Journal of Selected Topics in Quantum Electronics*, vol. 24, no. 3, pp. 1–6, 2017.

[85] H. Po, E. Snitzer, R. Tumminelli, L. Zenteno, F. Hakimi, N. Cho, and T. Haw, "Double clad high brightness nd fiber laser pumped by gaalas phased array," in *Optical Fiber Communication Conference*, vol. 5, pp. 220–223, Optical Society of America, 1989.

[86] Y. e. Jeong, J. Sahu, D. Payne, , and J. Nilsson, "Ytterbium-doped large-core fiber laser with 1.36 kw continuous-wave output power," *Optics express*, vol. 12, no. 25, pp. 6088–6092, 2004.

[87] K. Toyoda, F. Takahashi, S. Takizawa, Y. Tokizane, K. Miyamoto, R. Morita, and T. Omatsu, "Transfer of light helicity to nanostructures," *Physical review letters*, vol. 110, no. 14, p. 143603, 2013.

[88] F. Takahashi, K. Toyoda, S. Takizawa, K. Miyamoto, R. Morita, and T. Omatsu, "Chiral structure control of metal nano-needles fabrictaed by optical vortex laser ablation," in *CLEO: Science and Innovations*, pp. CM3H–6, Optical Society of America, 2013.

[89] Y. Nakamura, T. Sugimoto, K. Izumisawa, K. Miyamoto, T. Torimoto, R. Morita, K. Yamane, and T. Omatsu, "Twisted au nanoneedle fabricated by optical vortex illumination," in *Optics and Photonics Japan*, p. 30pON4, Optical Society of America, 2017.

[90] S. Syubaev, A. Zhizhchenko, O. Vitrik, A. Porfirev, S. Fomchenkov, S. Khonina, S. Kudryashov, and A. Kuchmizhak, "Chirality of laser-printed plasmonic nanoneedles tunable by tailoring spiral-shape pulses," *Applied Surface Science*, vol. 470, pp. 526–534, 2019.

[91] S. Syubaev, A. Porfirev, A. Zhizhchenko, O. Vitrik, S. Kudryashov, S. Fomchenkov, S. Khonina, and A. Kuchmizhak, "Zero-orbital-angular-momentum laser printing of chiral nanoneedles," *Optics Letters*, vol. 42, no. 23, pp. 5022–5025, 2017.

[92] J. Jj Nivas, S. He, A. Rubano, A. Vecchione, D. Paparo, L. Marrucci, R. Bruzzese, and S. Amoruso, "Direct femtosecond laser surface structuring with optical vortex beams generated by a q-plate," *Scientific reports*, vol. 5, no. 1, pp. 1–12, 2015.

[93] J. J. Nivas, S. He, Z. Song, A. Rubano, A. Vecchione, D. Paparo, L. Marrucci, R. Bruzzese, and S. Amoruso, "Femtosecond laser surface structuring of silicon with gaussian and optical vortex beams," *Applied Surface Science*, vol. 418, pp. 565–571, 2017.

[94] K. Anoop, R. Fittipaldi, A. Rubano, X. Wang, D. Paparo, A. Vecchione, L. Marrucci, R. Bruzzese, and S. Amoruso, "Direct femtosecond laser ablation of copper with an optical vortex beam," *Journal of Applied Physics*, vol. 116, no. 11, p. 113102, 2014.

[95] J. J. Nivas, H. Shutong, K. Anoop, A. Rubano, R. Fittipaldi, A. Vecchione, D. Paparo, L. Marrucci, R. Bruzzese, and S. Amoruso, "Laser ablation of silicon induced by a femtosecond optical vortex beam," *Optics letters*, vol. 40, no. 20, pp. 4611–4614, 2015.

[96] G. D. Jeffries, J. S. Edgar, Y. Zhao, J. P. Shelby, C. Fong, and D. T. Chiu, "Using polarization-shaped optical vortex traps for single-cell nanosurgery," *Nano letters*, vol. 7, no. 2, pp. 415–420, 2007.

[97] V. Shvedov, A. S. Desyatnikov, A. V. Rode, Y. Izdebskaya, W. Krolikowski, and Y. S. Kivshar, "Optical vortex beams for trapping and transport of particles in air," *Applied Physics A*, vol. 100, no. 2, pp. 327–331, 2010.

[98] L.-M. Zhou, K.-W. Xiao, J. Chen, and N. Zhao, "Optical levitation of nanodiamonds by doughnut beams in vacuum," *Laser & Photonics Reviews*, vol. 11, no. 2, p. 1600284, 2017.

[99] V. Garcés-Chávez, D. McGloin, M. Padgett, W. Dultz, H. Schmitzer, and K. Dholakia, "Observation of the transfer of the local angular momentum density of a multiringed light beam to an optically trapped particle," *Physical review letters*, vol. 91, no. 9, p. 093602, 2003.

[100] D. Cojoc, V. Garbin, E. Ferrari, L. Businaro, F. Romanato, and E. Di Fabrizio, "Laser trapping and micro-manipulation using optical vortices," *Microelectronic Engineering*, vol. 78, pp. 125–131, 2005.

[101] M. Mazilu, Y. Arita, T. Vettenburg, J. M. Auñón, E. M. Wright, and K. Dholakia, "Orbital-angular-momentum transfer to optically levitated microparticles in vacuum," *Physical Review A*, vol. 94, no. 5, p. 053821, 2016.

[102] V. Bobkova, J. Stegemann, R. Droop, E. Otte, and C. Denz, "Optical grinder: sorting of trapped particles by orbital angular momentum," *Optics Express*, vol. 29, no. 9, pp. 12967–12975, 2021.

[103] T. Gottwald, V. Kuhn, S.-S. Schad, C. Stolzenburg, and A. Killi, "Recent developments in high power thin disk lasers at trumpf laser," in *Technologies for Optical Countermeasures X; and High-Power Lasers 2013: Technology and Systems*, vol. 8898, p. 88980P, International Society for Optics and Photonics, 2013.

[104] L. Deck and P. De Groot, "High-speed noncontact profiler based on scanning white-light interferometry," *Applied optics*, vol. 33, no. 31, pp. 7334–7338, 1994.

[105] J. C. Wyant, "White light interferometry," in *Holography: a tribute to yuri denisyuk and emmett leith*, vol. 4737, pp. 98–107, International Society for Optics and Photonics, 2002.

[106] P. Kanburapa and G. A. Swartzlander, "White-light optical vortex coronagraph," in *Frontiers in Optics*, pp. FTh4E–2, Optical Society of America, 2012.

[107] G. Tawy, A. Minassian, and M. J. Damzen, "High-power 7.4 w tem 00 and wavelength-tunable alexandrite laser with a novel cavity design and efficient fibre-coupled diode-pumping," *OSA Continuum*, vol. 3, no. 6, pp. 1638–1649, 2020.

[108] N. M. Kerschbaumer, L. I. Fochler, M. Reichenspurner, T. Lohmueller, M. Fedoruk, and J. Feldmann, "High-precision interferometry with helical light beams," in *Optical and Quantum Sensing and Precision Metrology II*, p. PC1201630, SPIE, 2022.